

ELASTO-INERTIAL MIGRATION OF PARTICLES AND CAPSULES IN
VISCOELASTIC MICROCHANNELS

A Dissertation

Submitted to the Faculty

of

Purdue University

by

Amir Hossein Raffiee

In Partial Fulfillment of the

Requirements for the Degree

of

Doctor of Philosophy

December 2019

Purdue University

West Lafayette, Indiana

THE PURDUE UNIVERSITY GRADUATE SCHOOL
STATEMENT OF DISSERTATION APPROVAL

Dr. Arezoo M. Ardekani, Co-Chair

School of Mechanical Engineering

Dr. Sadegh Dabiri, Co-chair

Department of Agricultural and Biological Engineering and School of
Mechanical Engineering

Dr. Pavlos Vlachos

School of Mechanical Engineering

Dr. Steve Wereley

School of Mechanical Engineering

Approved by:

Dr. Nicole Key

Associate Head for Graduate Studies

ACKNOWLEDGMENTS

I would like to express my sincere gratitude to my Ph.D. advisors Dr. Arezoo M. Ardekani and Dr. Sadegh Dabiri, for providing me with the chance to conduct my research and study at Purdue University. Their knowledge, expertise, and leadership made it possible to overcome the challenges and complete the dissertation.

Furthermore, I would appreciate my committee members Dr. Pavlov Vlachos and Dr. Steve Wereley, for their insightful comments and encouragement.

Lastly, I would like to thank my lovely family: my parents Zahra and Hossein and my sister Shabnam without whom I would have never had this achievement and my friends who supported me during my Ph.D.

TABLE OF CONTENTS

	Page
LIST OF FIGURES	vii
ABSTRACT	xi
1 INTRODUCTION	1
1.1 Motion of cells in a microchannel	2
2 DEFORMATION AND BUCKLING OF MICROCAPSULES IN VISCOELASTIC MATRIX	7
2.1 Summary	7
2.2 Governing equations and Numerical methods	7
2.2.1 Newtonian fluid	7
2.2.2 Non-Newtonian fluid	10
2.3 Problem setup	11
2.4 Numerical verification	13
2.5 Transient dynamics of a viscoelastic capsule in a Newtonian fluid	14
2.5.1 Capsule deformation in a low capillary number regime	16
2.5.2 Capsule deformation in a moderate capillary number regime . . .	19
2.6 Viscoelastic capsule in a Newtonian matrix	23
2.7 Conclusion	25
3 ELASTO-INERTIAL MIGRATION OF DEFORMABLE CAPSULES IN A MICROCHANNEL	27
3.1 Summary	27
3.2 Methodology	28
3.2.1 Governing equations	28
3.2.2 Problem setup	30
3.3 Results and discussion	31

	Page
3.3.1 Cell focusing in a Newtonian fluid	31
3.3.2 Cell focusing in an Oldroyd-B fluid	37
3.3.3 Cell focusing in a Giesekus fluid	42
3.4 Conclusions	47
3.5 Appendix	48
3.5.1 Mesh independency	48
3.5.2 Domain independency	49
3.5.3 Validation of viscoelastic model	49
3.5.4 Validation of numerical method	50
4 SUSPENSION OF DEFORMABLE PARTICLES IN NEWTONIAN AND VISCOELASTIC FLUIDS IN A MICROCHANNEL	53
4.1 Summary	53
4.2 Introduction	53
4.3 Methodology	56
4.3.1 Problem setup	56
4.4 Result and discussion	57
4.4.1 Newtonian fluid	57
4.4.2 Viscoelastic fluid	65
4.5 Conclusions	71
4.6 Appendix	72
5 NUMERICAL INVESTIGATION OF ELASTO-INERTIAL PARTICLE FO- CUSING PATTERNS IN VISCOELASTIC MICROFLUIDIC DEVICES	73
5.1 Summary	73
5.2 Introduction	73
5.3 Mathematical modeling	76
5.4 Result and discussion	80
5.4.1 Migration in a low inertial regime	81
5.4.2 Migration in an intermediate inertial regime	87
5.4.3 Migration in a high inertial regime	90

	Page
5.5 Summary	95
6 Conclusion	97
REFERENCES	99
VITA	110

LIST OF FIGURES

Figure	Page
2.1 Schematic of the problem and coordinate system	13
2.2 A comparison of (a) the capsule deformation parameter and (b) orientation angle with the results of Doddi et al. [69] and Lac et al. [68].	14
2.3 Temporal evolution of (a) the capsule deformation and (b) transient orientation angle at $Ca = 0.2$ and $Wi = 2$	14
2.4 Temporal evolution of (a) the capsule deformation, (b) orientation angle and (c) length of main axes at $Ca = 0.1$	15
2.5 The temporal evolution of (a) the capsule deformation, (b) orientation angle and (c) axes length for $Ca = 0.025$	17
2.6 The deformation of capsule membrane at $Ca = 0.025$ and (a) $Wi = 0$ (b) $Wi = 5$ (c) $Wi = 10$ and (d) The cross section of the capsule membrane for different Weissenberg numbers	18
2.7 The temporal evolution of maximum and minimum principal tensions at $Ca = 0.025$	20
2.8 The temporal evolution of the (a) capsule deformation, (b) orientation angle, and (c) axes length for $Ca = 0.2$	21
2.9 Deformed capsule at $Ca = 0.2$ and (a) $Wi = 0$ (b) $Wi = 5$	22
2.10 (a) The capsule deformation and (b) inclination angle versus capillary number	22
2.11 The normalized value of the tank treading period versus Wi	23
2.12 Temporal evolution of (a) deformation for $Ca = 0.2$ and (b) normalized deformation as a function of Wi	24
2.13 Temporal evolution of (a) orientation angle for $Ca = 0.2$ and (b) normalized orientation angle as a function of Wi	25
2.14 The normalized value of tank treading period versus Wi	26
3.1 Schematic of the microchannel.	32
3.2 (a) The distance of cells from the channel centerline and (b) the trajectories of cells. The blockage ratio is $\frac{a}{W} = 0.3$ and $Re = 37.8$	33

Figure	Page
3.3 (a) The distance of cells from the channel centerline for various Re and La . (b) Cell deformation for various Re and La . The blockage ratio is $\frac{a}{W}=0.3$	34
3.4 Deformed shape of capsules with $\frac{a}{W} = 0.3$ and $Re = 60$ and (a) $La = 1$ (b) $La = 50$ (c) $La = 500$	34
3.5 (a) Equilibrium position of cells for various deformability and size at $Re = 37.8$. (b) Temporal evolution of cross-streamline velocity of cells with $\frac{a}{W}=0.3$ and $Re = 60$	36
3.6 (a) Focal position and (b) trajectories of cells with $\frac{a}{W}=0.3$ and $Re = 37.8$ in an Oldroyd-B fluid.	38
3.7 The flow field around the cell in (a) an Oldroyd-B fluid ($Wi = 2$) and (b) a Giesekus fluid ($Wi = 2$ and $\alpha = 0.1$). The blockage ratio is $\frac{a}{W}=0.2$ and $Re = 37.8$	39
3.8 Focal position of the cells in an Oldroyd-B fluid. Here, $\frac{a}{W}=0.3$ and $La=50$	41
3.9 (a) Final equilibrium location of cells and (b) their corresponding trajectories in a Giesekus fluid. The blockage ratio is $\frac{a}{W}=0.3$ and $Re = 37.8$	43
3.10 Deformed shape of capsules with $\frac{a}{W} = 0.3$, $La = 50$, $Re = 60$ and (a) $Wi = 0$ (b) $Wi = 0.9$ and $\alpha = 0$ (c) $Wi = 2$ and $\alpha = 0$ (d) $Wi = 1$ and $\alpha = 0.2$	45
3.11 (a) Deformation parameter of capsules at $Re = 60$ and (b) the velocity profile at $Z^* = 1$ and $X^* = x_{center}^*$ with $Re = 60$ and $La = 1$	46
3.12 Distance of the capsule from the channel centerline for $La = 500$ and $Re = 37.8$ with $128 \times 76 \times 76$ and $200 \times 128 \times 128$ Eulerian grid points.	49
3.13 Distance of the capsule from the channel centerline at $Re = 200$ and $La = 50$ for a) $Wi = 0$ and b) $Wi = 2$ with $200 \times 128 \times 128$ and $256 \times 152 \times 152$ Eulerian grid points.	50
3.14 Distance of the capsule from the channel centerline at $Re = 100$ and $La = 500$ for different domain lengths $L = 4W$ and $L = 8W$	51
3.15 Deformation of polymeric droplet at $Ca = 0.2$ and various Deborah numbers.	51
3.16 Equilibrium position of a deformable capsule flowing in a microchannel filled with a Newtonian fluid.	52
4.1 Schematic of problem setup	57
4.2 The distribution of cells at (a) $t^* = 0$ and (b) at $t^* = 1800$ for $\phi = 20\%$, $\frac{a}{W} = 0.3$, $La = 500$ and $Re = 37.8$	58

Figure	Page
4.3 Average cell distance from the centerline for $\phi = 10\%$, $\frac{a}{W} = 0.3$ and $Re = 37.8$	59
4.4 Quasi-steady cell distance from the centerline for various La number at $Re = 37.8$	59
4.5 Radial volume fraction for (a) $\phi = 10\%$, $\frac{a}{W} = 0.3$ and $Re = 37.8$ and (b) for $La = 500$ and $Re = 37.8$	61
4.6 Local volume fraction of cells at $\phi = 20\%$, $La = 10$, $\frac{a}{W} = 0.3$ and $Re = 37.8$	62
4.7 The volumetric flow rate of the suspension for various La , ϕ and size at $Re = 37.8$	63
4.8 The velocity profile in the microchannel at $\phi = 10\%$, $\frac{a}{W} = 0.3$ and $Re = 37.8$	64
4.9 Average cell distance for $\phi = 10\%$, $La = 500$ and $\frac{a}{W} = 0.2$ and 0.3	64
4.10 Radial volume fraction distribution for $\phi = 10\%$, $La = 500$ and $\frac{a}{W} = 0.2$	65
4.11 Temporal evolution of cell distance from the centerline for $\phi = 10\%$, $\frac{a}{W} = 0.3$, $La = 500$ and $Re = 37.8$	66
4.12 The distribution of cells at $\phi = 10\%$, $La = 500$, $Re = 37.8$, $\frac{a}{W} = 0.2$ and (a) $Wi = 0$ and (b) $Wi = 2$	67
4.13 Quasi-steady cell distance from the centerline for various Wi number at $Re = 37.8$	68
4.14 Radial volume fraction of cells for $\phi = 10\%$, $\frac{a}{W} = 0.3$ and $Re = 37.8$	69
4.15 (a) Volumetric flow rate of suspension for various Wi number at $Re = 37.8$ and (b) the velocity profile at $\phi = 10\%$, $La = 500$, $\frac{a}{W} = 0.3$ and $Re = 37.8$	70
4.16 Quasi-steady cell distance for various Re number at $\phi = 10\%$, $La = 500$ and $Wi = 2$	70
4.17 The volumetric flow rate at $Re = 100$, $\phi = 10\%$ and $\frac{a}{W} = 0.3$ (a) for $128 \times 76 \times 76$ and $200 \times 133 \times 133$ grid points and (b) for $L_x = 4W$ and $8W$ in x direction	72
5.1 Schematic of the problem setup	79
5.2 Force-map accross the microchannel for $Re = 5$ and (a) $Wi = 0$ and (b) the focusing pattern (stable equilibrium positions) at $Wi = 0$, (c) force-map for $Wi = 0.1$ and (d) the focusing pattern for $Wi = 0.1$, (e) force-map for $Wi = 0.5$ and (f) the focusing pattern at $Wi = 0.5$.	82
5.3 Lateral force profile along the main axis for (a) $Re = 1$ and (b) $Re = 5$.	83

Figure	Page
5.4 Distribution of (a) elastic force and (b) inertial force at $Re = 5$ and $Wi = 0.5$	85
5.5 Velocity profile at (a) the channel inlet and (b) the location of particle center at $Re = 5$ and $Wi = 3$. The stream-wise velocity is defined as $u^* = \frac{u}{U_0}$.86	
5.6 Force-map accross the microchannel for $Re = 10$ and (a) $Wi = 0.1$ and (b) the focusing pattern at $Wi = 0.1$, (c) force-map for $Wi = 0.5$ and (d) the focusing pattern for $Wi = 0.5$, (e) force-map for $Wi = 3$ and (f) the focusing pattern at $Wi = 3$	88
5.7 Lateral force profile on the main axis for $Re = 10$	89
5.8 Distribution of elastic force at $Re = 10$ and (a) $Wi = 0.1$ (b) $Wi = 0.5$ (c) $Wi = 3$ and inertial force at (d) $Wi = 0.1$ (e) $Wi = 0.5$ (f) $Wi = 3$. .	91
5.9 Force profile for (a) $Re = 30$ and (b) the force-map at $Re = 30$ and $Wi = 0.5$.92	
5.10 Distance of the off-center equilibrium points from the channel center along (a) the main axis and (b) the diagonal of the channel. Filled symbols indicate stable equilibrium points and open symbols represent unstable equilibrium points.	93
5.11 (a) The force profile along the main channel for $Wi = 0$ and (b) the stability of channel centerline equilibrium point for a range of Re and Wi numbers	94

ABSTRACT

Raffiee, Amir Hossein Ph.D., Purdue University, December 2019. Elasto-Inertial Migration of Particles and Capsules in Viscoelastic Microchannels. Major Professor: Arezoo M. Ardekani, Sadegh Dabiri.

The motion of synthetic capsules and living cells in microchannels has been the subject of numerous studies in the last decade due to its significance in engineering and biomedical applications. Cell sorting and separation are common processes that are used for various purposes such as separation of leukocytes from blood used in DNA sequencing. Isolation of rare cells in blood is needed for early diagnosis of lethal diseases such as cancer. Cell isolation and enrichment will also provide a better platform to biologists to study and analyze various properties of living cells. Thus, there is a high demand for developing techniques to precisely control trajectories of the cells and manipulate them in a desired manner. Microfluidic devices provide a platform to achieve aforementioned needs while overcoming challenges such as sample contamination, cost and complexity of the procedures. In many of these applications, the background fluid is non-Newtonian due to the presence of DNA and proteins, or polymers are added to control the trajectory of the cells. In this work, we first provide a fundamental study on the dynamics of a single deformable capsule in a viscoelastic matrix under a simple shear flow. Furthermore, we investigate the motion of a single cell and suspension of cells in microchannels. The effects of cell size, inertia, cell volume fraction, cell deformability and fluid elasticity are explored. Our findings on capsule motion in the viscoelastic medium suggest that the use of constant-viscosity viscoelastic fluid pushes the cells toward the channel centerline which can be used in

microfluidic devices used for cell focusing such as cytometers. However, viscoelastic fluid with shear-thinning characteristics and drives the flowing cells toward the channel wall. Particle motion in viscoelastic matrix equilibrium positions of the particle in the microchannel for a wide range of inertial and elastic effects. These fundamental studies can provide insight on the role of rheological properties of the fluid that can be tuned to control the motion of the cells and particles for efficient design of microfluidic devices.

1. INTRODUCTION

Due to the rising application of microcapsules in consumable, pharmaceutical, and medical industries, extensive research focusing on their dynamics has been documented in recent years. Capsules are liquid-filled droplets surrounded by an elastic membrane that are often used in targeted drug and cell delivery [1] applications and encapsulation of volatile substances in lab-on-a-chip devices [2, 3]. In many of these applications, either the background fluid or encapsulated fluid are non-Newtonian due to the presence of DNA, proteins, or polymers [4, 5]. A large number of numerical, experimental and theoretical studies have been conducted on the capsule behavior under various flow fields in a Newtonian fluid [6–10]. These studies suggest that the motion of capsule depends on the imposed flow field, membrane stiffness, shear rate, initial shape and viscosity ratio (the ratio of inner fluid viscosity to the outer fluid viscosity) [6, 7, 11]. The numerical study shows that the capsule that is subject to a simple shear flow deforms to a steady shape and the membrane rotates around it, which is referred to as the Tank-Treading (TT) motion [12]. In this regard, theoretical analysis based on the perturbation method [13, 14] predicts the deformation of initially spherical capsule as well as the Tank-Treading motion of the membrane. The perturbation method is, however, only valid for small deformations. Therefore, numerical solutions are required to address large capsule deformations. The boundary integral, front-tracking [7, 8] and immersed boundary method [9] are among the numerical techniques widely utilized for simulating the capsule dynamics in a shear flow of a Newtonian fluid. In these methods the membrane is discretized using Lagrangian grids which enables us to accurately capture the membrane deformation and

to calculate the elastic force acting on the capsule. These numerical methods have been used to investigate the role of the membrane constitutive laws, area incompressibility and bending resistance [8, 10, 15]. On the other hand, the experimental study on synthetic capsules suspended in a confined shear flow suggests that the membrane starts thinning along the principal strain axes of the shear flow when the shear rate is sufficiently large [16] and its break-up occurs in these areas [11, 16]. Despite numerous studies on the deformation and tank treading motion of capsules in Newtonian fluids, their motion in a viscoelastic fluid is poorly studied. Hence, in chapter 2 we present three dimensional numerical simulations of the dynamics of a Newtonian capsule in a polymeric matrix following an Oldroyd-B fluid constitutive equation as well as dynamics of a polymeric capsule in a Newtonian fluid. A front-tracking method is employed to accurately capture the underlying physics of a deforming capsule in a shear flow for a wide range of Ca and Wi .

1.1 Motion of cells in a microchannel

Separation and focusing of cells are critical processes in biomedical applications [17–20]. In these applications, the samples of interest are mostly composed of various population of cells with different sizes, shapes and properties needed to be isolated, filtered or sorted. These operations are mostly used for diagnostic, therapeutic or biological purposes [21]. For instance, fractionated blood components are used for several diagnostic tests, such as leukocytes (white blood cells) required for hematologic tests [21], isolated reticulocytes and mononucleated red blood cells (RBCs) used for diagnosis of diseases concerned with RBC turnover [22], and purified plasma used for cancer detection [23, 24]. In addition to these components, blood may contain extremely rare cells which their identification is a vital step for diagnosis of lethal diseases. The identification of circulating tumor cells (CTC) [25], malaria [26] and

fetal cells [27] that are present in a limited quantity in blood are of significant importance. Cell isolation is also used for therapeutics such as Platelet transfusion [28], CTC filtration and blood cleansing [21]. Furthermore, providing highly concentrated suspension of homogeneous cells enables biologists to study the biological and physical properties of cells [29] which points out the significance of cell isolation techniques. There are several techniques that use biochemical markers for separation of cells in a heterogeneous population such as Fluorescence-activated cell sorting (FACS) [30] and Magnetic-activated cell sorting (MACS) [31]. These methods are robust, but the complexity of the process and costly procedures required in these techniques prevent them from being widely used in clinical applications. The use of biochemical markers may also affect the natural biological process of cells in targeted samples. Hence, researchers focus on the development of label-free strategies which rely on the intrinsic properties of the cells including size [32], shape [33] and electrical polarizability [34]. One of the main advantages of these techniques is the fact that they are not costly and the users do not need to be highly skilled to work with them. In this chapter 3 we focus on a label-free technique which works based on the hydrodynamic interaction between cells and the surrounding fluid.

Cross-stream migration of particles in a moderate Reynolds number was first observed by Segre and Silberberg [35]. In their experiment the millimeter-sized particles were distributed randomly in a circular tube and they noticed that these particles assembled in an annulus with the radius 0.6 times the tube radius. A similar behavior was also observed for tubes with rectangular and square cross sections [36–39]. Drag and lift forces, acting on the particle surface, drive the particle to a steady equilibrium position. The lift force is the results of two counteractive forces: (i) the inertial lift force that pushes the particle toward the wall due to the shear gradient in the flow field [40] and (ii) the repulsive wall-induced force [41] that drives the particle toward

the channel centerline. The interplay between these two opposing forces determines the final position of the particle in a channel filled with a Newtonian fluid. Several analytical investigations were conducted to explain the dynamics of particles in the flow. These studies used a matched asymptotic expansion technique to obtain a scaling for the lift force [40, 42–45]. Findings of these studies suggest that a particle with diameter a moving in a channel with dimension H experiences a lift force in the form of $F_L = f_L(Re, \frac{x}{L})\rho U^2 a^4/H^2$. In other words, this model predicts that the lift force is a function of particle position and Reynolds number. Although this model is accurate enough to explain the observed particle behavior in Segre and Silberberg experiment, it is only valid for small particle Reynolds numbers and size ratios $\frac{a}{H}$ that significantly restricts its range of applicability [39]. This restriction motivated researchers to conduct numerical and experimental investigations to study various aspects of this phenomenon [45–49]. The suspensions in biomedical and industrial applications mostly contain particles with deformable membranes. These particles have different dynamics compared to rigid particles because of the additional deformability-induced lift force acting on the deformable particles [50]. The interplay between three indicated lift forces determines the transient motion and final position of particles. The underlying physics of migration of deformable particles has been numerically [51, 52] and experimentally [53] investigated. Recently, there has been a growing interest in developing techniques that take advantage of cell deformability to enhance the efficiency of microfluidic devices working with biological fluids [53, 54]. Thus, it is necessary to study the motion of deformable particles, i.e., capsules, vesicles and red blood cells, in a microchannel, but most of the studies in this field have been conducted for rigid particles in a poiseuille flow. The findings of this work provides an insight into the performance of the inertia-based separation techniques and effective parameters that improve the efficiency of these devices for deformable particles.

The current sorting strategies based on inertial migration suffer from a serious restriction which is low flow throughput. The volume flow rate of the samples is limited by two factors: (i) hydrodynamic transition from laminar to turbulent flow in straight microchannels [55] and (ii) the ratio of the Dean drag force to inertial lift that restricts the throughput in curved channels [56]. One of the promising approach to solve this problem is the addition polymers to the fluid. *Lim et al.* [57] showed that their microfluidic device for cell sorting and classification successfully works at $Re \sim 10000$ by adding polymers to the suspending fluid. They added micromolar concentration of hyaluronic acid (HA) to the solution and were able to significantly increase the sample volume flow rate and particle velocity. In this system, the migration behavior of the cells is significantly influenced by the interaction between viscoelastic and inertial lift forces [57,58]. *Del Giudice et al.* [59,60] also investigated the effect of fluid rheology on the dynamics of rigid particles in a microchannel. They showed that the particle focusing in a viscoelastic fluid is enhanced for high flow rates and they quantified the effect of fluid rheological properties on the focusing length of particles. According to previous studies the rheological properties of polymeric fluids can be tuned such that the resulting migration behavior changes in a desired manner for high throughput conditions [58]. Furthermore, the system gives us the ability to control the focal position of cells that enhances the efficiency of the current methods in cell sorting and classification at a very low cost.

In chapter 3, we study the viscoelastic effects of the suspending fluid and its interaction with inertial forces on the migration behavior of deformable cells. We study the focal position of the cells in inertial-based microfluidic devices in polymeric and Newtonian fluids. The role of various fluid rheological parameters are investigated to provide an insight into an efficient design of microfluidic sorting and separation devices.

Despite the importance of the dynamics of cell suspension in a microchannel, previous experimental and computational studies focus on the migration of cells in a very dilute regime. In chapter 4, we focus on the suspension of deformable cells in Newtonian and polymeric fluids in a semidilute regime and investigate the role of various factors including cell size, deformability, inertia and viscoelasticity of the suspending fluid. Our results provide fundamental understanding of the dynamics of suspension of cells in a straight microchannel used in various microfluidic devices.

In chapter 5, we study the mechanism of particle migration in a viscoelastic fluid and provide the results of fully resolved 3D numerical simulations on particle dynamics in a microchannel. We calculate the distribution of lift force acting on the particle in a viscoelastic fluid and investigate the influence of combined elastic and inertial forces on the particle behavior in a microchannel. Furthermore, the location of equilibrium points and their corresponding stability are determined for a wide range of elastic and inertial effects which is important for designing the microfluidic devices relying on viscoelastic effects.

2. DEFORMATION AND BUCKLING OF MICROCAPSULES IN VISCOELASTIC MATRIX

This chapter is reproduced with permission from: A.H. Raffiee, S. Dabiri, A.M. Ardekani, Deformation and buckling of microcapsules in viscoelastic matrix”, Physical Review E, 96(3), 032603. [61]

2.1 Summary

In this chapter, we numerically study the dynamics of (i) a Newtonian liquid-filled capsule in a viscoelastic matrix and that of (ii) a viscoelastic capsule in a Newtonian matrix in a linear shear flow using a front-tracking method. The numerical results for case (i) indicate that the polymeric fluid reduces the capsule deformation and aligns the deformed capsule with the flow direction. It also narrows the range of tension experienced by the deformed capsule for case (i), while the tank-treading period significantly increases. Interestingly, the polymeric fluid has an opposite effect on the tank-treading period and the orientation angle of case (ii), but its effect on the deformation is similar to case (i).

2.2 Governing equations and Numerical methods

2.2.1 Newtonian fluid

In this section, we first present the system of equations governing the motion of a deformable Newtonian capsule in a Newtonian fluid and the mathematical method used for coupling the interfacial interaction between the elastic membrane and the

surrounding fluid. We will then discuss the constitutive equation and the numerical implementation for a viscoelastic fluid. The inner and outer fluids are assumed to be incompressible. Hence, the flow field is governed by the Navier-stokes equations:

$$\nabla \cdot \mathbf{u} = 0, \quad (2.1)$$

$$\frac{\partial(\rho \mathbf{u})}{\partial t} + \nabla \cdot (\rho \mathbf{u} \mathbf{u}) = -\nabla p + \nabla \cdot \boldsymbol{\tau} + \mathbf{F}, \quad (2.2)$$

where ρ is equal to the density of inner (outer) fluid inside (outside) the capsule, p represents the pressure, \mathbf{u} is the velocity vector, t is the time and $\boldsymbol{\tau}$ denotes the total stress tensor. The total stress tensor for a Newtonian fluid is $\boldsymbol{\tau} = \mu \mathbf{D}$, where $\mathbf{D} = (\nabla \mathbf{u}) + (\nabla \mathbf{u})^T$ is the strain rate tensor. In this equation, $\mathbf{F}(\mathbf{x}, t) = \int_{\partial B} \mathbf{f}(\mathbf{x}_i, t) \delta(\mathbf{x} - \mathbf{x}_i) dV$ is the smoothed representation of the membrane force which is zero everywhere except at the interface location. In this formulation, \mathbf{x} and \mathbf{x}_i denote arbitrary points on the Eulerian and Lagrangian grids, respectively, and δ and V represent the Dirac delta function and the volume. Furthermore, $\mathbf{f}(\mathbf{x}_i, t)$ is the elastic force of the membrane. The capsule membrane is modeled as an infinitely thin sheet of elastic material following a neo-Hookean constitutive equation. Therefore, the corresponding strain energy function W is expressed as:

$$W = \frac{E_s}{6} (\epsilon_1^2 + \epsilon_2^2 + \epsilon_1^{-2} \epsilon_2^{-2} - 3), \quad (2.3)$$

where ϵ_1 and ϵ_2 are the principal strains and E_s is the two dimensional elastic shear modulus. The elastic force on the capsule membrane is obtained using the finite element model developed by [62, 63]. In this model, the membrane surface is discretized with triangular elements. The number of surface elements is large enough so that these elements remain approximately flat even after large deformations. The Lagrangian grid is deformed due to the hydrodynamic interaction with the surrounding

fluid and consequently a resistive elastic force develops. The deformed and initially undeformed elements are transformed to a common two dimensional plane to evaluate the displacement of vertices and the corresponding elastic force ($\mathbf{f}(\mathbf{x}_i, t)$) exerted on the membrane using the principle of virtual work, $f = \frac{-dW}{dv}$, where v denotes the displacement of vertices between deformed and undeformed states.

In this work, a finite volume method is used to discretize the equations. The computational domain is discretized using a uniform, Cartesian and staggered grid. The governing equations are solved in the entire domain using an explicit Euler method for time discretization, a third order QUICK (Quadratic Upstream Interpolation for Convective Kinematics) scheme [64] for the convective term and a central difference scheme for the diffusive term. Furthermore, the pressure-velocity coupling is conducted using a projection method [65]. A front-tracking method [66] is used to model the capsule. The computational cost is reduced by solving the Navier-Stokes equations on the entire computational domain rather than solving them separately for each phase and matching the boundary conditions at the interface. Fluid properties (i.e., density and viscosity) are uniform in the interior and exterior fluids but sharply vary in a small region across the interface. To provide a smooth representation of material properties, we solve the Poisson's equation for an indicator function which is used to evaluate fluid properties everywhere in the computational domain. The elastic force is evaluated on the Lagrangian marker points on the interface and are added as a singular body force in the momentum equation to account for the presence of membrane. The velocity field on Lagrangian points are calculated as:

$$\mathbf{u}(\mathbf{x}_i) = \int \mathbf{u}(\mathbf{x}) \delta(\mathbf{x} - \mathbf{x}_i) dV. \quad (2.4)$$

This method requires an interpolation for treating the singular body force in (5.2) and tracking the membrane temporal evolution. Therefore, a smoothed representation of

the delta function is employed to distribute the desired variables with sharp variation across the interface over few grid points surrounding the interface:

$$\delta(x) = D(x)D(y)D(z), \quad (2.5)$$

$$D(x) = \frac{1}{4\Delta}(1 + \cos(\frac{\pi}{2\Delta}(x))), |x| \leq 2\Delta, \quad (2.6)$$

where Δ is the grid size. In summary, a single set of equations is solved in the entire computational domain, taking into account the presence of the membrane and changes in the fluid properties across the interface.

2.2.2 Non-Newtonian fluid

The Oldroyd-B constitutive equation is used to describe the polymeric stress in the inner/outer fluid. The total stress tensor $\boldsymbol{\tau}$ is decomposed into solvent $\boldsymbol{\tau}_s$ and viscoelastic $\boldsymbol{\tau}_p$ stress tensors as follow:

$$\boldsymbol{\tau} = \boldsymbol{\tau}_p + \boldsymbol{\tau}_s, \quad (2.7)$$

where

$$\boldsymbol{\tau}_s = \mu_s \mathbf{D}, \quad (2.8)$$

$$\lambda \overset{\nabla}{\boldsymbol{\tau}}_p + \boldsymbol{\tau}_p = \mu_p \mathbf{D}, \quad (2.9)$$

In this formulation, μ_s and μ_p are the solvent and polymeric viscosity, respectively. The polymer relaxation time, represented by λ , is zero when the fluid is Newtonian

and has a nonzero value when the fluid is viscoelastic. $\overset{\nabla}{\boldsymbol{\tau}}_{\boldsymbol{p}}$ denotes the upper convected time derivative defined as:

$$\overset{\nabla}{\boldsymbol{\tau}}_{\boldsymbol{p}} = \frac{\partial \boldsymbol{\tau}_{\boldsymbol{p}}}{\partial t} + \boldsymbol{u} \cdot \nabla \boldsymbol{\tau}_{\boldsymbol{p}} - \nabla \boldsymbol{u} \boldsymbol{\tau}_{\boldsymbol{p}} - \boldsymbol{\tau}_{\boldsymbol{p}} \nabla \boldsymbol{u}^T. \quad (2.10)$$

We follow the implementation of Aggarwal et al. [67] for the polymeric stress to implement a single constitutive equation in the entire computation domain.

$$\lambda \frac{\partial \boldsymbol{\tau}_{\boldsymbol{p}}}{\partial t} + \boldsymbol{\tau}_{\boldsymbol{p}} = K(t), \quad (2.11)$$

where

$$K(t) = \mu_p \boldsymbol{D} - \lambda (\boldsymbol{u} \cdot \nabla \boldsymbol{\tau}_{\boldsymbol{p}} - \nabla \boldsymbol{u} \boldsymbol{\tau}_{\boldsymbol{p}} - \boldsymbol{\tau}_{\boldsymbol{p}} \nabla \boldsymbol{u}^T), \quad (2.12)$$

This equation is discretized using an explicit Euler scheme for time:

$$\begin{aligned} \boldsymbol{\tau}_{\boldsymbol{p}}(t + \Delta t) = \boldsymbol{\tau}_{\boldsymbol{p}}(t) \exp\left(-\frac{\Delta t}{\lambda}\right) + K(t + \Delta t) - K(t) \exp\left(-\frac{\Delta t}{\lambda}\right) - \exp\left(-\frac{(t + \Delta t)}{\lambda}\right) \\ \int_t^{t+\Delta t} \exp\left(\frac{t}{\lambda}\right) \frac{\partial K}{\partial t} dt \end{aligned} \quad (2.13)$$

We can neglect the integral in (2.13) assuming $\frac{\partial K}{\partial t} = 0$. In this case, the polymeric stress tensor can be written as:

$$\boldsymbol{\tau}_{\boldsymbol{p}}^{n+1} = \boldsymbol{\tau}_{\boldsymbol{p}}^n \exp\left(-\frac{\Delta t}{\lambda}\right) + K^n \left(1 - \exp\left(-\frac{\Delta t}{\lambda}\right)\right) \quad (2.14)$$

2.3 Problem setup

In this study, we simulate the deformation of an initially spherical, unstressed capsule which is introduced to the flow at time $t=0$. The capsule is deformed under a linear shear flow bounded by two infinitely long flat plates as shown in Fig.2.1.

Accordingly, the undisturbed velocity field in the absence of the capsule is described as:

$$U = \dot{\gamma}(Z - \frac{H}{2}), V = W = 0, \quad (2.15)$$

where U, V and W denote the velocity of the fluid in the streamwise direction (X), wall normal direction (Z) and vorticity direction (Y), respectively. In this formulation $\dot{\gamma}$ and H represent the imposed shear rate and the distance between the parallel walls. The computational domain is a rectangular box with the size of $10R \times 5R \times 10R$ (R is the initial capsule radius) in the streamwise, wall normal and vorticity directions, respectively. The computational domain is discretized using a uniformly distributed $128 \times 64 \times 128$ Eulerian grid points. The capsule membrane is also discretized with 8120 triangular elements. A periodic boundary condition is imposed in X and Y directions and a no-slip boundary condition is considered on the upper and lower walls. The interior fluid of the capsule is incompressible and Newtonian while the exterior fluid is viscoelastic, following an Oldroyd-B constitutive equation. The characteristic length and time scales are R and $\dot{\gamma}^{-1}$, respectively, leading to the following dimensionless parameters: (i) Reynolds number $Re = \frac{\rho \dot{\gamma} R^2}{\mu}$, which represents the ratio of the inertial force to the viscous force (ii) Capillary number $Ca = \frac{\mu \dot{\gamma} R}{E_s}$, denoting the ratio of the viscous force to the elastic force on the capsule membrane (iii) Weissenberg number $Wi = \lambda \dot{\gamma}$, and (iv) $\beta = \frac{\mu_p}{\mu}$, indicating the ratio of the polymeric viscosity to the total viscosity. The total viscosity is defined as the sum of polymeric viscosity and solvent viscosity of the fluid ($\mu = \mu_p + \mu_s$). The interior and exterior fluids are assumed to have the same density and total viscosity. The values of β and Re are set to $\beta = 0.5$ and $Re = 0.1$, unless otherwise stated.

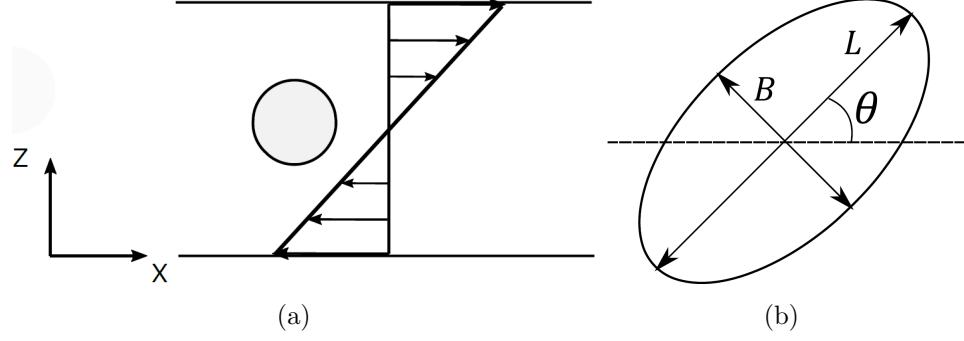


Fig. 2.1. Schematic of the problem and coordinate system

2.4 Numerical verification

In this section, we compare our numerical results against previously published numerical results of [68] and [69], where front-tracking and boundary element methods were used, respectively. For this purpose, we simulate the deformation of a Neo-Hookean membrane in a linear shear flow, where the interior and exterior fluids are Newtonian. In order to conduct a quantitative comparison, the Taylor deformation parameter $D = (L - B)/(L + B)$ and orientation angle θ are evaluated, where L and B are the major and minor axes of the deformed capsule in the shear plane and θ represents the angle between the major axis of ellipsoid and the X -axis. Fig.2.2 shows steady-state values of deformation parameter D and orientation angle θ for various Ca . The results agree well with the published results in the literature.

The numerical convergence of the solution is investigated by increasing the grid resolution from $64 \times 32 \times 64$ to $160 \times 80 \times 160$. The temporal evolution of the deformation parameter and orientation angle for $Ca = 0.2$ and $Wi = 2$ are shown in Fig.2.3. This figure shows that the capsule deformation does not depend on the grid resolutions used here, while the orientation angle converges by increasing the grid resolution. Henceforth, we choose $128 \times 64 \times 128$ grid points.

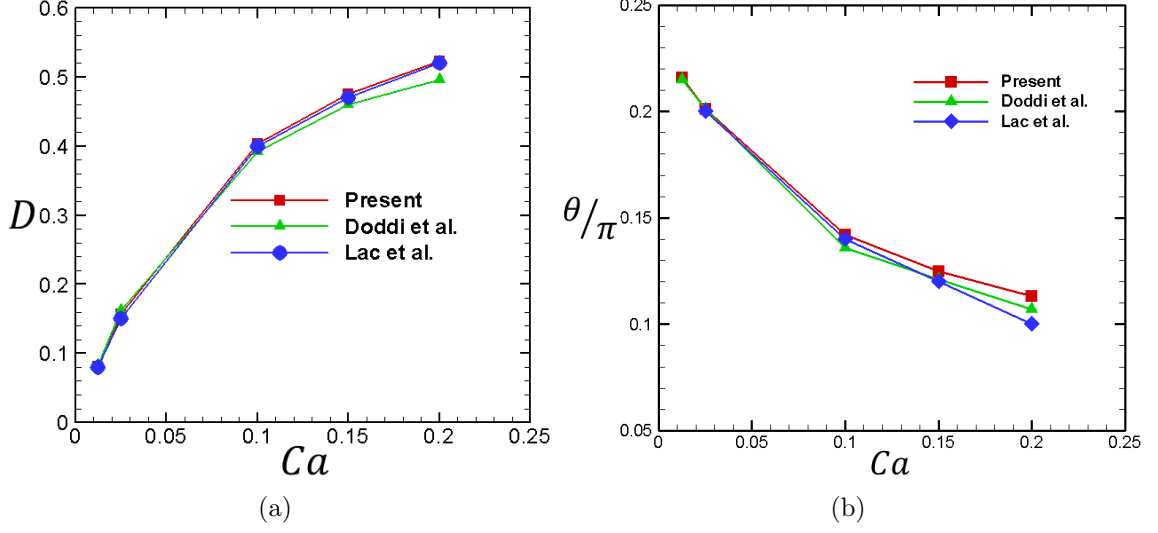


Fig. 2.2. A comparison of (a) the capsule deformation parameter and (b) orientation angle with the results of Doddi et al. [69] and Lac et al. [68].

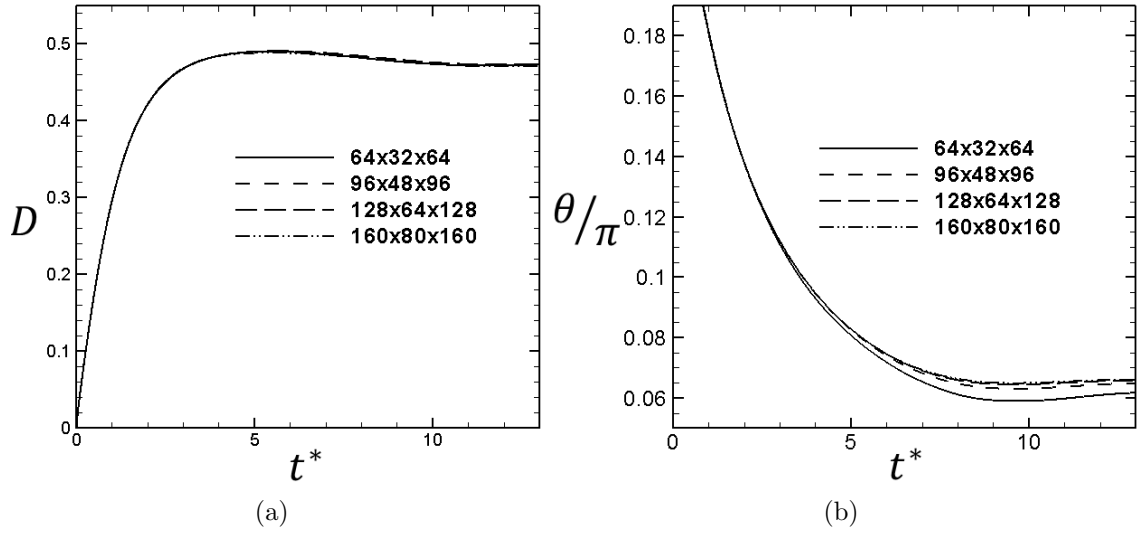


Fig. 2.3. Temporal evolution of (a) the capsule deformation and (b) transient orientation angle at $Ca=0.2$ and $Wi=2$

2.5 Transient dynamics of a viscoelastic capsule in a Newtonian fluid

When the capsule is released at the center of a linear shear flow, the membrane deforms and elongates due to the hydrodynamic interaction with the surrounding

fluid. The deformation grows until it reaches a steady state, when no further change is observed in the final deformed shape and inclination angle. The Lagrangian nodes on the capsule continuously rotate on the deformed capsule which is called tank-treading mode (referred to as TT). The temporal evolution of three main axes of the deformed membrane ($L^* = \frac{L}{R}$, $B^* = \frac{B}{R}$ and $W^* = \frac{W}{R}$) are plotted in Fig.2.4.c for $Ca = 0.1$ and various values of Wi . In this plot, L^* is the dimensionless semi-major axis

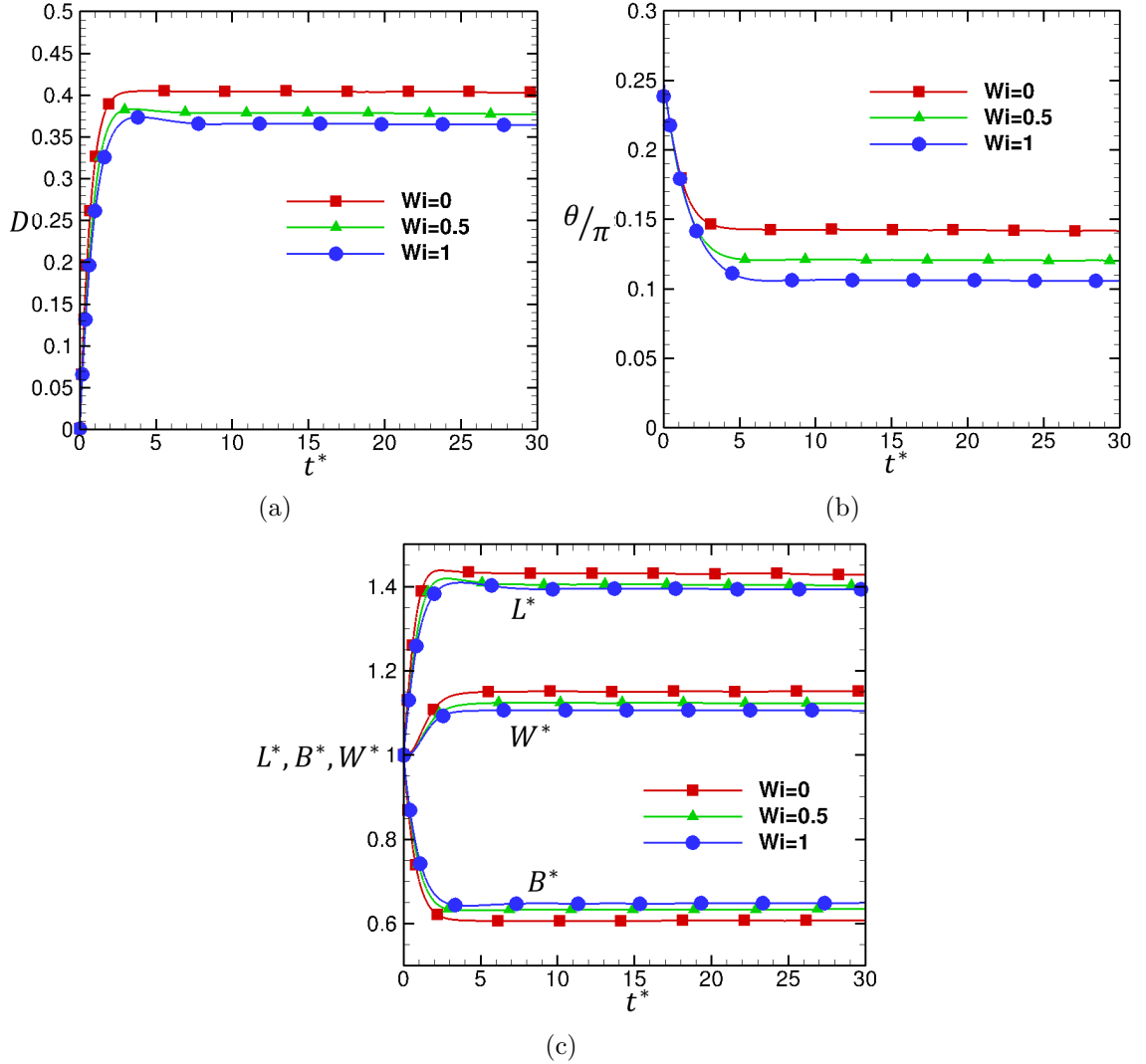


Fig. 2.4. Temporal evolution of (a) the capsule deformation, (b) orientation angle and (c) length of main axes at $Ca = 0.1$

and B^* is the dimensionless semi-minor axis in the shear plane and W^* denotes the dimensionless semi-axis of the capsule in the vorticity direction. The capsule elongates in two directions and compresses in the wall normal direction for both Newtonian and viscoelastic fluids. It should be noted that increase in Wi hinders stretching of L^* and W^* as well as the compression of B^* . This means that the surrounding viscoelastic fluid reduces the capsule deformation and orientation angle due to large polymeric stresses developed in the outer fluid (Fig.2.4.a-b). As illustrated in Fig.2.4.a, an overshoot is observed in the deformation of the membrane when the outer fluid is viscoelastic at $Wi = 0.5$ and 1 . This phenomenon is attributed to the relaxation time of the outer viscoelastic fluid leading to a delay in the development of the polymeric stress. Consequently, the membrane deformation is larger than its steady values. Additionally, as the Weissenburg number increases the orientation angle of the capsule in a shear flow decreases and it reaches the equilibrium state at a longer time.

2.5.1 Capsule deformation in a low capillary number regime

In this section, we investigate the dynamics of a sheared capsule in a low capillary number regime. The temporal evolution of the capsule deformation parameter for different Weissenburg numbers at $Ca=0.025$ is shown in Fig. 2.5.a. The deformation increases and reaches an equilibrium value, following by small amplitude oscillations. These oscillations are caused by the formation of folds on the membrane surface which is discussed later in this section. The membrane deformation in this low capillary number regime decreases with Weissenburg number similar to the observation in the previous section. However, the fluid elasticity does not have the same effect for the entire range of Wi considered here. The reduction in the steady deformation is observed for $Wi \in [0, 2]$. On the other hand, the capsule deformation monotonically

increases for larger Wi numbers (e.g., $Wi = 5$). This behavior was also observed for

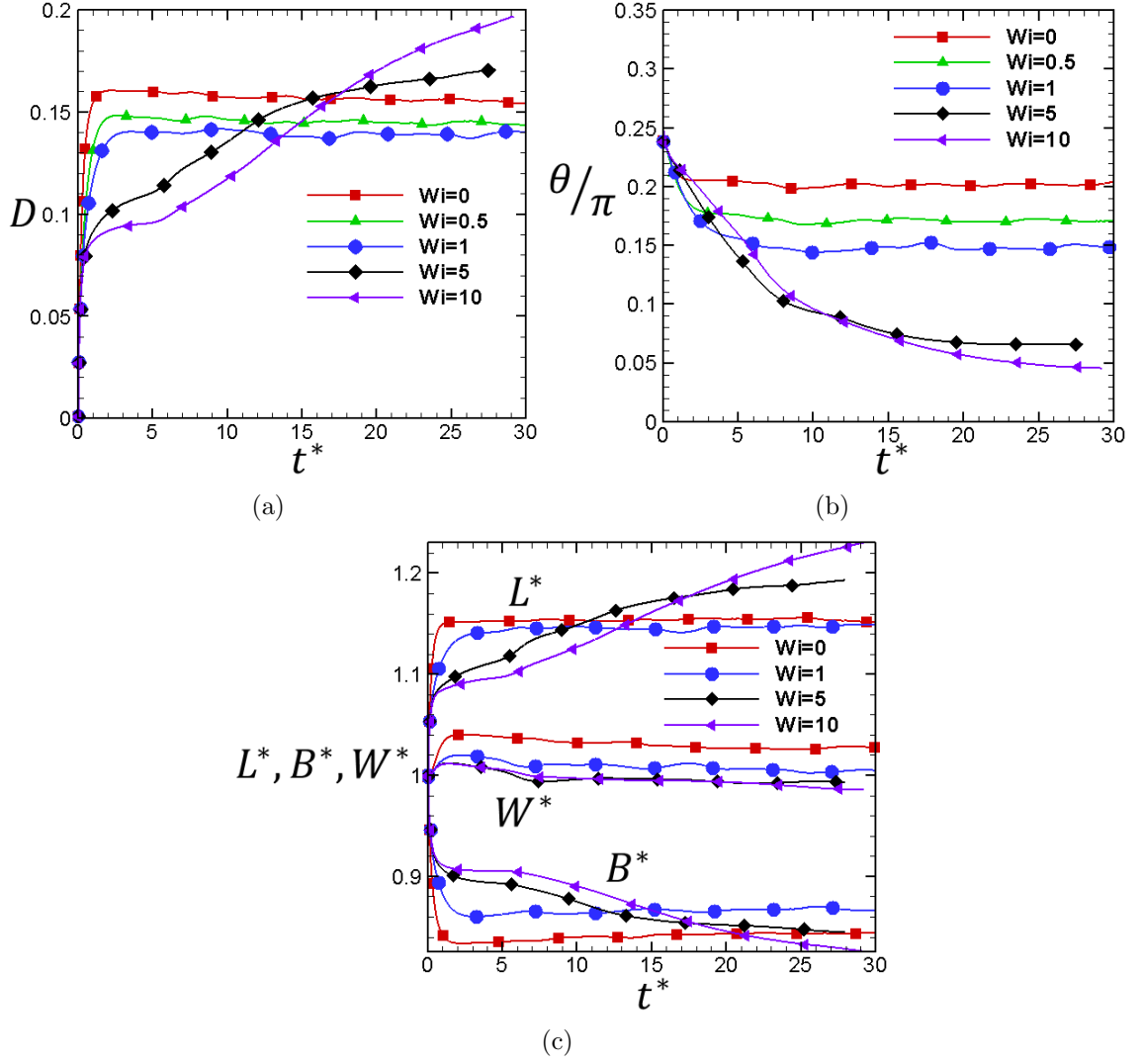


Fig. 2.5. The temporal evolution of (a) the capsule deformation, (b) orientation angle and (c) axes length for $Ca = 0.025$

droplets suspended in a shear flow. The reason for this unexpected behaviour can be attributed to the memory and nonlinearity of the Oldroyd-B fluid as a similar trend exists for the variation of the drag coefficient of a cylinder with increasing Wi [67]. In order to explore the deformation of capsule in more detail, the transient lengths of major and minor axes are plotted in Fig.2.5.c. The elongation of L^* and compression

of B^* reduces for cases with steady-state deformations. However, at $Wi = 5$, L^* and B^* monotonically increase in time, while the vorticity-directed axis (W^*) has an infinitesimal change in this case. Increase in the fluid elasticity causes the capsule to get more aligned with the flow direction. The orientation angle monotonically decreases with the Weissenberg number for the entire range of Wi investigated in this work. This is in contrast to the elasticity effects on the deformation where it decreases for low weissenberg numbers, but is unstable for Wi above a certain threshold. The folds on the capsule surface are illustrated in Fig.2.6 for various Wi .

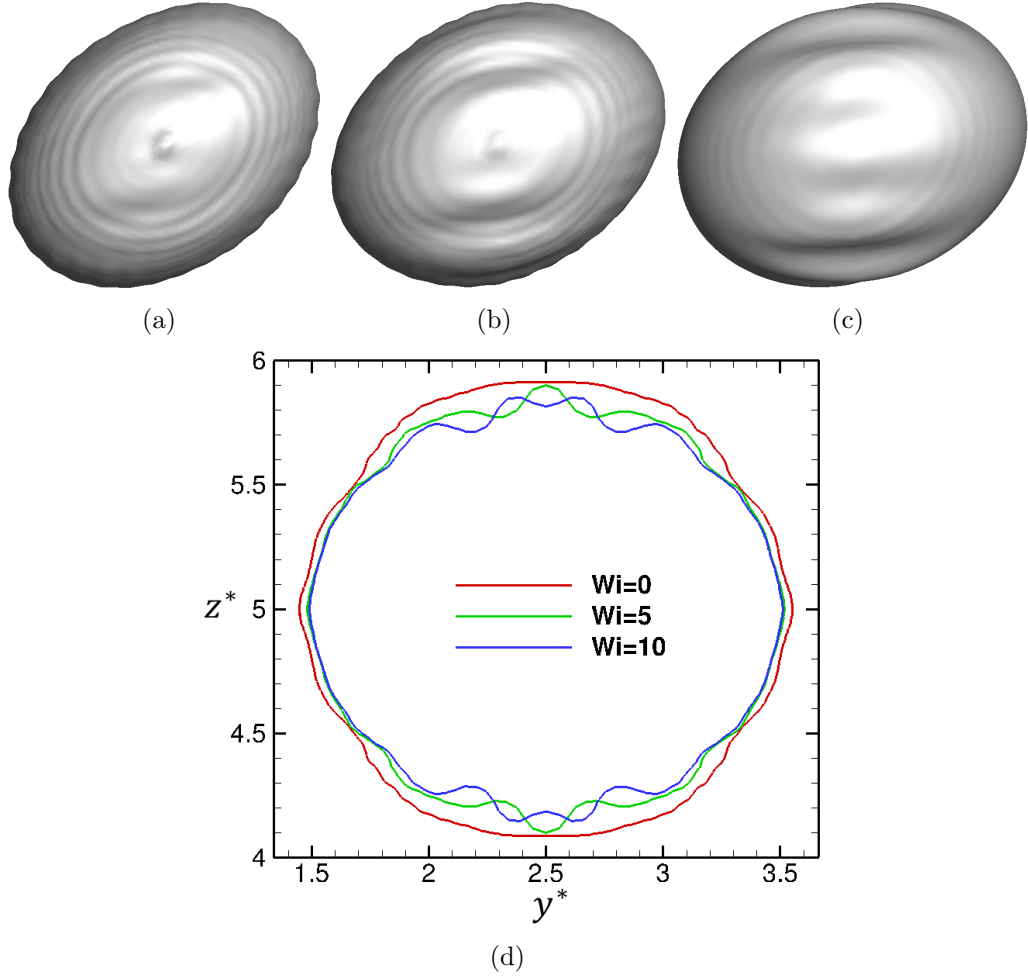


Fig. 2.6. The deformation of capsule membrane at $Ca = 0.025$ and (a) $Wi=0$ (b) $Wi=5$ (c) $Wi=10$ and (d) The cross section of the capsule membrane for different Weissenberg numbers

One of the important parameters in cell biology is the maximum tension experienced by the cell membrane. If maximum tension exceeds a threshold the cell membrane bursts and releases its content which has harmful effects on the function of biological systems. The effects of principal tension on mechanotransduction of biological cells have become the subject of recent studies [70]. Therefore, it is important to study the evolution of maximum and minimum tension on the membrane. To do so, the principal elastic tensions are computed on each triangular element on the membrane which is used to evaluate the range of experienced tension at each time step. According to Li et. al [7] the principal tension on each element, represented by T_1 and T_2 , are explicitly written as:

$$T_1 = \frac{1}{\epsilon_2} \frac{dW}{d\epsilon_1} = \frac{E_s}{3\epsilon_1\epsilon_2}(\epsilon_1^2 - \epsilon_1^{-2}\epsilon_2^{-2}) \quad (2.16)$$

$$T_2 = \frac{1}{\epsilon_1} \frac{dW}{d\epsilon_2} = \frac{E_s}{3\epsilon_1\epsilon_2}(\epsilon_2^2 - \epsilon_1^{-2}\epsilon_2^{-2}) \quad (2.17)$$

By finding the values of T_1 and T_2 on each element the maximum and minimum principal tension on the membrane can be computed. The temporal evolution of maximum and minimum tensions for different Wi at $Ca=0.025$ is illustrated in Fig. 2.7. The increase in Wi decreases the maximum and increases the minimum tensions, indicating that the range of the tension experienced by the capsule decreases with Wi .

2.5.2 Capsule deformation in a moderate capillary number regime

The deformation of a capsule is plotted in Fig. 2.8.a for $Ca = 0.2$ and various Wi . Numerical simulations predict that the steady-state deformation decreases with increasing Wi number. This behavior changes for larger Wi number such that the deformation starts increasing with increasing fluid elasticity. The reason for this

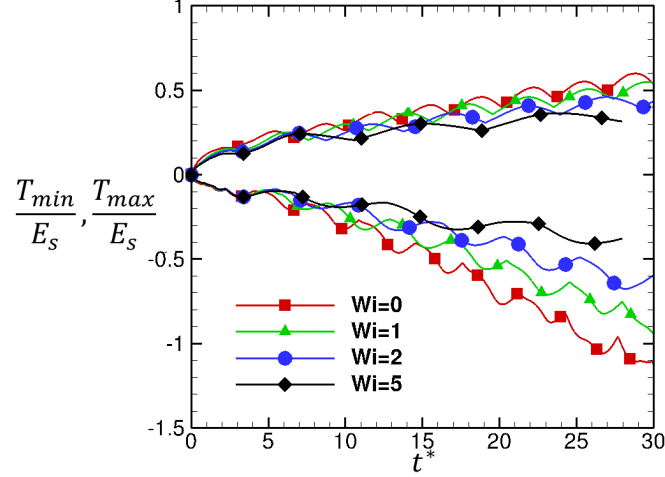


Fig. 2.7. The temporal evolution of maximum and minimum principal tensions at $Ca = 0.025$

complex phenomenon is the nonlinearity of the fluid as discussed in the previous section. The temporal evolution of orientation angle, plotted in Fig. 2.8.b, shows the effect of fluid elasticity on the membrane inclination angle. The deformed shaped of the capsule in Newtonian and viscoelastic surrounding fluids is represented in Fig.2.9. The resulting membrane develops high-curvature tips due to the large viscous stretching exerted by the flow field on the membrane in a Newtonian fluid, while these tips are less sharp as Wi increases. This phenomenon is more prominent for larger Wi . The effect of fluid elasticity on the deformation and orientation angle are shown in Fig.2.10. The deformation increases with Ca as expected and fluid elasticity reduces the capsule deformation particularly for large Wi . The effect of the fluid elasticity on the deformation is negligible at small Ca but it has a significant effect on the orientation angle. The capsule aligns more with the flow direction as fluid elasticity increases. In order to study TT behavior of a deformed capsule the tank-treading period (TTP) is defined as the time required by the material points on the membrane to complete a circulation. Therefore, we choose an arbitrary material point located on the shear plane and track its position and angle with the X-direction to quantify

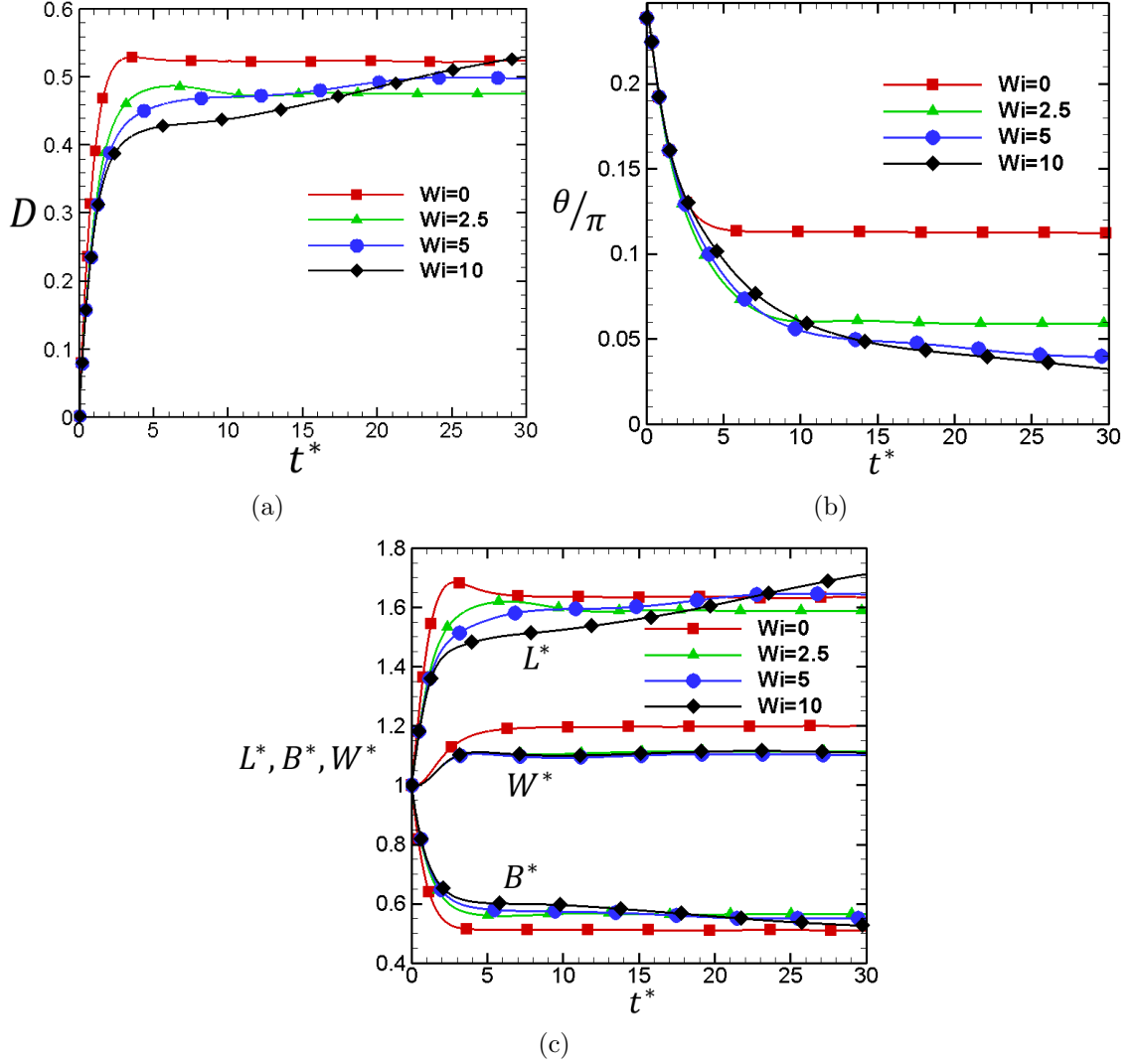


Fig. 2.8. The temporal evolution of the (a) capsule deformation, (b) orientation angle, and (c) axes length for $Ca=0.2$

the time period. Fig.2.11 shows the effect of Wi on the TTP compared to the one in a Newtonian fluid. This ratio is always larger than unity, which implies that the fluid elasticity of the outer fluid slows down the rotational velocity of the deformed membrane leading to a larger TTP. As we know the TTP is prolonged at higher Ca because the membrane is highly deformed and the material points circulate a larger

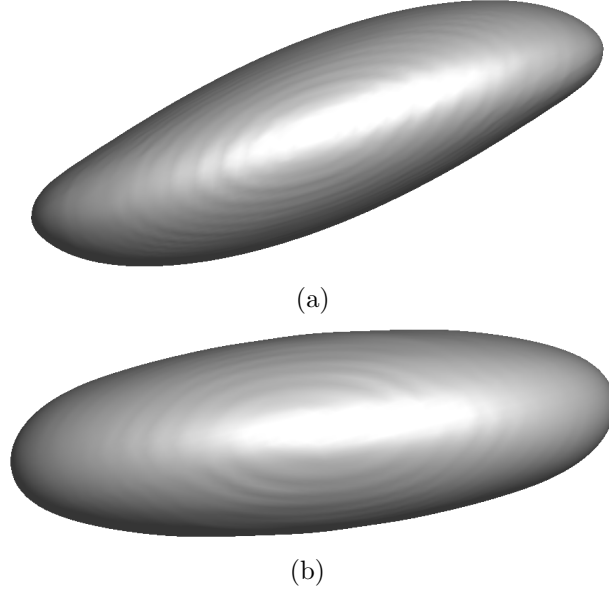


Fig. 2.9. Deformed capsule at $Ca = 0.2$ and (a) $Wi = 0$ (b) $Wi = 5$

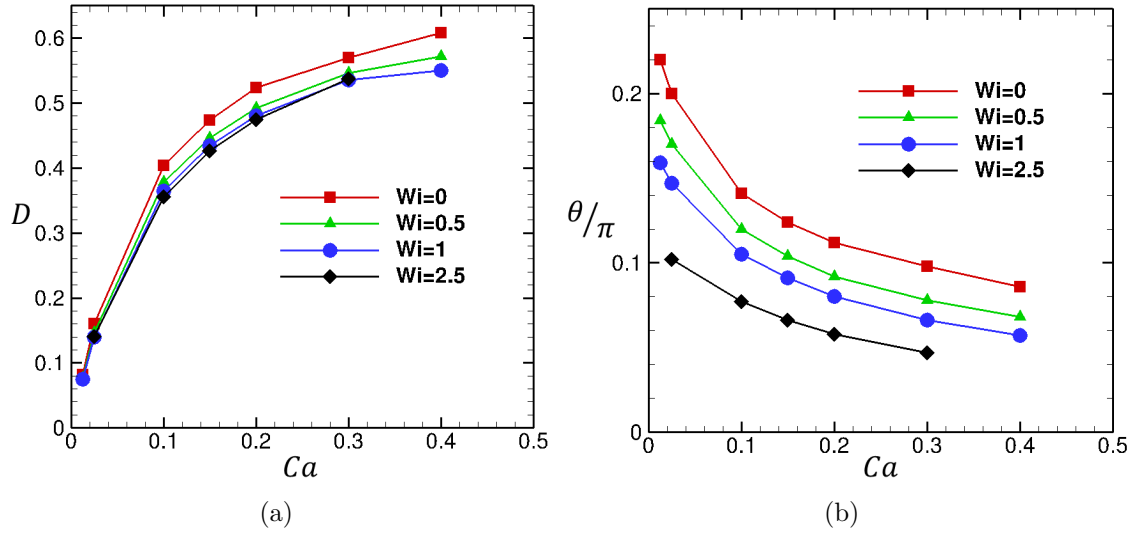


Fig. 2.10. (a) The capsule deformation and (b) inclination angle versus capillary number

distance to complete an orbit. According to Fig.2.11, the relative change in TTP caused by fluid elasticity reduces as Ca increases.

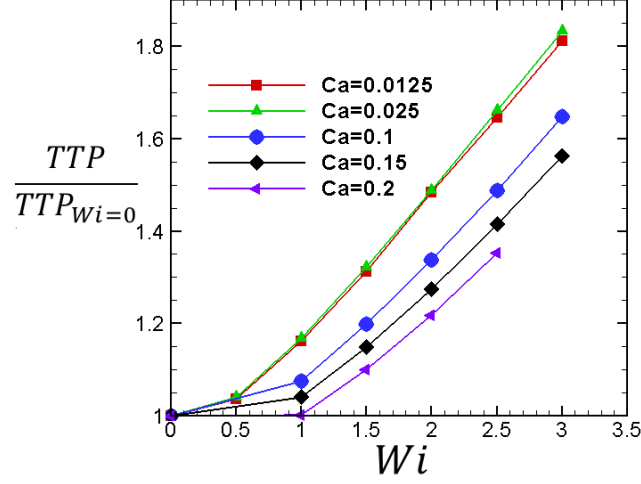


Fig. 2.11. The normalized value of the tank treading period versus Wi

2.6 Viscoelastic capsule in a Newtonian matrix

In this section, we investigate the dynamics of a viscoelastic liquid-filled capsule suspended in a Newtonian fluid. The effect of inner polymeric fluid on the deformation is shown in Fig. 2.12 for a range of Wi . The steady value of deformation decreases for $Wi \in [0, 2]$ and increases for any value outside of this range (Fig. 2.12.a and b). Furthermore, the overshoot observed in the deformation parameter can be attributed to the polymer relaxation time as explained in the previous section. The effect of the inner viscoelastic fluid is of the order of 3-4% on the deformation parameter which proves negligible effects of fluid elasticity compared to the case where the outer fluid is viscoelastic (Fig. 2.12.b). The viscoelastic fluid is bounded in a finite volume of capsule and can not have a significant effect on the deformation parameter as that of the previous cases. On the other hand, the fluid elasticity has a more appreciable effect on the angle as shown in Fig.2.13. Contrary to the deformation, polymer increases the orientation angle for $Wi \leq 6$ for $Ca = 0.2$ (Fig.2.13.a and b). The effect of fluid elasticity on the dynamics of the deforming capsule is enhanced for larger Ca (Fig.2.13.b). The tank-treading period of the viscoelastic capsule is shown

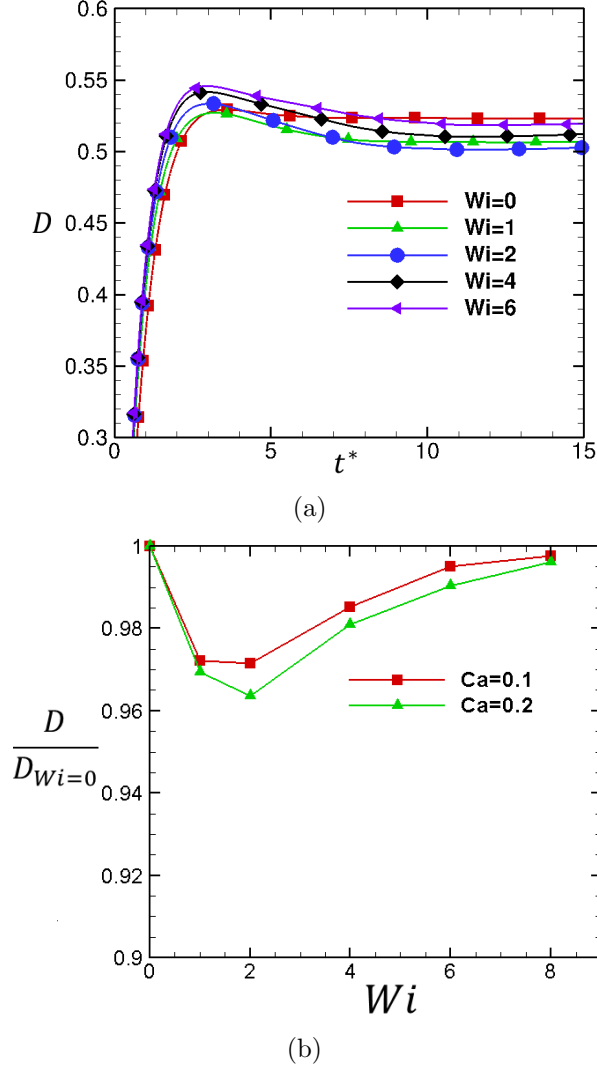


Fig. 2.12. Temporal evolution of (a) deformation for $Ca = 0.2$ and (b) normalized deformation as a function of Wi

in Fig.2.14. Interestingly, this parameter decreases in the presence of inner fluid elasticity which indicates faster rotational velocity of the capsule membrane. This behaviour is opposite to the effect of fluid elasticity on the TTP when the outer fluid is viscoelastic. As the Ca increases, the TTP decreases more significantly compared to that of a Newtonian fluid.

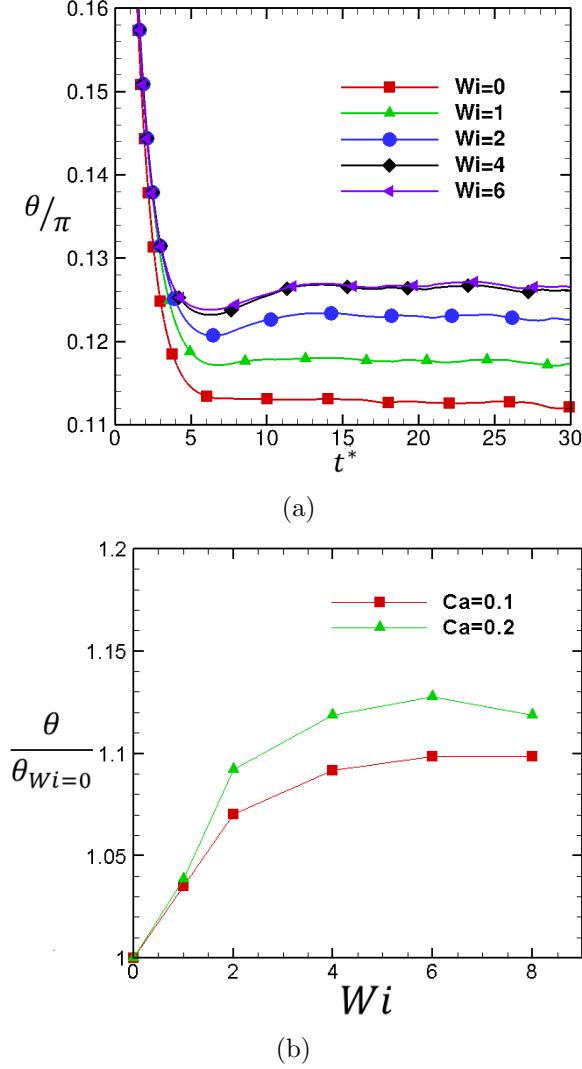


Fig. 2.13. Temporal evolution of (a) orientation angle for $Ca = 0.2$ and (b) normalized orientation angle as a function of Wi

2.7 Conclusion

We have simulated a Newtonian capsule in a viscoelastic matrix as well as a viscoelastic capsule in a Newtonian matrix to investigate the dynamics of a deformed capsule suspended in a shear flow using a front-tracking method. The deformation of the sheared capsule is such that the major axis in the shear plane and the axis in the vorticity direction are elongated, while the minor axis in the shear plane is com-

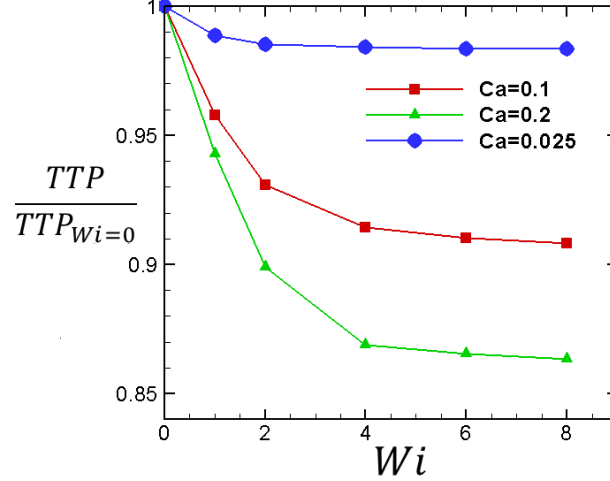


Fig. 2.14. The normalized value of tank treading period versus Wi

pressed. The numerical results show that the outer fluid elasticity reduces the capsule deformation and orientation angle of the capsule with the streamwise direction. The capsule has a steady-state deformation for low Weissenberg numbers and when Wi exceeds a threshold, the capsule deformation increases with time. Furthermore, the deformation curves display small amplitude oscillations in the low capillary regime which is due to the folds developed on the capsule membrane. Other important parameters investigated in this work are the maximum and the minimum tensions experienced by the capsule. According to the results, the range of the tension generated on the membrane decreases with Wi . The TTP calculated for the deforming capsule increases with Wi . This means that the fluid elasticity slows down the rotational velocity of the membrane and this effect is more prominent for smaller Ca . The numerical results for a viscoelastic liquid-filled capsule in a Newtonian matrix also indicate the decrease in the deformation with Wi , but interestingly the TTP and orientation angle increase, which is opposite to the capsule dynamics observed in a viscoelastic matrix.

3. ELASTO-INERTIAL MIGRATION OF DEFORMABLE CAPSULES IN A MICROCHANNEL

This chapter is reproduced with permission from: A.H. Raffiee, S. Dabiri, A.M. Ardekani, Elasto-inertial migration of deformable capsules in a microchannel”, *Biomicrofluidics*, 11(6), 064113. [71]

3.1 Summary

Cell classification and sorting are of importance in many biomedical applications. The current methods suffer from various problems such as complexity of the process, low-throughput, and costly procedures that limit the use of these technologies. In this chapter, we study the dynamics of deformable cells in a channel flow of Newtonian and polymeric fluids and unravel the effects of deformability, elasticity, inertia and size on the cell motion. We investigate the role of polymeric fluids on the cell migration behavior and the performance of inertial microfluidic devices. Our results show that the equilibrium position of the cell is on the channel diagonal, in contrary to that of rigid particles, which is on the center of the channel faces. A constant-viscosity polymeric fluid, modeled using an Oldroyd-B constitutive equation, drives the cells toward the channel centerline, while a shear-thinning polymeric fluid, modeled using a Giesekus constitutive equation, pushes the cells toward the channel wall. The findings of this paper suggest that the addition of polymers in microfluidic devices can be used to enhance the throughput of cell focusing and separation at a low cost. This study provides an insight on the role of rheological properties of the fluid and the ways that they can be tuned to control focal position of the cells.

3.2 Methodology

3.2.1 Governing equations

The system of equations governing the flow and the motion of an elastic capsule in a Newtonian fluid is presented in this section. The inner and outer fluids are assumed to be incompressible. Hence, we have:

$$\nabla \cdot \mathbf{u} = 0, \quad (3.1)$$

$$\frac{\partial(\rho \mathbf{u})}{\partial t} + \nabla \cdot (\rho \mathbf{u} \mathbf{u}) = -\nabla p + \nabla \cdot \boldsymbol{\tau} + \mathbf{F}, \quad (3.2)$$

where ρ is the density of the inner and outer fluids, \mathbf{u} is the velocity vector, t represents the time and p and $\boldsymbol{\tau}$ denote the pressure and the total stress tensor, respectively. The total stress tensor in a Newtonian fluid is calculated by $\boldsymbol{\tau} = \mu \mathbf{D}$, where μ is the viscosity and $\mathbf{D} = (\nabla \mathbf{u}) + (\nabla \mathbf{u})^T$ is the strain rate tensor. In equation (5.2), F represents the smoothed elastic force exerted by the capsule membrane which is calculated as:

$$\mathbf{F}(x, t) = \int_{\partial B} \mathbf{f}(x_i, t) \delta(x - x_i) dV. \quad (3.3)$$

This force represents the membrane response to the surrounding fluid which is zero everywhere except on the membrane. In this equation, x and x_i denote arbitrary points in the computational domain and membrane surface and δ and V are the Dirac delta function and volume, respectively, that have been explained in previous chapter. In equation 5.3, f is the response force due to the shear deformation and area dilatation resistance of the capsule membrane. We use the Shalak model [72] to

include the resistive force of the membrane. In this model, the following strain energy function is assigned to the membrane:

$$W = \frac{E_s}{12}((\epsilon_1^2 + \epsilon_2^2 - 2)^2 + 2(\epsilon_1^2 + \epsilon_2^2 - 2) - 2(\epsilon_1^2 \epsilon_2^2 - 1)) + \frac{E_a}{12}(\epsilon_1^2 \epsilon_2^2 - 1)^2, \quad (3.4)$$

where ϵ_1 and ϵ_2 are principal strains and E_s and E_a represent the shear and area dilatation moduli, respectively. Following Krüger et al. [73], we assume a fixed ratio for $\frac{E_a}{E_s} = 2$. We use a finite element method [62] to obtain the interfacial force f . We have validated this model in our previous work [61].

Biological fluids are often complex fluids due to the presence of polymers, proteins, and DNA molecules. In order to model viscoelastic complex fluids, the total stress tensor in (5.2) is split into solvent stress tensor ($\boldsymbol{\tau}_s$) and polymeric stress tensor ($\boldsymbol{\tau}_p$) as follow:

$$\boldsymbol{\tau} = \boldsymbol{\tau}_s + \boldsymbol{\tau}_p, \quad (3.5)$$

where the solvent stress tensor $\boldsymbol{\tau}_s$ is:

$$\boldsymbol{\tau}_s = \mu_s \mathbf{D}, \quad (3.6)$$

where μ_s is the solvent viscosity. The nonlinear elastic properties of complex fluids can be modeled using the Giesekus constitutive equation [74], which captures both effects of fluid elasticity and shear-thinning behavior. The Giesekus constitutive equation is written as:

$$\lambda \overset{\nabla}{\boldsymbol{\tau}_p} + \boldsymbol{\tau}_p + \frac{\alpha \lambda}{\mu_p} \boldsymbol{\tau}_p \cdot \boldsymbol{\tau}_p = \mu_p \mathbf{D}. \quad (3.7)$$

In this equation, μ_p is the polymeric viscosity and α denotes the mobility factor, which is in the range of $0 < \alpha < 0.5$ [75]. If α is set to zero, the polymeric fluid follows an Oldroyd-B model, which behaves like a constant-viscosity elastic fluid. Furthermore,

λ is the relaxation time of polymeric fluid and $\overset{\nabla}{\tau}_p$ denotes the upper convected time derivative defined as:

$$\overset{\nabla}{\tau}_p = \frac{\partial \tau_p}{\partial t} + \mathbf{u} \cdot \nabla \tau_p - \nabla \mathbf{u} \tau_p - \tau_p \nabla \mathbf{u}^T. \quad (3.8)$$

The first and second normal stress differences in a viscoelastic polymeric fluid, defined below, can lead to flow phenomena in contrast with their counterpart in Newtonian fluids.

$$N_1 = \tau_{xx} - \tau_{yy} \quad (3.9)$$

$$N_2 = \tau_{zz} - \tau_{yy} \quad (3.10)$$

where τ_{xx} , τ_{yy} and τ_{zz} represent the normal stresses along the x , y and z directions, respectively.

3.2.2 Problem setup

We consider the motion of a deformable capsule in a straight square channel with the edge length of $2W$ and the channel length of $4W$ illustrated in Fig.3.1. A constant pressure gradient is applied in the x direction, leading to a parabolic Poiseuille flow. The periodic boundary condition is applied in the x direction and the no-slip boundary condition is applied in the y and z directions. In this study, we consider W and U_0 (the centerline velocity of the channel filled with a Newtonian fluid) as the length and velocity scales, respectively. The dynamics of motion of the capsule is governed by the following dimensionless parameters: (i) Reynolds number $Re = \frac{\rho U_0 2W}{\mu}$, representing the ratio of the inertial to the viscous force (ii) Laplace number $La = \frac{2\rho E_s a}{\mu^2}$, denoting the deformability of the cell (iii) Weissenberg number $Wi = \frac{\lambda U_0}{W}$, which is defined as a function of polymer relaxation time, length and

velocity scales, (iv) $\beta = \frac{\mu_p}{\mu}$, representing the ratio of the polymeric viscosity to the total viscosity. The total viscosity is defined as $\mu = \mu_s + \mu_p$. (v) Aspect ratio $AR = \frac{a}{W}$, representing the blockage of the channel by the capsule. Unless otherwise stated $Re = 37.8$. The blockage ratio is set to 0.2 and 0.3 to study the effect of the capsule size on its cross-streamline motion. The fluid inside the cell is assumed to be Newtonian, and its viscosity and density are equal to the total viscosity and density of the outer fluid ($(\mu_s + \mu_p)_{outer} = (\mu_s)_{inner}$ and $\rho_{inner} = \rho_{outer}$). Unless otherwise stated, β is set to 0.9 in polymeric fluids. The initial viscoelastic stress in the domain is zero in all simulations. The cells are assumed to have spherical initial shape and they are released at $\frac{y}{W} = 1.5$ and $\frac{z}{W} = 1.3$. Furthermore, in the case of polymeric fluid the initial viscoelastic stress is zero. The computational domain is discretized using two sets of uniformly distributed Eulerian grids. For the cases corresponding to $Re = 37.8$, we use $128 \times 76 \times 76$ grid points and for higher Reynolds numbers, we use $200 \times 128 \times 128$ grid points. The mesh independency tests are included in the Appendix. The capsule surface is discretized using 21632 triangular elements to accurately track the location of the membrane. Furthermore, according to Euler explicit method for time discretization the time step is restricted by CFL number, which is set to 0.9.

3.3 Results and discussion

3.3.1 Cell focusing in a Newtonian fluid

In this section, we study the dynamics of a cell moving in a Newtonian fluid. The blockage ratio is set to $\frac{a}{W} = 0.2$ and 0.3 and the Laplace number varies between 1 to 500.

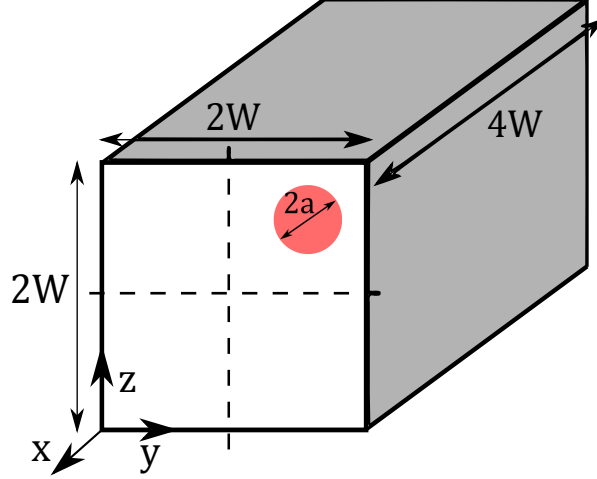


Fig. 3.1. Schematic of the microchannel.

The trajectories and the time history of distance from the channel centerline are illustrated in Fig. 4.2 for various Laplace numbers. All the cells are released from the same location in the channel. The motion of cells can be described by two phases. In the first phase, cells migrate toward the diagonal until they reach it and then they move slowly along the diagonal until they reach their equilibrium position represented with symbols in Fig. 4.2(b). One of the main differences between solid particles and deformable cells in the microchannel is the equilibrium position. According to Fig. 4.2(b), the equilibrium position for deformable cells lies on the diagonal which is in agreement with a previous study [54]. On the other hand, experimental and numerical investigations [76] show that solid particles focus onto four off-center points on the main axes near the channel edges. This difference in the final equilibrium position can be used for sorting cells with different deformability. Figure 4.2 (a) shows that the cells with $La = 1$ and 10 migrate to the channel center. The final position of less deformable cells approaches the channel wall and their distance from the center increases. A similar behavior is observed for the cells with $\frac{a}{W} = 0.2$ in which only the very soft cells with $La = 1$ move to the center and the equilibrium position for

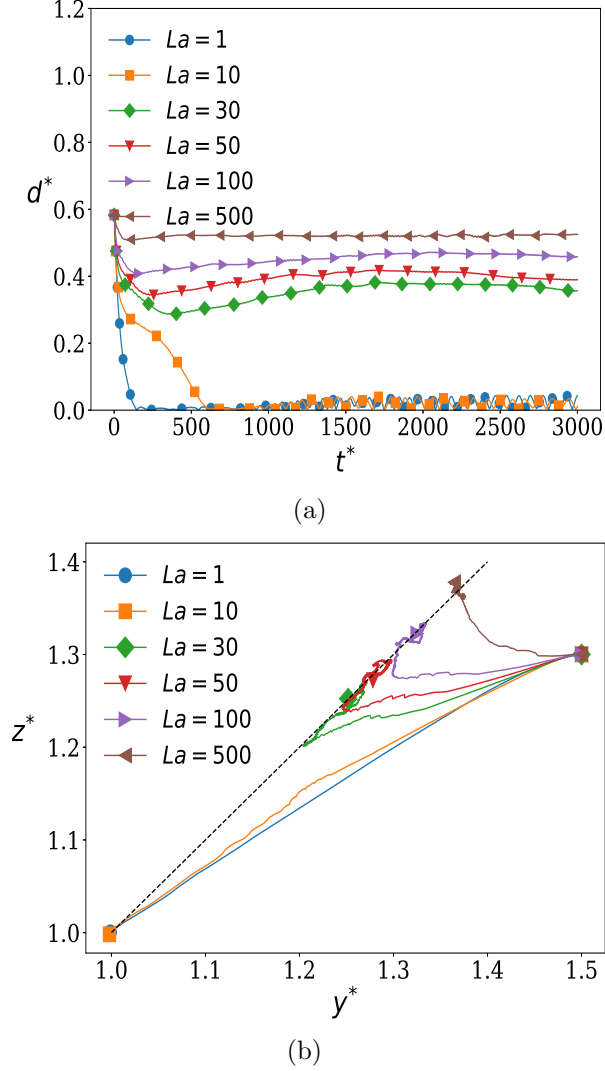


Fig. 3.2. (a) The distance of cells from the channel centerline and (b) the trajectories of cells. The blockage ratio is $\frac{a}{W}=0.3$ and $Re = 37.8$.

the rest of particles lies on the diagonal as shown in Fig. 3.5(a). The reason for this phenomenon is the dependence of the inertial lift force and deformability-induced lift force on the Laplace number. For low La , the deformability-induced force dominates the inertial force and the cells tend to focus on the centerline. As Laplace number increases, the strength of the inertial force increases, while that of deformability-induced force reduces and the inertial force becomes the dominant driving force.

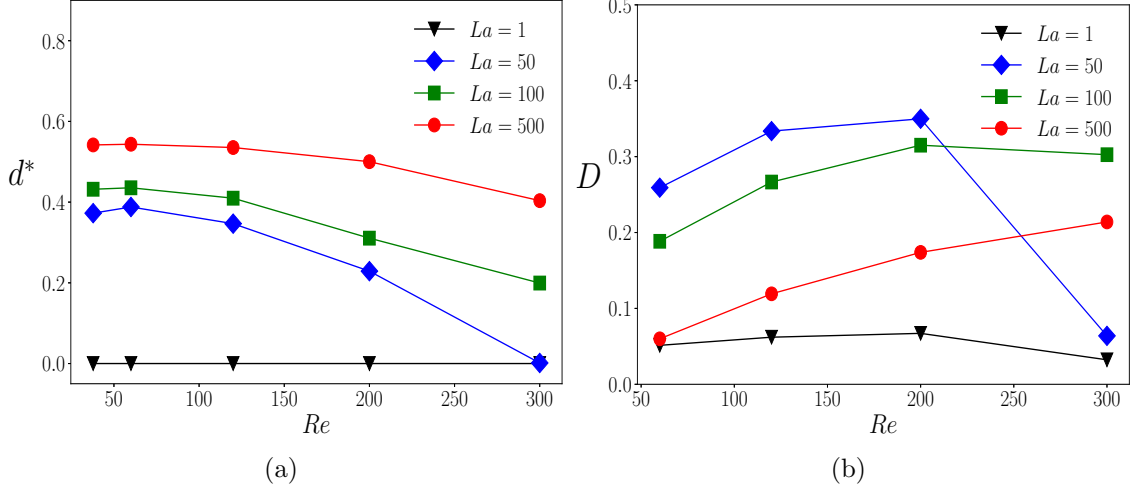


Fig. 3.3. (a) The distance of cells from the channel centerline for various Re and La . (b) Cell deformation for various Re and La . The blockage ratio is $\frac{a}{W}=0.3$.

Under this condition, the final position is pushed further away from the centerline and closer to the that of solid particles which is in agreement with previous studies [51,54].

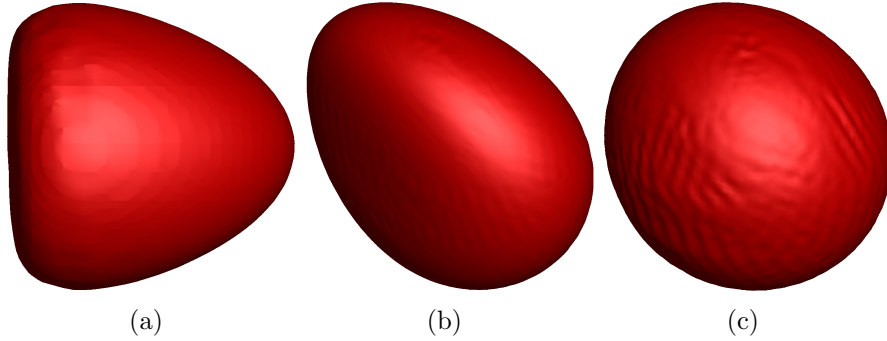


Fig. 3.4. Deformed shape of capsules with $\frac{a}{W} = 0.3$ and $Re = 60$ and (a) $La = 1$ (b) $La = 50$ (c) $La = 500$.

We have also investigated the effect of Re number on the dynamics of deformable capsules. Previous numerical simulations [51,54] studied this effect for the range of $1 < Re < 100$, while in this work we extended this range to $37.4 < Re < 300$. Our

results show that the equilibrium position of rigid particles is almost independent of Re in the range of $1 < Re < 100$ and merely depends on La , which is in agreement with previous observations. However, the equilibrium position of capsules is a function of Reynolds number for larger values of Reynolds number. This dependency is more significant for softer capsules. As shown in Fig.4.3 (a), the deformable capsules move toward the channel center as Re increases and this dependency is enhanced with increasing deformability. This behavior is also observed in Ref. [51], where they showed the change in the focal position of capsules for large Reynolds numbers ($Re = 100$). We should note that the capsule with $La = 500$ is not completely rigid as shown in Fig. 4.3 (b), where the capsule deformation is plotted.

We calculate the Taylor deformation parameter (D) to quantify the deformation of capsules. For this purpose, we compute the moment-of-inertia tensor, which provides us with the principal major and minor axes of an equivalent ellipsoidal particle (L and B , respectively). Accordingly, the deformation parameter is defined as:

$$D = \frac{L - B}{L + B} \quad (3.11)$$

Figure 4.3 (b) illustrates the deformation parameter versus Re for different La . The increase in Laplace number leads to decrease in the deformation, except for $La = 1$ which is very soft and has a small deformation. The reason for this phenomenon is related to the equilibrium position of these particles. The focal position for capsules with $La = 1$ is the channel centerline where the shear rate is zero and the capsule has a parachute shape that yields to a small deformation. Furthermore, increasing Re leads to an increase in the deformation because of the increase in the viscous shear stress acting on the deformable capsules. Interestingly, for $La = 50$ the deformation rapidly falls at $Re = 300$. The final position of the capsule at this Reynolds number

is at the centerline. This capsule has a parachute shape and experiences a small shear rate.

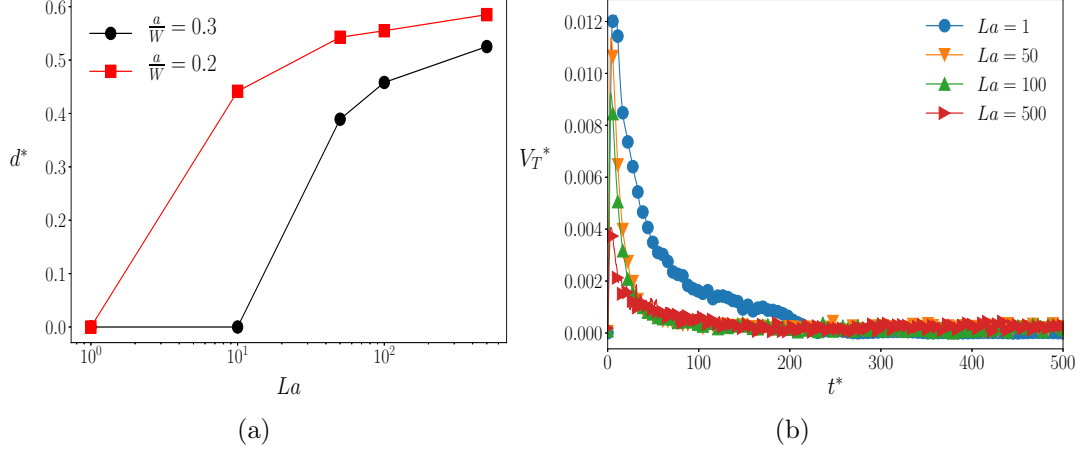


Fig. 3.5. (a) Equilibrium position of cells for various deformability and size at $Re = 37.8$. (b) Temporal evolution of cross-streamline velocity of cells with $\frac{a}{W} = 0.3$ and $Re = 60$.

Figure 4.4 shows the deformed shape of capsules at their focal position. According to Fig.4.3 (a) soft capsules (e.g., $La = 1$) focus at the centerline and experience a symmetric deformation, leading to a parachute shape. As the Laplace number increases the final equilibrium position moves away from the centerline and capsules asymmetrically deform. Increasing the Laplace number means that the capsule behaves more similar to a rigid particle. On the other hand, the final position of capsules with larger La is closer to the wall which yields larger viscous stress exerted on the capsule. Therefore, the deformation of capsule does not monotonically decrease with La .

The inertial force scales with $Re(\frac{a^3}{W^3})$ according to Ref. [54]. Therefore, the cell size is another important factor that changes the motion of cells. According to the Fig. 3.5(a), the critical La_c number at which the cell equilibrium position is away from the centerline is affected by the size such that the larger cells require larger La

number to not focus on the center. This value is also sensitive to Re number [54]. The cell size also affects the off-center equilibrium position of the cells illustrated in Fig. 3.5(a). Smaller cells end up at the location more distant from the center for a given La number. This is due to the fact that d_{eq} (the equilibrium distance from the centerline) is proportional to $\frac{La}{(\frac{a}{W})^4}$ according to Ref. [54]. Figure 3.5(b) illustrates the temporal evolution of the cross-streamline velocity V_T^* and the role of the cell deformability. The migration velocity of softer cells is larger, although all cells are released from the same location in the microchannel. The cells reach their focal position nearly at the same time. Hence, those cells that need to travel longer distance to reach the equilibrium position have a larger velocity.

3.3.2 Cell focusing in an Oldroyd-B fluid

In this section, we study the effect of fluid elasticity on the cell migration behavior. Our numerical results suggest that an Oldroyd-B viscoelastic fluid drives the cells toward the channel centerline. Figure 3.6(a) shows the final position of cells for different Laplace and Weissenberg numbers for $\frac{a}{W}=0.3$ and $Re=37.8$. The equilibrium position of the cells is on the diagonal similar to a Newtonian fluid. The equilibrium position of the cells is shifted closer to the center with increasing Wi number ($Wi=0$ represents the Newtonian fluid). Ultimately, for $Wi=2$ all the cells regardless of their size and deformability focus at the centerline. It should be noted that for $La=1$ and 10 the cells end up on the centerline even for a Newtonian fluid due to the strong deformability-induced force. Hence, increasing the Wi number does not make any change to the final position of these soft cells. The observed focusing behavior provides us with the ability to control the focal position of cells by tuning Wi number. The cell migration is influenced by viscoelastic, inertial and deformability-induced forces. The viscoelastic and deformability effects have reinforcing interaction in driv-

ing the cells to the center, while the inertial force has an opposite effect. Therefore, for low Wi numbers when the elasticity is weak, the cells are significantly influenced by the inertial force and focus to an equilibrium location close to the one in a Newtonian fluid. As the Weissenberg number and consequently fluid elasticity increase, the final position of cells moves toward the centerline. Figure 3.6(b) shows the trajectories of cells for $La = 500$, $\frac{a}{W} = 0.3$ and $Re = 37.8$ at various Wi numbers. Cells migrate to the diagonal of the microchannel and the final position represented by symbols approaches the centerline as the fluid elasticity increases. Finally, at $Wi = 2$ the cell directly moves towards the centerline indicating the dominance of the viscoelastic stress on the cell migration. Figure 3.7(a) shows the flow field in the cross-section of the microchannel where the cell is located at $Re = 37.8$ and $La = 500$. The streamlines around the cell in an Oldroyd-B fluid are directed radially inward, leading to cell focusing on the centerline.

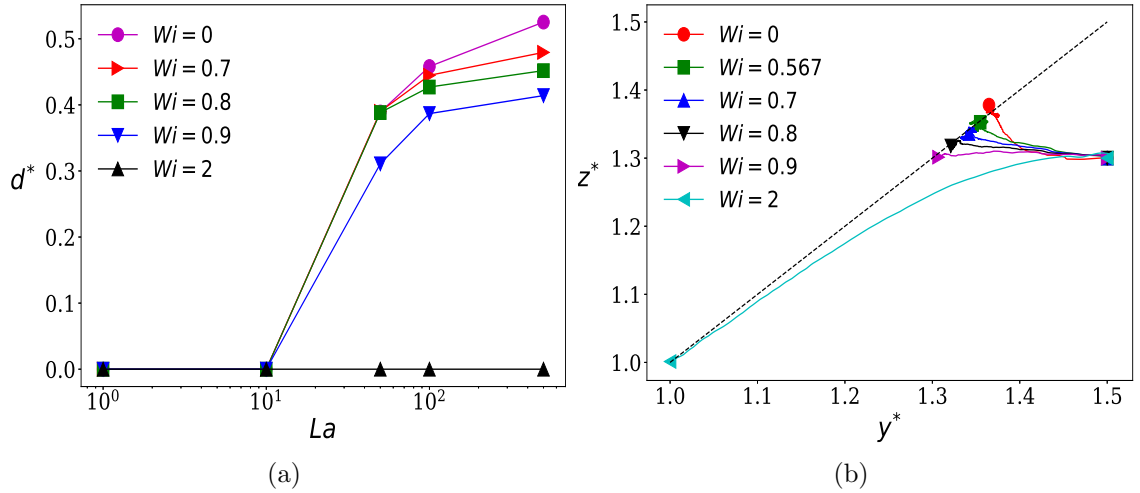


Fig. 3.6. (a) Focal position and (b) trajectories of cells with $\frac{a}{W} = 0.3$ and $Re = 37.8$ in an Oldroyd-B fluid.

Another important effect that influences the dynamics of the cells is the inertial effect. Figure 3.8 illustrates the impact of the Re number on the final position of the

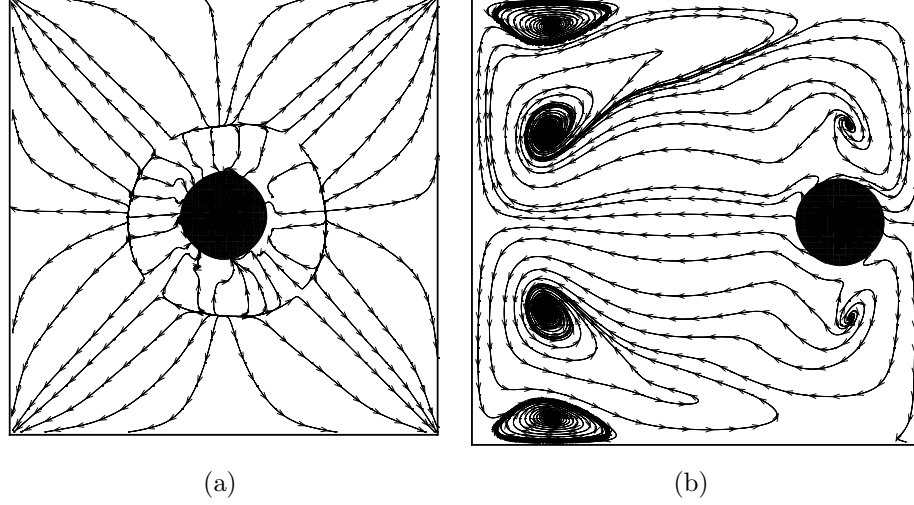


Fig. 3.7. The flow field around the cell in (a) an Oldroyd-B fluid ($Wi = 2$) and (b) a Giesekus fluid ($Wi = 2$ and $\alpha = 0.1$). The blockage ratio is $\frac{a}{W} = 0.2$ and $Re = 37.8$.

cells at $Wi = 2$ and $Wi = 5$ for the cells with $La = 50$ and $\frac{a}{W} = 0.3$. Increasing the Re number induces disturbances in the flow field such that at a large enough Reynolds number the flow regime transitions from laminar to turbulence and cell focusing no longer occurs [57]. This is the main limitation of current microfluidic technologies leading to low throughput devices for cell classification. Hence, it is important to study the inertial effects in the presence of polymers and identify the threshold above which cell focusing is not observed. Figure 3.8 shows the interplay between the flow inertia and the elastic effects that determines the final position of the cell. The equilibrium position of cells moves further toward the channel wall with increasing Re . The reason for this behavior is the dependence of the inertial lift force on the Reynolds number. The inertial lift force is correlated with the Reynolds number as $F_{inertail} \sim Re^2$ according to Ref. [54]. In high Re number regimes, the inertial lift force dominates other effects, while in low Re number regimes, the viscoelastic effect is stronger and the cells focus on the centerline. On the other hand, the effect of

fluid viscoelasticity is significant even at high Re numbers such that cell focusing occurs in the presence of polymers. However, the focal position is no longer at the centerline. As shown in the Fig. 3.8 the final position of the capsule in polymeric fluid is significantly affected by the Re number. This phenomenon is also observed for solid particle migration in viscoelastic fluids [58]. The inertial lift force acting on a solid particle [43] is in the form of:

$$F_{inertial} = \rho U_0^2 a^2 \left(\frac{a}{W}\right)^2 C_2 \left(\frac{y}{W}\right) \quad (3.12)$$

where y denotes the distance from the centerline. Furthermore, the viscoelastic force on a solid particle in a second order fluid [77] is:

$$F_{viscoelastic} = -\frac{40}{3} \pi \rho U_0^2 (2a)^2 \left(\frac{a}{W}\right) \left(\frac{Wi}{Re}\right) \beta \left(\frac{y}{W}\right) \quad (3.13)$$

The negative sign in eq. 3.13 shows that this force is toward the centerline, leading to the cell migration toward the centerline in an Oldroyd-B fluid. The balance between these two forces determines the equilibrium position of a solid particle. Equations 3.12 and 3.13 indicate that the location where the sum of forces are zero strongly depends on the Reynolds number.

The results indicate that we still have a control on the equilibrium position of cells in high Reynolds number regimes when the fluid is viscoelastic. We note that a higher Reynolds number corresponds to a larger sample volume flow rate. The addition of polymers improves the throughput of microfluidic cell focusing devices.

The fluid elasticity brings the equilibrium position of cells closer to the centerline. For instance, at $Re = 100$ the cell is no longer at the channel center for $Wi = 2$ and increasing the Re number leads to a larger equilibrium distance from the centerline. Increasing the Wi number, on the other hand, decreases the equilibrium distance

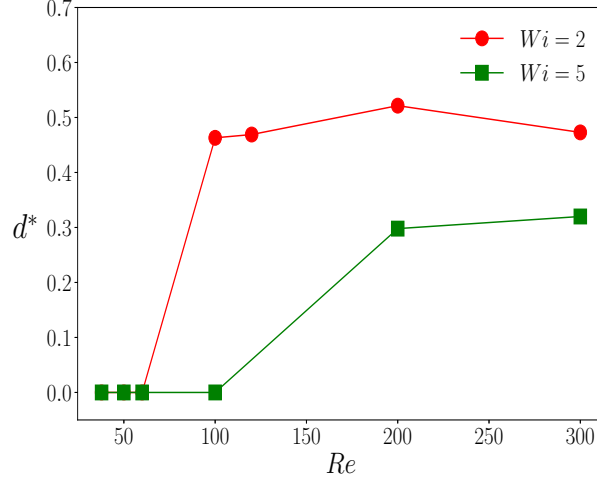


Fig. 3.8. Focal position of the cells in an Oldroyd-B fluid. Here, $\frac{a}{W} = 0.3$ and $La = 50$.

from the centerline. By changing the Weissenberg number from 2 to 5, the centerline focusing occurs even for $Re = 100$. This phenomenon suggests that for each Wi number there is a critical Re_c number above which the final position of the cells is no longer on the centerline. In order to achieve the centerline focusing of the cells for higher Re numbers, it is required to increase the Wi number of the fluid. This change is experimentally possible by increasing polymer molecular weight or concentration, but the resulting numerical instability limits the range of the Weissenberg number that can be explored in this paper. These results suggest that this method can be used for cleaning the particulate flows. Cells in an Oldroyd-B fluid (constant-viscosity polymeric fluid) assemble in the channel center and can be separated from the suspending fluid. For instance, bacteria or circulating tumor cells (CTC) can be separated from the suspending fluid [21]. Furthermore, this method does not employ any complex active system for controlling the migration such as electric or magnetic field or acoustic wave application, which limit the sample throughput and often requires skilled users.

Another important advantage of using fluid elasticity is the ability of the polymer chains in maintaining the flow regime in a laminar regime even for very high Re numbers. It means that higher sample throughput can be pumped into the microchannel without transition into a turbulent regime, and the focusing behavior is still observed for high flow rates. We note that the previous studies on particle focusing were restricted to rigid particles in a Newtonian fluid or highly viscoelastic fluid ($Wi \gg Re$) in the creeping flow limit [78–82]. In these studies, the deterioration of particle focusing was observed for $Re > 1$. Lim *et al.* [57] showed that the focusing behavior of rigid particles can be achieved for high Reynolds numbers ($10 < Re < 10^4$) and weakly viscoelastic fluids ($Wi \ll Re$). Here, we quantify for the first time focusing of deformable cells in viscoelastic polymeric fluids.

3.3.3 Cell focusing in a Giesekus fluid

In this section, the effects of the fluid elasticity and shear-thinning behavior on the cell migration is investigated by using a Giesekus constitutive equation. Figure 3.9(a) shows the final position of the cells with varying deformability for $\frac{a}{W} = 0.3$ and $Re = 37.8$. The cells in a shear-thinning viscoelastic fluid are pushed toward the wall compared to their final position in a Newtonian fluid. This behavior is opposite of what we observed in an Oldroyd-B fluid. The reason for this complex behavior can be explained by considering the interplay between effective forces on the cell. In this fluid, the dynamics of the cells is governed by the interplay between shear-thinning effects, secondary flow generated by second normal stress difference (nonzero for a Giesekus fluid and zero for an Oldroyd fluid), elastic force, inertial effect and the deformability-induced force. Mobility factor α that is non-zero in a Giesekus fluid leads to a shear-thinning effect which is absent in an Oldroyd-B fluid. The shear-thinning effect significantly reduces the viscoelastic force (the force that drives the cell

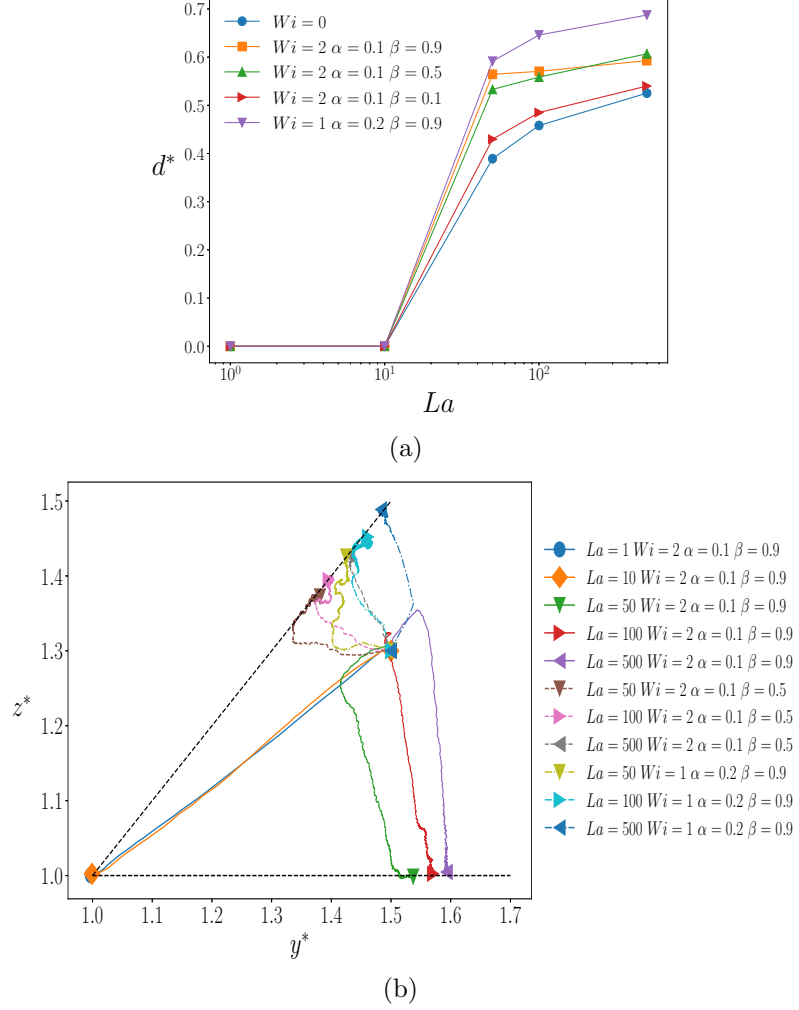


Fig. 3.9. (a) Final equilibrium location of cells and (b) their corresponding trajectories in a Giesekus fluid. The blockage ratio is $\frac{a}{W} = 0.3$ and $Re = 37.8$.

to the centerline) by reducing the viscosity. It also increases the flow velocity (Fig. 3.11(b)) which enhances the inertial force (the force that pushes the cells toward the wall). Furthermore, the secondary flow induced by the second normal stress difference [58] shown in Fig. 3.7(b) moves the final position of cells closer to the channel walls. The deformability-induced force for the cells with low La number ($La = 1$ and $La = 10$) dominates other effects, and similar to the Newtonian fluid the cells move

to the centerline. On the other hand, increasing the Laplace number leads to the cell migration to off-center locations. The difference between the equilibrium position of soft and rigid cells becomes larger in an Giesekus fluid and this effect enhances the separation of cells based on cell deformability. The stress tensor generated in the presence of the polymeric fluid depends on parameters such as α and β (see equation (5.7)). Therefore, it is important to study the effect of these parameters on the cell migration to provide engineers with an insight to design more efficient sorting techniques. According to Fig. 3.9(a), as β increases from 0.1 to 0.9 for constant Wi and α , the focal position of cells is pushed toward the wall, while the distance between the equilibrium position of the cells with different La number is significantly reduced. This behavior continues with increasing β until the cells with Laplace numbers ranging from 50 to 500 assemble in the same location at $\beta = 0.9$. In this case, all cells focus onto the same off-center point in the cross section regardless of their deformability. Figure 3.9(b) shows the trajectories of cells toward the equilibrium position in a Giesekus fluid $Re = 37.8$. The final location of the cells are mostly on the channel diagonal similar to the Newtonian and Oldroyd-B fluids except for the case with $Wi = 2$, $\beta = 0.9$ and $\alpha = 0.1$, where the equilibrium position is on the x-axis. Previous studies [83] have shown that the stability of final position changes with Re and size ratio ($\frac{a}{W}$), while here we show that the stability can also change with the variation of fluid rheology such as β given a constant Reynolds number and size ratio. Mobility factor α is another parameter that plays an important role in the cell dynamics. Increasing α from 0.1 to 0.2 leads to an increase in the final distance of the cells from centerline. The reason for this observation can be attributed to the stronger secondary flow, generated in a Giesekus fluid, that pushes the cells toward the wall. This phenomenon has been observed in previous works [58]. Additionally, the shear-thinning effects increase the inertial lift force. This effect pushes the cells

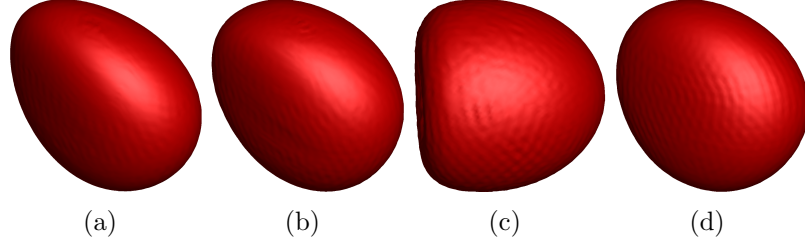


Fig. 3.10. Deformed shape of capsules with $\frac{a}{W} = 0.3$, $La = 50$, $Re = 60$ and (a) $Wi = 0$ (b) $Wi = 0.9$ and $\alpha = 0$ (c) $Wi = 2$ and $\alpha = 0$ (d) $Wi = 1$ and $\alpha = 0.2$

toward the channel wall. The results presented in this section suggest that the efficiency of microfluidic technologies used for classification of soft and stiff cells increases in shear-thinning polymeric fluids. In this section, we also investigate the effect of fluid elasticity on the shape and deformation of cells. Figure 3.10 illustrates the deformed shape of capsules at their equilibrium position for various polymeric fluids at $Re = 60$ and $La = 50$. The shape of the cell in a polymeric fluid is smoother and it does not develop sharp edges compared to the cell in a Newtonian fluid. In order to quantify the effect of viscoelasticity, the Taylor deformation parameter is plotted for polymeric fluids in Fig. 3.11 (a). According to this figure the capsule deformation decreases with increasing Wi number in an Oldroyd-B fluid. As we mentioned in section 3.3.2, the cells move toward the centerline as the Weissenberg number increases in an Oldroyd-B fluid. Therefore, the cells experience less viscous shear stress leading to smaller deformations. Furthermore, as we shown in our previous work [61], the capsule deformation decreases with increasing Wi number due to the developed normal stress around the capsule membrane. The capsule at $Wi = 2$ focuses at the centerline (Fig. 3.10(c)) and it recovers the parachute shape. On the other hand in Gseikus fluid, the cells move toward the channel wall, leading to larger viscous shear stresses and consequently larger deformations.

Figure 3.11(b) shows the streamwise velocity profile at $Z^* = 1$ and $X^* = x_{center}^*$, where x_{center} represents the x-component of the capsule center of mass. In this case, $Re = 60$ and $La = 1$ leading to focusing of the capsule on the center in both Newtonian or polymeric fluids. According to this figure, the velocity profiles for Newtonian and Oldroyd-B fluids are identical, while the velocity increases for a Giesekus fluid, due to the shear-thinning effect [58]. This phenomenon suggests that the use of Giesekus fluid in micro-devices increases the volumetric flow rate of samples. The uniform velocity occurs inside the deformable capsules (channel centerline). The translational velocity of the cells is smaller than the flow velocity at that location, meaning the cell lags the flow. The similar behavior is observed for rigid particles [58]. This behavior is attributed to the dominant effect of the wall that increases the drag force acting on capsules [84, 85].

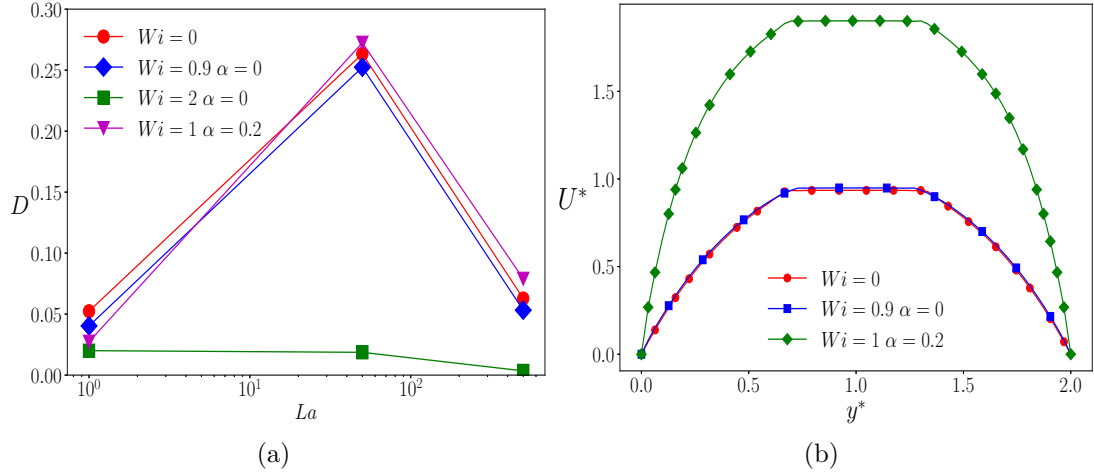


Fig. 3.11. (a) Deformation parameter of capsules at $Re = 60$ and (b) the velocity profile at $Z^* = 1$ and $X^* = x_{center}^*$ with $Re = 60$ and $La = 1$

3.4 Conclusions

In this paper, we studied the dynamics of deformable cells in Newtonian and polymeric fluids flowing in a square microchannel. We investigated the effects of various parameters such as cell deformability, fluid elasticity, inertia and size on the cell migration behavior. The numerical results show that the equilibrium position of deformable cells are different from the rigid particles. Previous studies [76, 86] showed that the focal position of rigid particles are four off-center points near the channel wall, while our results show that of deformable cells lies on the channel diagonal. The deformability has a significant role on the dynamics of cell migration such that the reduction in the Laplace number causes the final position of cells to approach the channel centerline. This behavior is attributed to the strength of deformability-induced force that increases with decrease in La moving the cells to the center. This effect becomes dominant for very soft cells (e.g., $La = 1$), where cells focus on the centerline regardless of their size. The migration of cells in a Newtonian fluid is a function of size, deformability and flow inertia. We observed a completely different behavior for the cases in which the cells flow in a polymeric fluid. The constant-viscosity viscoelastic fluid (an Oldroyd-B fluid) pushes the cells toward the centerline. The focal position of the cells approaches the centerline with increasing Wi and ultimately all the cells with various size and deformability end up at the centerline. The results suggest an enhanced focusing behavior in a polymeric fluid that can be used in various applications aiming to separate the cells from the suspending fluid. We also investigate the effect of fluid inertia and showed that increasing the Reynolds number, pushes the equilibrium position toward the wall which exhibits an opposite effect compared to the Weissenberg number. The stabilizing effect of the polymer molecules in the suspending fluid enhances the throughput of current microfluidic technologies as it delays the transition from laminar to turbulent flow. This allows us to increase the

sample flow rate while achieving cell focusing. The cell motion in a shear-thinning viscoelastic fluid (a Giesekus fluid) is considered in this paper. Our findings indicate that non-Newtonian effects of a Giesekus fluid drives the cells toward the wall, contrary to an Oldroyd-B fluid. The reason for this behavior can be attributed to shear-thinning effects and the secondary flow generated in a microchannel. The findings of this paper suggest that the addition of polymers in microfluidic devices can be used to enhance the throughput of cell focusing and separation at a very low cost. This study provides an insight on the role of rheological properties of the fluid and ways they can be tuned to control the focal position of the cells.

3.5 Appendix

3.5.1 Mesh independency

In this section, we show the mesh-independency of the results presented in this study. As we mentioned in section 3.2.2 the computational domain for $Re = 37.8$ is discretized using $128 \times 76 \times 76$ in x , y and z directions, respectively. In order to check the mesh-independency of the numerical simulations, we used $128 \times 152 \times 152$ Eulerian mesh. The results are shown in Fig. 4.17 for $La = 500$. The focal positions changes 1.5% as we increase the number of grid points.

The mesh-independency of the numerical simulation is also checked for $Re = 200$ and $La = 50$. Fig.3.13(a) and (b) show the distance of the capsule from the channel centerline for Newtonian ($Wi = 0$) and Oldroyd-B ($Wi = 2$) fluids, respectively. The maximum error between two different sets of grid points are 2.02% and 0.65% for Newtonian and Oldroyd-B fluids, respectively.

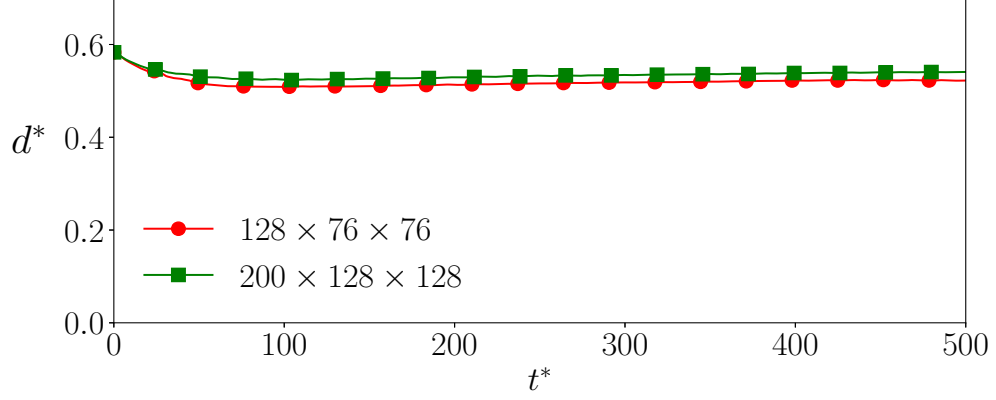


Fig. 3.12. Distance of the capsule from the channel centerline for $La = 500$ and $Re = 37.8$ with $128 \times 76 \times 76$ and $200 \times 128 \times 128$ Eulerian grid points.

3.5.2 Domain independency

Here, we show the independency of the numerical results to the domain length in the X-direction, where the periodic boundary condition is applied. Figure 3.14 shows the distance of capsule from the channel centerline at $Re = 100$ and $La = 500$ for two cases with different lengths in X-direction ($L = 4W$ and $L = 8W$). The maximum error between two different cases is 1.71%.

3.5.3 Validation of viscoelastic model

The viscoelastic model used in this study is validated against published results. For this purpose, we simulate the deformation of a droplet containing polymeric fluid subjected to a shear flow. Figure 3.15 shows the ratio of steady-state deformation to the deformation of a droplet with Newtonian content at $Ca = 0.2$ ($Ca = \frac{\mu a \gamma}{\sigma}$, where a and σ are the droplet radius and surface tension, respectively, and γ denotes the imposed shear rate). The results are in a good agreement with previous published results [67], with maximum error of 0.72%.

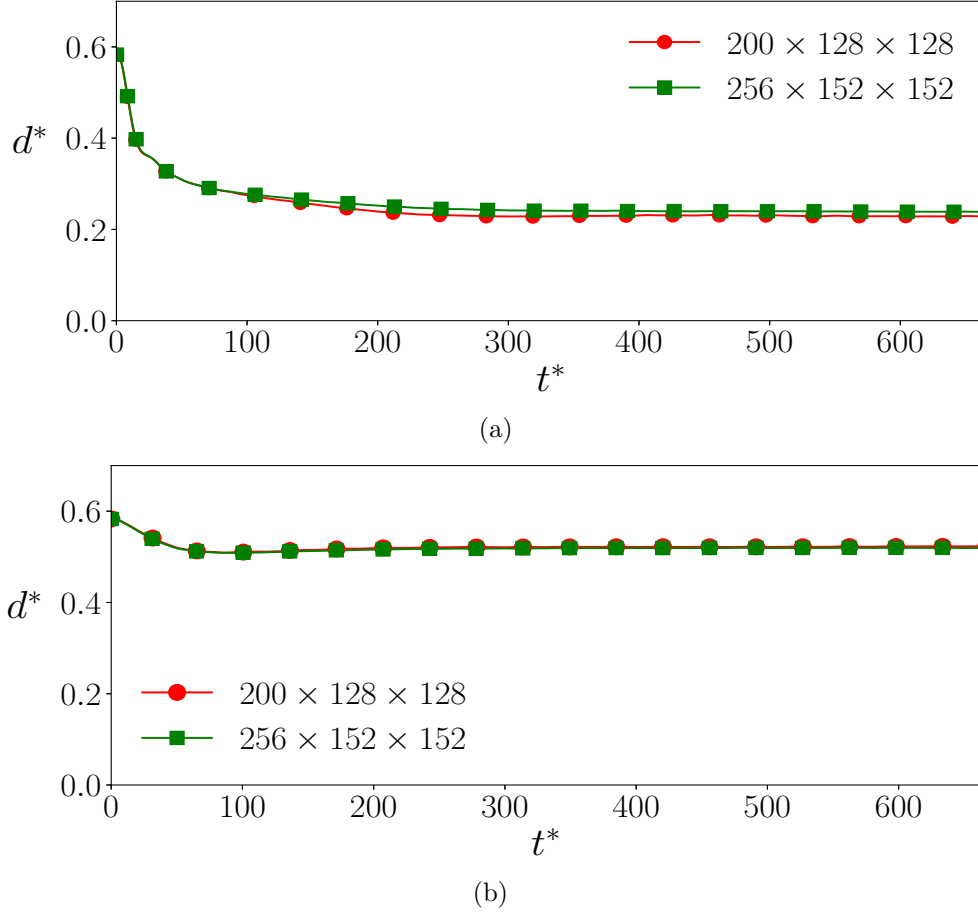


Fig. 3.13. Distance of the capsule from the channel centerline at $Re = 200$ and $La = 50$ for a) $Wi = 0$ and b) $Wi = 2$ with $200 \times 128 \times 128$ and $256 \times 152 \times 152$ Eulerian grid points.

3.5.4 Validation of numerical method

Here, we compare the results of our study with published results [54] to show that the numerical method used in this investigation accurately captures the inertial effects. For this purpose, the equilibrium position of capsules of various La flowing in a microchannel filled with a Newtonian fluid is computed. The Reynolds number in our study is $Re = 37.8$. As we know, the Reynolds number does not affect the equilibrium position of capsule in this range [51]. Our results are in good agreement with Ref [54] and the maximum error observed here is 1.15% (Fig.3.16).

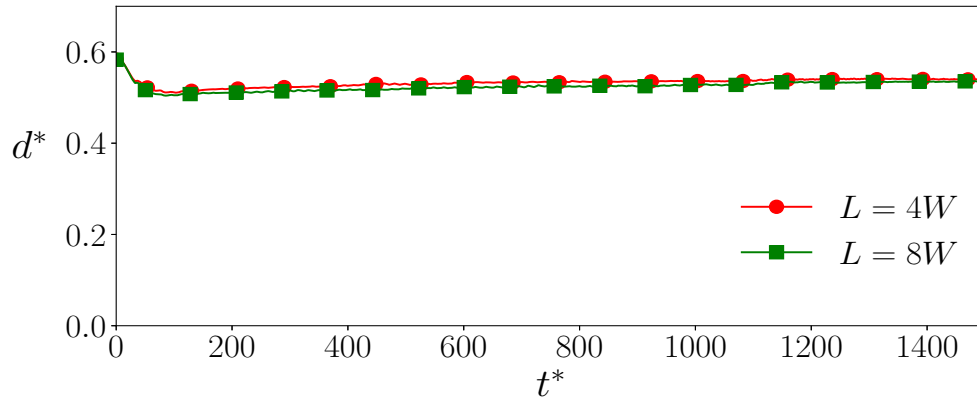


Fig. 3.14. Distance of the capsule from the channel centerline at $Re = 100$ and $La = 500$ for different domain lengths $L = 4W$ and $L = 8W$.

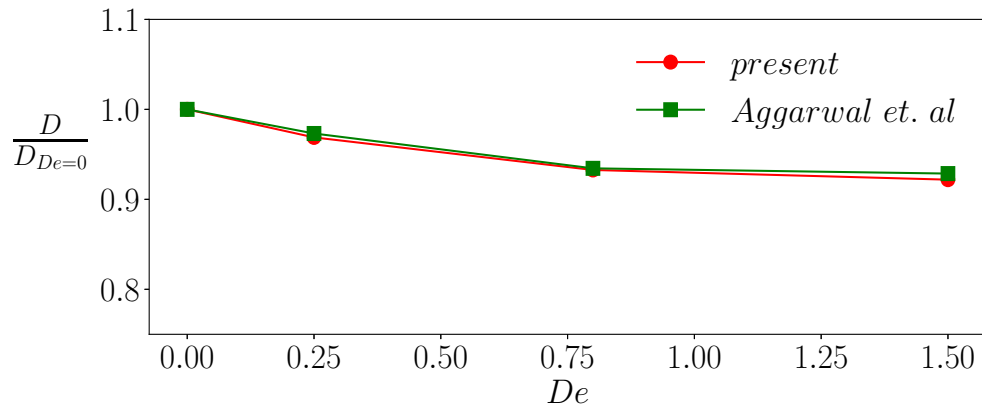


Fig. 3.15. Deformation of polymeric droplet at $Ca = 0.2$ and various Deborah numbers.

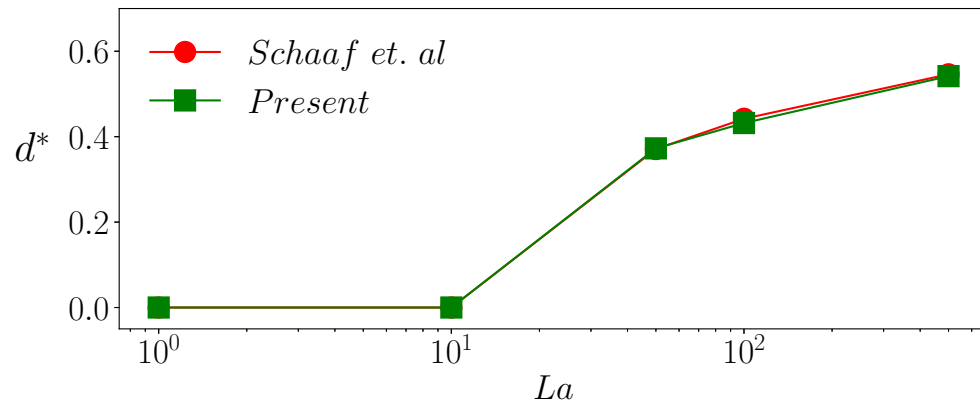


Fig. 3.16. Equilibrium position of a deformable capsule flowing in a microchannel filled with a Newtonian fluid.

4. SUSPENSION OF DEFORMABLE PARTICLES IN NEWTONIAN AND VISCOELASTIC FLUIDS IN A MICROCHANNEL

This chapter is reproduced with permission from: A.H. Raffiee, S. Dabiri, A.M. Ardekani, Suspension of deformable particles in Newtonian and viscoelastic fluids in a microchannel”, Microfluidics and Nanofluidics, 23(2), 22. [87]

4.1 Summary

In this chapter, we study a suspension of cells flowing in a microchannel of Newtonian and viscoelastic fluids and investigate the role of cell size, cell volume fraction, inertia, deformability and fluid elasticity on the cell distribution. Our results suggest that the use of constant-viscosity viscoelastic fluid pushes the cells toward the channel centerline which can be used in microfluidic devices used for cell focusing such as cytometers. Furthermore, we show that the volumetric flow rate can be significantly enhanced with the addition of the polymer in the suspending fluid. This fundamental study can provide insight on the role of rheological properties of the fluid and other factors that they can be tuned to control the collective behavior of the cells that can be used for efficient design of microfluidic devices.

4.2 Introduction

The motion of synthetic capsules and living cells in microchannels has been the subject of numerous studies in the last decade due to its significance in engineering and biomedical applications [88, 89]. Cell sorting and separation are common pro-

cesses that are used for various purposes such as separation of leukocytes from blood used in DNA sequencing [21]. Early diagnosis of lethal diseases such as cancer [25] can be conducted by isolation of rare cells in blood, which is a complex suspension of the cells. Furthermore, fractionated healthy blood components are used for different therapeutic applications such as platelet transfusion [28]. Cell isolation and enrichment provide a better platform to biologists to study and analyze various properties of living cells [21, 29]. In this regard, microfluidic devices provide a platform to achieve aforementioned needs while overcoming challenges such as sample contamination, cost and complexity of the procedures [90]. Besides, these devices offer higher accuracy for analysis and increased automation of the process [91, 92]. Accordingly, there is a high demand for developing techniques to precisely control trajectories of the cells and manipulate them in a desired manner. Some of the proposed techniques employ external factors such as electric [93], magnetic [94] and acoustic [95] fields and sheath flows [96–98]. Even though, they can offer high throughput sample processing, the complexity of the procedure and high cost limit their utilization in clinical applications [21]. Furthermore, these methods require cell manipulation that may change biological properties of the cells [99]. Hence, there is a growing interest in employing label-free techniques that take advantage of physical properties of the cells such as size, shape and deformability to control their trajectories in microfluidic devices [21, 90, 99]. Inertial microfluidics are among the proposed techniques that use inertial forces to induce cell migration in microchannels [76, 86, 100]. In this technique, cells focus at an equilibrium position depending on their physical properties [39, 101, 102]. The particles flowing in a Newtonian fluid follow the streamlines without any transversal migration for low Reynolds numbers [43]. With increasing the Reynolds number the inertial force becomes important and the cross-streamline migration of particles is observed [79, 103]. Previous investigations show that the

deformability of the cell can affect its trajectory in the microchannel [54, 71]. Due to deformability of cell membrane, a deformability-induced force is generated and the interplay of all the above forces governs the equilibrium position of the flowing cells [71]. In chapter 3, we study the effect of cell deformability on the equilibrium position of the deformable cells. Our results show that deformability-induced force drives the cells toward the channel centerline in a Newtonian fluid. Recent studies on microfluidic devices introduced an alternative way for cell focusing by adding a polymer to the suspending fluid [104–106]. In this method, the polymer chains in the fluid are stretched and generate an uneven normal stress on the flowing particles. This phenomenon leads to a net elastic force that interacts with the inertial force and affects the migration dynamics and equilibrium position of the particle [60, 99]. This phenomenon has been experimentally and analytically [78, 79, 81] observed. The particle migration depends on the fluid rheology, cell size, channel geometry and volumetric flow rate [107]. There are several experimental studies that showed promising results for cell separation and focusing using polymeric fluid as the suspending fluid. For instance, human breast carcinoma and leukocyte cells were separated in a straight microchannel [108] which highlights the effect of cell size and deformability on the particle migration flowing in a viscoelastic polymeric fluid. The effect of size and deformability was also observed in *Liu et al.* [109] where solid particles, living cells and bacteria were separated by focusing in different locations in the channel cross-section. Previous studies [71, 79, 110, 111] show that fluid rheological properties are important on the dynamics of cell migration in microchannels. In chapter 3, we show that a constant-viscosity viscoelastic fluid drives the particle toward the channel centerline, while a shear-thinning viscoelastic fluid exhibits an opposite behavior. The equilibrium position of the cell depends on the cell size, deformability and volumetric flow rate.

Despite the importance of the dynamics of cell suspension in a microchannel, previous experimental and computational studies focus on the migration of cells in a very dilute regime. In this chapter, we focus on the suspension of deformable cells in Newtonian and polymeric fluids in a semidilute regime and investigate the role of various factors including cell size, deformability, inertia and viscoelasticity of the suspending fluid. Our results provide fundamental understanding of the dynamics of suspension of cells in a straight microchannel used in various microfluidic devices.

4.3 Methodology

4.3.1 Problem setup

In this work, the computational domain is a straight squared channel illustrated in Fig. 4.1. The edge of the channel is $2W$ and the channel length is set to be $4W$. We applied a periodic boundary condition in x direction and a no-slip boundary condition is implemented in y and z directions. In this problem, W and U_0 (the centerline velocity of the channel) are used as the characteristic length and velocity scales, respectively. Hence, the dimensionless numbers governing the problem are: (i) the Reynolds number $Re = \frac{\rho U_0 2W}{\mu}$ that represents the ratio of inertial to the viscous forces, (ii) the Laplace number $La = \frac{2\rho E_s a}{\mu^2}$ denoting the deformability of the cell, (iii) ϕ that shows the volume fraction of cells in the microchannel, (iv) the Weissenberg number $Wi = \frac{\lambda U_0}{W}$ showing the ratio of elastic to viscous forces and (v) $\beta = \frac{\mu_p}{\mu}$ representing the ratio of the polymer viscosity to total viscosity ($\mu = \mu_s + \mu_p$) and finally (vi) the aspect ratio $AR = \frac{a}{W}$ that shows the blockage ratio in the microchannel. We assume that the inner fluid of the cells is a Newtonian fluid with a density and viscosity equal to those of the outer fluid ($(\mu_s + \mu_p)_{outer} = (\mu_s)_{inner}$ and $\rho_{inner} = \rho_{outer}$). Unless otherwise stated, β is set to 0.9 and the cells are initially spherical. The computational

domain and cell membrane are discretized using $128 \times 76 \times 76$ Eulerian grid points in x , y and z directions and 20000 Lagrangian grid points. The mesh and domain size independency tests are provided in the Appendix.

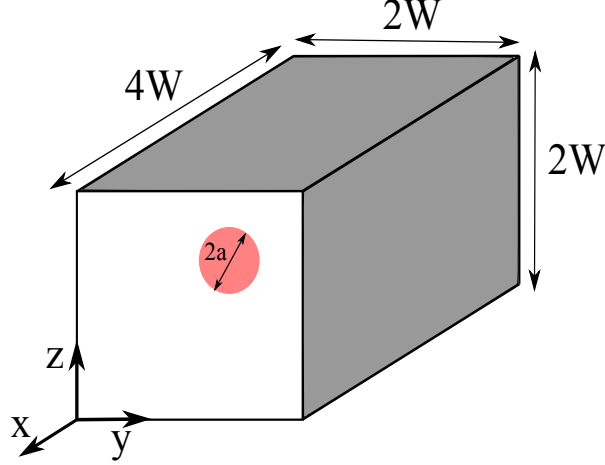


Fig. 4.1. Schematic of problem setup

4.4 Result and discussion

4.4.1 Newtonian fluid

In this section, the migration of cells flowing in a Newtonian fluid is investigated. The effects of various factors including deformability (La), cell volume fraction (ϕ), inertia (Re) and cell size ($\frac{a}{W}$) are explored. The computational domain is filled with a suspension of randomly distributed cells (cells with the same size and deformability) along the channel. A constant pressure gradient is applied to generate a flow in the microchannel and cells flow and migrate across the microchannel due to the cell-cell and cell-fluid interactions. The simulation is run long enough that the suspension reach a statistically steady state. The Reynolds number is set to 37.8 unless otherwise stated.

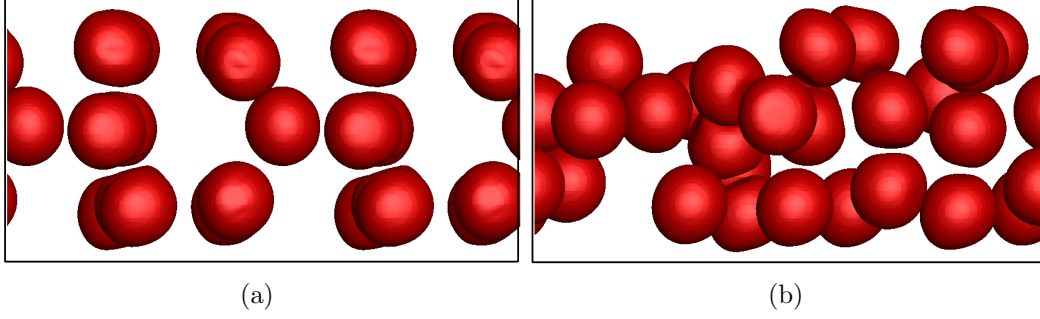


Fig. 4.2. The distribution of cells at (a) $t^* = 0$ and (b) at $t^* = 1800$ for $\phi = 20\%$, $\frac{a}{W} = 0.3$, $La = 500$ and $Re = 37.8$

Figure. 4.2 illustrates the cell suspension at two time instances $t^* = 0$ and $t^* = 1800$ for $La = 500$, $\phi = 20\%$ and $\frac{a}{W} = 0.3$. The cells interact and deform in the channel. Due to the low shear rate in the central region of the channel, cells maintain their initial spherical shape, while cell deformation is more significant as the cells get closer to the wall, where the shear rate is higher. Cells migrate in the cross-stream direction and accumulate near the center of the channel. This migration behavior toward the centerline is caused by the deformability-induced force acting on the cells. The interplay between this force, inertial lift force and wall-induced force determines the focal location of cells [54, 71] in the microchannel. The migration of cells toward the center can also be observed by comparing cell distribution at two different time instances in Fig. 4.2 where the accumulation of cells near the center of channel is significant. To study the motion of a suspension of cells, the ensemble average of cell distance from the centerline ($\langle r^* \rangle$) is computed. Figure. 4.3 shows the temporal evolution of average distance of cells from the channel centerline for various La number at $\phi = 10\%$, $\frac{a}{W} = 0.3$. According to this figure, $\langle r^* \rangle$ initially decreases and reaches a quasi-steady state. The initial decrease in $\langle r^* \rangle$ shows the net migration of cells toward the centerline due to the deformability-induced force acting on the cells. The steady value of cell position is computed by temporally averaging $\langle r^* \rangle$ over

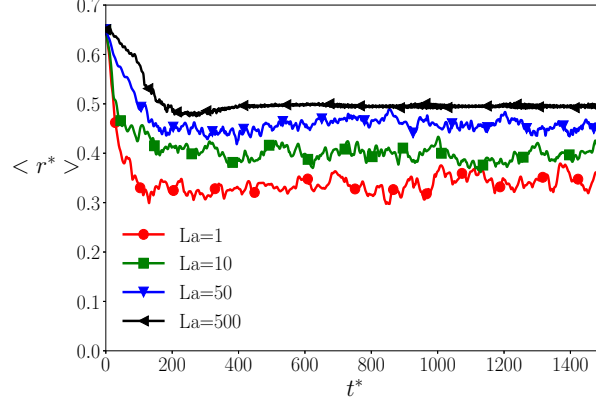


Fig. 4.3. Average cell distance from the centerline for $\phi = 10\%$, $\frac{a}{W} = 0.3$ and $Re = 37.8$

the time period during which statistically steady state is reached (see Fig. 4.4 for $Re = 37.8$). The cell distance from centerline increases with increasing La number

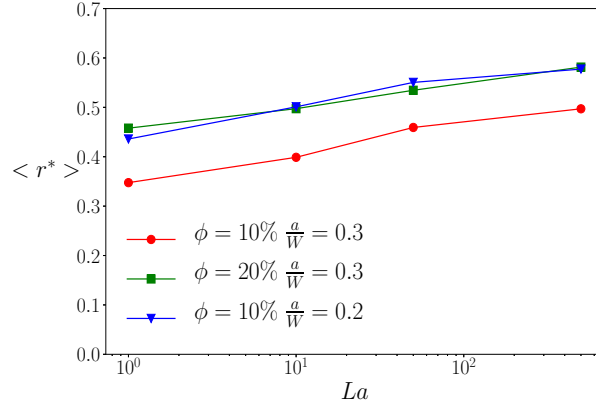


Fig. 4.4. Quasi-steady cell distance from the centerline for various La number at $Re = 37.8$

(decreasing deformability) which is in agreement with the behavior of a single cell in a microchannel [54, 71]. This change is attributed to the effect of La number on the deformability-induced force. As La increases this force gets weaker and the inertial and wall-induced forces become dominant factors. Hence, the location of cells with a high Laplace number is close to that of solid particle flowing in a microchannel. Figure

4.4 also exhibits that increasing the cell volume fraction leads to increase in the cell distance from the channel centerline. This behavior is due to the increase in the cell-cell interaction due to the increase in the number of cells flowing in the channel. Furthermore, the cell size has an important role on the net motion of cells. Comparing the average distance for different blockage ratios ($\frac{a}{W} = 0.2$ and 0.3) indicates that bigger cells get closer to the centerline consistent with previous studies [54, 71] for an isolated cell. According to *Schaaf et al.* [54], the deformability-induced forces scale proportionally with the size of the cells. Hence, the bigger cells experience a larger force towards the centerline. In order to study the steady distribution of cells in microchannel, two quantities including radial volume fraction (ϕ_r) and local volume fraction (ϕ_l) are defined. The local volume fraction represents the cell distribution across the microchannel and is defined as the fraction of volume $\Delta y \Delta z L_x$ (L_x is the channel length in x direction) occupied by the cells at different y and z across the channel cross-section. To find ϕ_r , eq. 4.1 is introduced.

$$\phi_r = \frac{1}{A_{r,r+\Delta r}} \int_r^{r+\Delta r} \phi_l 2\pi r dr, \quad (4.1)$$

In this equation, r is the distance from the channel centerline and $A_{r,r+\Delta r}$ is the area between r and $r + \Delta r$. Hence, the radial volume fraction (ϕ_r) is the fraction of microchannel volume between r and $r + \Delta r$ that is occupied by cells. The radial volume fraction for $\phi = 10\%$, $\frac{a}{W} = 0.3$ is plotted for various Laplace number in Fig. 4.5(a). According to this figure, the cells are not evenly distributed across the channel. The results show that the radial volume fraction of cells decreases with the distance from the channel centerline and it reaches to zero at a particular radius. The region in the microchannel in which the radial volume fraction is zero is called cell-free layer (CFL). The formation of this layer has been numerically and experimentally observed in previous studies [112, 113]. Furthermore, the same phenomenon occurs in blood

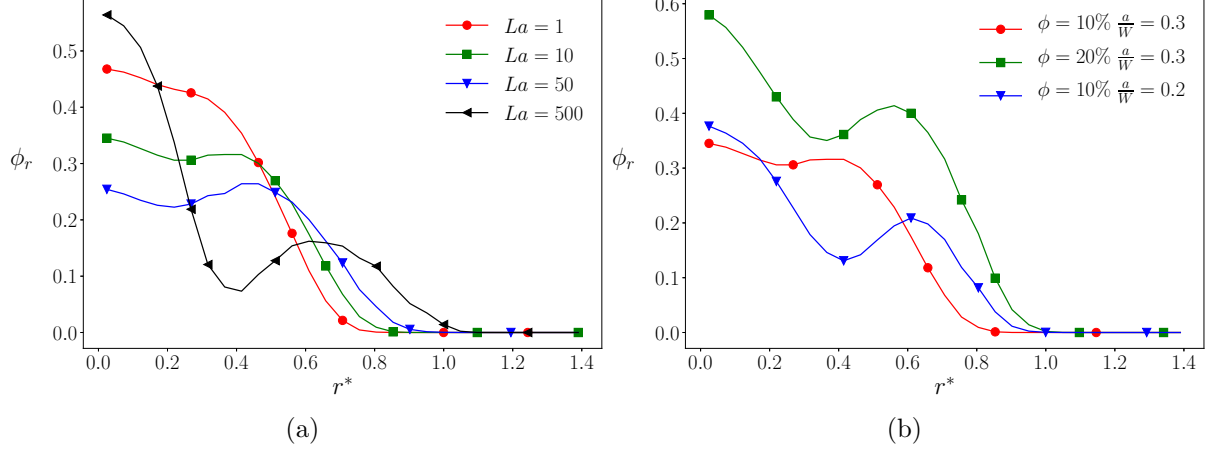


Fig. 4.5. Radial volume fraction for (a) $\phi = 10\%$, $\frac{a}{W} = 0.3$ and $Re = 37.8$ and (b) for $La = 500$ and $Re = 37.8$

vessels where the concentration of the red blood cells close to the vessel wall is far less than its value in the core region [114]. One of the important factors affecting the thickness of CFL is La number. The thickness of CFL increases with decreasing La number (Fig. 4.5(a)). The reason for this behavior is the tendency of deformable cells to migrate toward the core region and this tendency is enhanced by decreasing La number. Hence, the concentration of cells is higher in the central region leading to a thicker cell-depleted layer near the wall. The maximum radial volume fraction of cells at $La = 1$ occurs at the centerline and it decreases monotonously with the distance. The occurrence of the peak at the centerline is caused by two factors: (i) cell migration toward the centerline that yields to a significant cell accumulation in that region and (ii) the small area of the region ($A_{r,r+\Delta r}$) over which the radial volume fraction is computed in the central region. As the Laplace number increases an off-center peak in the radial volume fraction occurs, although the maximum radial volume fraction still occurs at the centerline due to the aforementioned reasons. In order to better understand this trend in cell distribution, the effect of deformability on the focal position of cells should be considered. Increasing the La number pushes

the focal position of cells toward the wall of the microchannel [54, 71]. Therefore, a significant increase in the local volume fraction of cells is observed at off-center locations in the cross-section. This rise in the local volume fraction is reflected as the second peak in the radial volume fraction in Fig. 4.5(a). The effect of the cell volume fraction (ϕ) and the cell size on the cell distribution is plotted in Fig. 4.5(b). The thickness of CFL decreases with ϕ due to the increase in the number of the cells and their interaction. Hence, the cells are more spread across the channel cross-section leading to a decrease in CFL thickness. Furthermore, decrease in the cell size results in decrease in the CFL thickness. This effect is attributed to the role of the cell size on the equilibrium position of cells shown in Fig. 4.4. More importantly, the formation of the second peak is also observed for all the cases shown in Fig. 4.5(b). In order to elaborate the formation of the second peak in the radial volume fraction in details, the local volume fraction of cells (ϕ_l) in the channel cross-section at $\phi = 20\%$, $La = 10$ and $\frac{a}{W} = 0.3$ is plotted in Fig. 4.6. The blue region near the channel wall

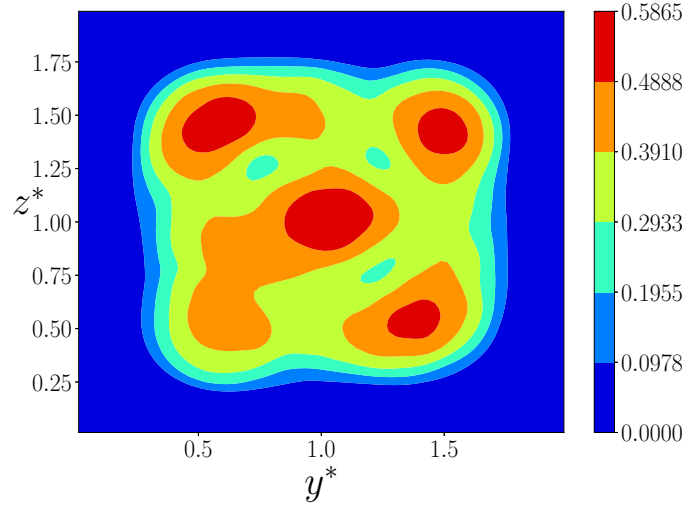


Fig. 4.6. Local volume fraction of cells at $\phi = 20\%$, $La = 10$, $\frac{a}{W} = 0.3$ and $Re = 37.8$

with zero concentration of cells is the cell free layer. According to this figure, ϕ_l has

its maximum values at the center and at off-center locations shown by red regions. The off-center red regions in the channel cross-section lead to the formation of the second peak in radial volume fraction (ϕ_r) in Fig. 4.5. This phenomenon is also observed in previous studies [112,115] in which suspension of droplets and capsules were studied.

One of the important factors in evaluating the performance of microfluidic devices is the sample throughput. Hence, we plot the volumetric flow rate of the suspension exiting the microchannel (Q^*) for various Laplace numbers in Fig. 4.7 to quantify the throughput of the microdevices. Our results show that the volumetric flow rate

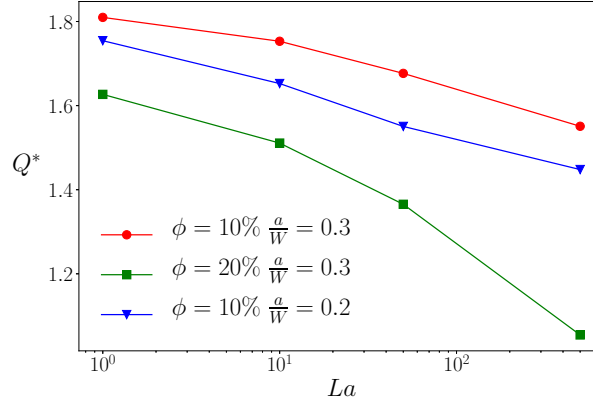


Fig. 4.7. The volumetric flow rate of the suspension for various La , ϕ and size at $Re = 37.8$

deceases with increasing Laplace number. This effect can be elaborated by considering the single cell dynamics in a microchannel. According to our previous study [58,71], a single cell flowing in the microchannel lags the surrounding fluid and its velocity is smaller than the local velocity of the fluid in the absence of the cell. This effect becomes more significant as the Laplace increases. Hence, the reduction of volumetric flow rate with increase in La is expected. In order to quantify the effect of the cell deformability on the flow field, the velocity profile in the cross-section of microchannel is plotted for various La numbera in Fig. 4.8. Our results show that decreasing the

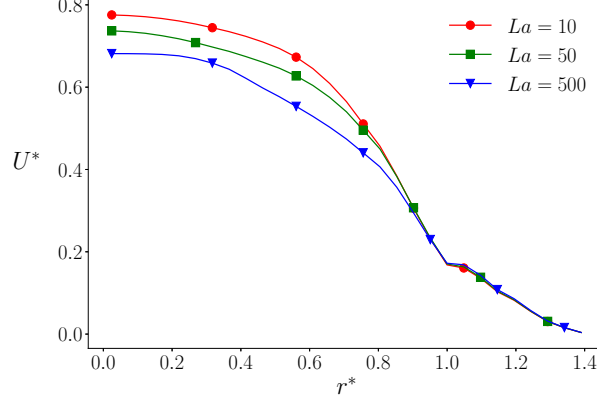


Fig. 4.8. The velocity profile in the microchannel at $\phi = 10\%$, $\frac{a}{W} = 0.3$ and $Re = 37.8$

cell deformability results in decrease in the velocity distribution across the cross-section. Furthermore, the velocity profiles for various La numbers are identical in the cell depleted region, while they are different in the regions occupied by the flowing cells. Figure 4.7 shows that the volumetric flow rate is also influenced by the cell volume fraction (ϕ) and the cell size. Accordingly, the reduction in the volumetric flow rate is observed with increasing the volume fraction (ϕ), while increasing the cell size ($\frac{a}{W}$) enhances Q^* . Here, we also study the effect of Reynolds number on the cell migration in the microchannel. In this work, we simulate the motion of cells at $\phi = 10\%$, $La = 500$ and two different cell sizes ($\frac{a}{W} = 0.2$ and 0.3) for various Re numbers. The average distance of the cells ($\langle r^* \rangle$) is plotted in Fig. 4.9. Our result

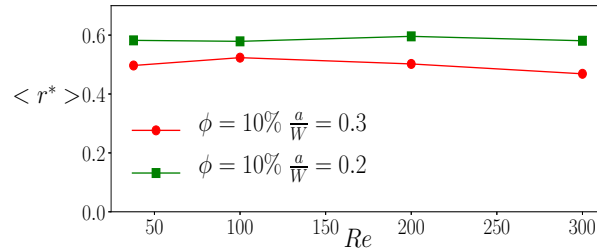


Fig. 4.9. Average cell distance for $\phi = 10\%$, $La = 500$ and $\frac{a}{W} = 0.2$ and 0.3

shows that the average cell distance is not influenced by Reynolds number. This behavior is in agreement with previous studies [58,71] that investigated the dynamics of a solid particle and a deformable capsule with high La number in a microchannel. Furthermore, the radial volume fraction distribution (ϕ_r) for the cell suspension with $\frac{a}{W} = 0.2$ is plotted in Fig. 4.10. This result also emphasizes that the steady spatial

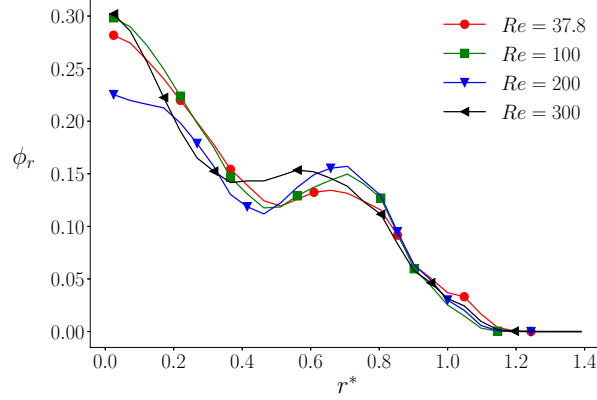


Fig. 4.10. Radial volume fraction distribution for $\phi = 10\%$, $La = 500$ and $\frac{a}{W} = 0.2$

distribution of flowing cells is not affected by the Reynolds number and the change in the CFL thickness is negligible.

4.4.2 Viscoelastic fluid

In this section, the effect of the polymeric fluid on the cell migration behavior is investigated. As it is mentioned in section 4.4.1, the migration of the cells is governed by the interplay between inertial lift force, deformability-induced force, wall-induced force and cell-cell interaction. However, the cells flowing in a polymeric fluid experience an elastic force beside other forces. The elastic force is generated due to the deformation of polymer chains in the channel flow. The interplay between various forces determines the cell distribution in the channel. The motion and the quasi-steady distance of cells suspended in a polymeric fluid is significantly influenced

by the fluid elasticity. Figure. 4.11 plots the temporal evolution of the average cell

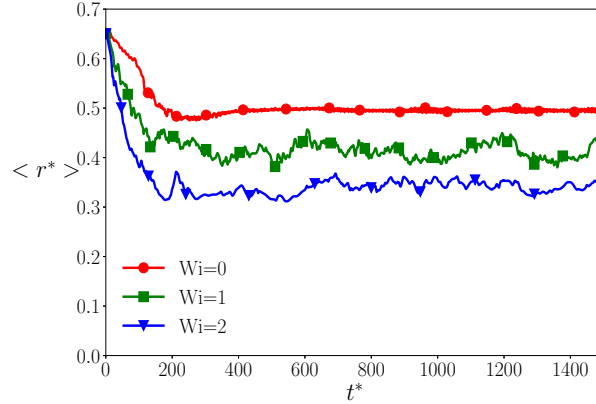


Fig. 4.11. Temporal evolution of cell distance from the centerline for $\phi = 10\%$, $\frac{a}{W} = 0.3$, $La = 500$ and $Re = 37.8$

distance from the channel centerline at $\phi = 10\%$, $La = 500$ and $\frac{a}{W} = 0.3$ for various Wi numbers ($Wi = 0$ corresponds to a Newtonian fluid). Our results show that the cell distance decreases as Wi number increases. Therefore, the constant-viscosity viscoelastic fluid pushes the cells toward the channel centerline. This behavior is in agreement with previous numerical and experimental studies [57,58,71] for an isolated cell. This result suggests that the polymeric fluid can be used as a passive method in devices in which the main goal is cell focusing at the centerline such as cytometers. Furthermore, this method adds another variable to be tuned by the user to control the focal position of the cells in microfluidic devices. According to the results, the deformability-induced force and elastic force have reinforcing effect that drives the cells toward the centerline, while the inertial force has the opposite effect that pushes the cells toward the channel wall. Therefore, for low Wi number the inertial force is dominant and the resulting average cell distance is close to that of cells flowing in a Newtonian fluid, while for high Wi number the elastic force has a significant effect and the cells accumulate in the centerline. This effect is plotted in Fig. 4.12 which shows the cell configuration for $\phi = 10\%$, $La = 500$ and $\frac{a}{W} = 0.2$ for two different

values of Weissenberg number ($Wi = 0$ and 0.2). According to this figure, the cells flowing in a constant-viscosity viscoelastic fluid (Fig. 4.12(b)) focus more in the centerline compared to the cells flowing in a Newtonian fluid (Fig. 4.12(a)). In order

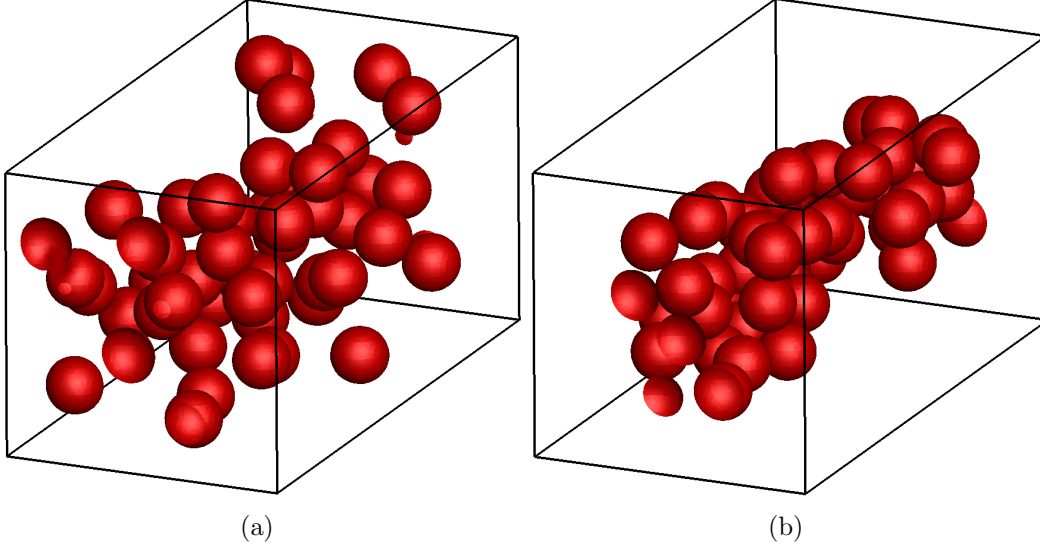


Fig. 4.12. The distribution of cells at $\phi = 10\%$, $La = 500$, $Re = 37.8$, $\frac{a}{W} = 0.2$ and (a) $Wi = 0$ and (b) $Wi = 2$

to quantify the effect of polymeric fluid, the quasi-steady value of the average cell distance ($\langle r^* \rangle$) for various cell sizes and volume fractions is plotted as a function of Wi number in Fig. 4.13. The cell distance from the centerline decreases with increase in Wi number for various ϕ and $\frac{a}{W}$. The decrease in $\langle r^* \rangle$ continues until the Wi number reaches a critical value above which the cell distance does not reduce further and reaches a plateau. This behavior is attributed to the cell-cell interaction that has an opposing effect against elastic effect and does not allow the cells to focus at the centerline. In other word, the cells are accumulated in the core region and the distance between the cells cannot be further reduced. This effect can be seen in Fig. 4.12 (b) that illustrates the distribution of cells in the central region. As it is shown in Fig. 4.13, the cell distance is not computed for Wi above 2 for two

cases ($\phi = 20\%$, $\frac{a}{W} = 0.3$ and $\phi = 10\%$, $\frac{a}{W} = 0.2$). The lack of data for these cases is due to the numerical instability occurring for larger Wi numbers and volume fractions. The effect of the cell volume fraction (ϕ) and the cell size ($\frac{a}{W}$) is similar to their effect in a Newtonian fluid. Increasing the volume fraction increases the cell distance and increasing the cell size decreases the cell distance from the centerline. In

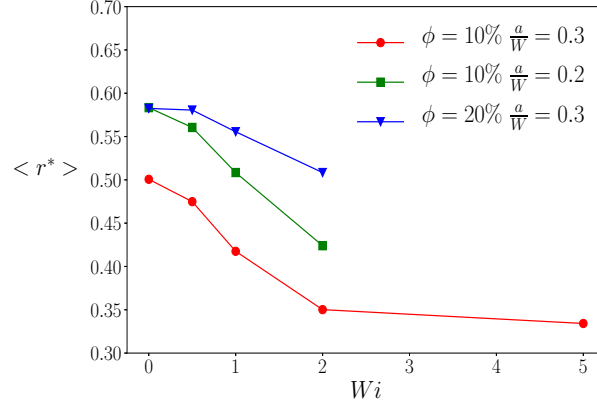


Fig. 4.13. Quasi-steady cell distance from the centerline for various Wi number at $Re = 37.8$

order to study the effect of elasticity on CFL thickness, the radial volume fraction is plotted in Fig. 4.14 for $\phi = 10\%$, $\frac{a}{W} = 0.3$ and $Re = 37.8$. The thickness of the CFL increases with increasing Wi number. This change is attributed to the polymer chains driving the cells more effectively toward the centerline with increasing Wi number. Hence, a larger region in the vicinity of channel walls remain depleted from the cells. Furthermore, the location of the off-center peak in the radial volume fraction of the cells approaches to the centerline as the elasticity of the suspending fluid increases which is also due to the enhanced tendency of the cells in accumulating in the core region. The effect of the polymeric fluid on the throughput of microfluidic devices is also studied in this section. The volumetric flow rate of the exiting suspension is measured under various Wi numbers and constant pressure-gradient at $\phi = 10\%$, $\frac{a}{W} = 0.3$ and $Re = 37.8$ and is plotted in Fig. 4.15(a). Our results show that the

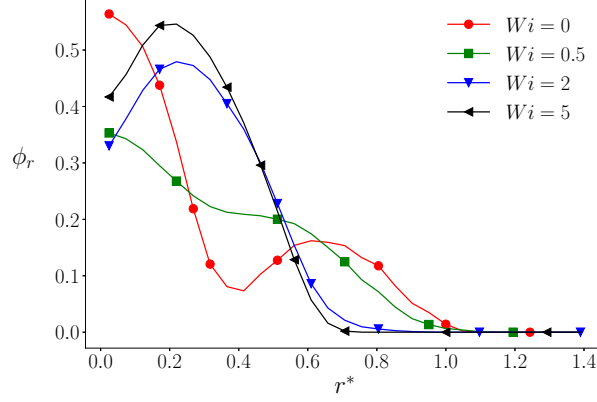


Fig. 4.14. Radial volume fraction of cells for $\phi = 10\%$, $\frac{a}{W} = 0.3$ and $Re = 37.8$

volumetric flow rate increases with increasing Wi number. In order to elaborate this effect, the velocity profile of the corresponding cases in the channel cross-section is plotted in Fig. 4.15(b). As Wi number increases, the velocity at centerline ($r^* = 0$) increases and the velocity profile becomes flatter in the central region. Therefore, the change in the velocity distribution across the microchannel due to the change in fluid elasticity results in the enhanced sample throughput in microfluidic devices. Furthermore, Fig. 4.15(a) shows that there is a critical Wi_c number above which the volumetric flow rate reaches a plateau. This change is attributed to the accumulation of cells in the core region where cells cannot be more compact above the critical Wi_c number. Besides, the effect of Reynolds number on the performance of the microfluidic devices in presence of polymeric fluids is investigated. The quasi-steady cell distance is plotted for various Re numbers at $\phi = 10\%$, $La = 500$ and $Wi = 2$ in Fig. 4.16. As it is shown, the distance of the cells from the centerline increases with increasing the Re number. This finding is in agreement with previous studies [58, 71] in which the dynamics of an isolated solid and deformable particle were studied in a microchannel. This behavior can be elaborated according to the strong dependence of inertial and elastic forces on Re number. The interaction between various forces such as inertial

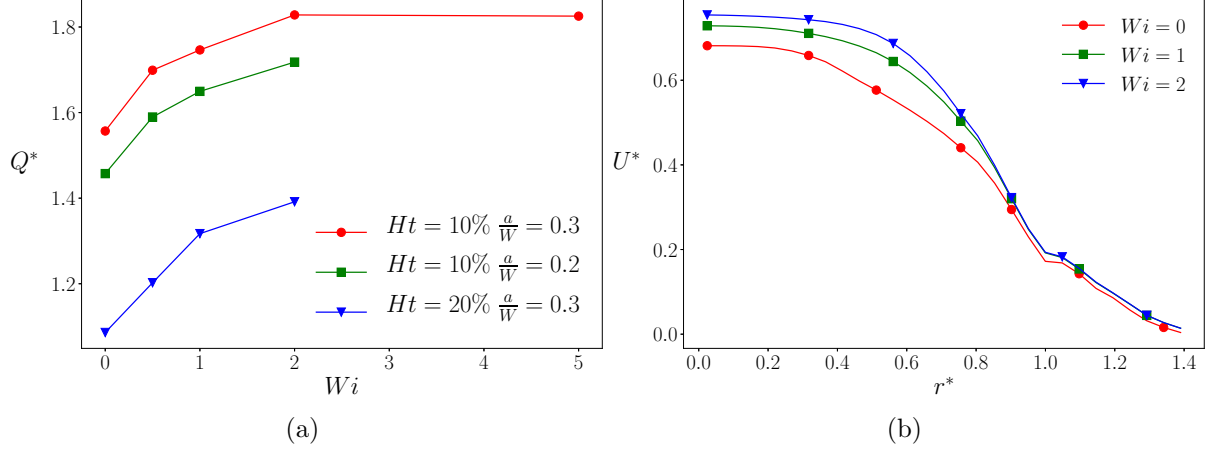


Fig. 4.15. (a) Volumetric flow rate of suspension for various Wi number at $Re = 37.8$ and (b) the velocity profile at $\phi = 10\%$, $La = 500$, $\frac{a}{W} = 0.3$ and $Re = 37.8$

and elastic forces determines the final position of cells in the microchannel. The inertial effect is the dominant factor when $Re \gg Wi$ and the cells are expected to be driven toward the walls, while for the case where $Wi \gg Re$ the elastic force become dominant the the cells tend to accumulate in the central region of the microchannel.

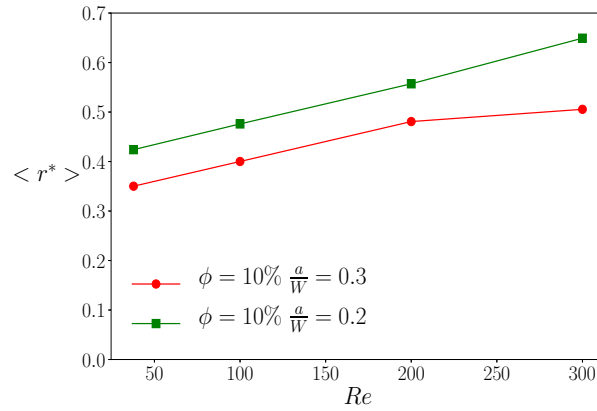


Fig. 4.16. Quasi-steady cell distance for various Re number at $\phi = 10\%$, $La = 500$ and $Wi = 2$

4.5 Conclusions

In this work, the dynamics of cell suspension flowing in Newtonian and viscoelastic fluids is investigated. We study the effect of the cell size ($\frac{a}{W}$), cell volume fraction (ϕ), inertia (Re), deformability (La) and fluid elasticity (Wi) on the motion of cell suspension and the performance of the microfluidic devices composed of a straight microchannel. The variation of the aforementioned factors, changes the governing forces and influences the distribution of cells in the microchannel. Our results show that increasing the La number leads to the increase in the cell distance from the channel centerline (r^*) and reduction in the volumetric flow rate of the exiting flow (Q^*). These variables are also affected by the cell size and cell volume fraction. Increasing the cell size pushes the cells further toward the wall and this effect can be reinforced by increasing the cell volume fraction. However, the increase in $\frac{a}{W}$ and ϕ has an opposite effect on the volumetric flow rate and causes the decrease in Q^* . Our findings suggest that adding the polymer in suspending fluid pushes the cells further toward the centerline compared to a Newtonian fluid and can be used in devices that require centerline focusing of the cells such as cytometers. It is shown that increasing fluid elasticity (Wi) yields the reduction in cell distance from the centerline, while it increases the volumetric flow rate of the exiting flow. Furthermore, the effect of the inertia (Re) is investigated for both Newtonian and viscoelastic fluids. The results indicate that the change in the Reynolds number does not significantly affect the suspension dynamics, while an opposite behavior is observed in a viscoelastic fluid in which the cells are driven further toward the wall due to increasing the inertial effects.

4.6 Appendix

In order to check the mesh and the domain size independency of the cell suspension in a microchannel, we follow the method used in *Doddi et. al* [116] which the volumetric flow rate of the flow is investigated for various grid and domain sizes. Figure 4.17.(a) shows the the volumetric flow rate of the cell suspension in a Newtonian fluid at $Re = 100$, $\phi = 10\%$ and $\frac{a}{W} = 0.3$ for various La numbers with $128 \times 76 \times 76$ and $200 \times 133 \times 133$ grid points in x, y and z directions, respectively. The maximum error between two different grid sizes is 2.44%. Hence, our results indicate that the numerical simulation performed in this study is independent of the mesh sizes. The results for the domain independency of the simulation is also plotted in Fig. 4.17(b). The variation of the volumetric flow rate at $Re = 100$, $\phi = 10\%$ and $\frac{a}{W} = 0.3$ for two different domain sizes ($L_x = 4W$ and $8W$) in the x direction along which the periodic boundary condition is considered. The maximum error between two channel geometries is 0.71% that proves the independency of the numerical results against the computational domain size.

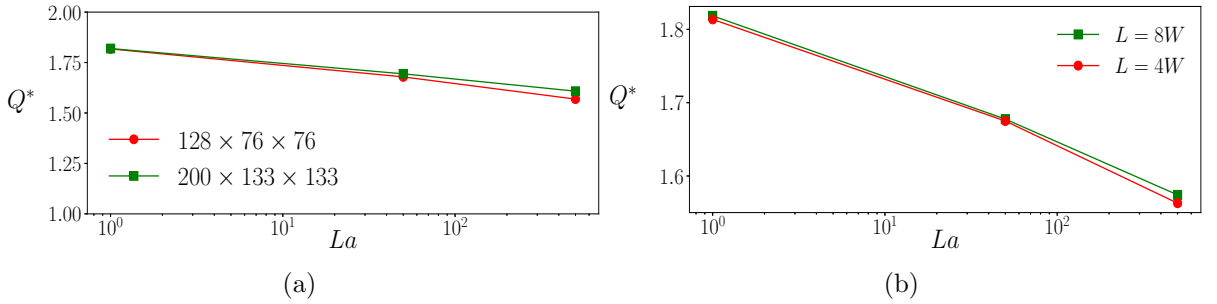


Fig. 4.17. The volumetric flow rate at $Re = 100$, $\phi = 10\%$ and $\frac{a}{W} = 0.3$ (a) for $128 \times 76 \times 76$ and $200 \times 133 \times 133$ grid points and (b) for $L_x = 4W$ and $8W$ in x direction

5. NUMERICAL INVESTIGATION OF ELASTO-INERTIAL PARTICLE FOCUSING PATTERNS IN VISCOELASTIC MICROFLUIDIC DEVICES

This chapter is reproduced with permission from: A.H. Raffee, A.M. Ardekani, S. Dabiri, Numerical investigation of elasto-inertial particle focusing patterns in viscoelastic microfluidic devices”, *Journal of Non-Newtonian Fluid Mechanics*, 272, 104166. [117]

5.1 Summary

Viscoelastic microfluidic devices are promising for various microscale procedures such as particle sorting and separation. In this chapter, we perform three dimensional computational investigation of a particle in a viscoelastic channel flow by considering combined inertial and elastic effects. We calculate equilibrium positions of the particle in the microchannel for a wide range of Reynolds and Weissenberg numbers, which are important in the design of microfluidic devices. The results provide an insight into the motion of cells and particles and explain the findings of previous experiments. Furthermore, we suggest new particle behaviors that have not been found before. Ultimately, a phase diagram is provided to predict the particle dynamics under a wide range of inertial and elastic effects.

5.2 Introduction

Microfluidic devices have been widely used in biomedical devices. These devices have significantly enhanced therapeutic, diagnostic and many industrial procedures by

increasing accuracy and accelerating the processes [21, 29, 39, 118–121]. Isolation and separation of rare cells from a heterogeneous population of cells is a critical process in early diagnosis of fatal diseases such as cancer [25] and malaria [26]. Furthermore, the isolated cells such as rare blood components can be used for therapeutic purposes. For instance, platelet-rich plasma are used in transfusion [21, 28] or stem cells can be found in blood samples [21]. Enriching the cell population provides a platform to biologists to conduct physical and chemical analysis on cells [122–127].

In order to accomplish the desired tasks in aforementioned applications the precise control of particles is required [99]. Hence, developing new techniques for the manipulation of particle trajectory has been the subject of many studies in the past decade. Some of these techniques are designed based on the use of externally applied forces generated by electric [93], magnetic [94] and acoustic [95] fields. These methods offer high sample processing rates [21], however, there are many factors that prevent them from widely being used in clinical applications. Mainly, these methods work based on biochemical labeling of the cells that may affect the cell function and properties [21, 29]. Furthermore, the cost and complexity of the process can also be considered as an important downside for these methods [21]. Hence, there is a growing interest in developing label-free techniques that introduce advantages such as accurate analysis, low sample use and low cost operations [29]. In this regard, inertial microfluidic devices are used to manipulate particle trajectories in microchannels.

[35] first reported the transverse migration of particles due to inertial forces in a straight tube filled by a Newtonian fluid [35]. The hydrodynamic interaction between the flowing particles and the ambient fluid can be used to manipulate the trajectory of particles. This effect was studied theoretically by [43] in which they considered the dynamics of a rigid sphere in a 2D Poiseuille flow and a simple shear flow and predicted the equilibrium locations of the particle in these flows. Furthermore, they

showed that the final location of the particle is independent of releasing point in the microchannel. [128] also theoretically investigated the lateral migration of a solid particle in a circular tube. They studied the motion of a buoyant and neutrally buoyant particle in a Poiseuille flow and showed that their findings agree well with experiments. Many microfluidic setups are designed based on inertial migration of particles to control the location of targeted cells in microchannels, particularly for sorting and separation of the cells [86, 100, 101, 105, 129, 130]. The efficiency of this method reduces in cases where the targeted cells are small or the flow rate is low [99, 104, 131]. Viscoelastic microfluidics are developed to address this issue by replacing the Newtonian ambient fluid by a dilute polymer solution [131]. The solute polymer chains get deformed in the induced flow field and exert an additional elastic force on the particle. The resulting force affects the particle migration along with the inertial force [99, 105]. Previous studies show that the direction and the magnitude of generated elastic force depends on the rheology of the polymer solution and the volumetric flow rate of the suspending fluid [79, 131, 132].

Transverse migration of a particle suspended in a viscoelastic fluid is caused by the lift force generated due to the interaction between ambient flow and the particle [77, 133, 134]. This lift force comprises an inertial lift force (F_{in}) and an elastic lift force (F_{el}). The inertial lift force can be decomposed into two forces: (i) shear-gradient lift force (F_{s-in}) that arises from the non-uniform velocity profile across the channel and drives the particle away from the channel center and (ii) wall-induced lift force (F_{w-in}) that is caused by the uneven distribution of the vorticity around the particle that leads to higher pressure in the gap between the wall and the particle and pushes the particle away from the wall [41, 43, 135, 136]. These forces have been investigated extensively in the literature and there are experimental [45, 46], numerical [47, 76, 137, 138] and analytical [40, 43, 133, 134] works proposing scaling relations for the total inertial force

in square and rectangular microchannels. On the other hand, the elastic force acts on the particle due to non-uniform distribution of normal stress difference across the channel [77,139]. In this phenomenon, the first normal stress difference (N_1) generates a stream-wise tension and the second normal stress difference (N_2) gives rise to a secondary flow in the cross section [107]. There are numerical [71, 87, 107, 140, 141] and experimental [99,110] studies investigating the particle migration in a viscoelastic fluid. Here, in this work we focus on illustrating the distribution of elastic and inertial forces acting on a particle in a viscoelastic channel flow and calculating the equilibrium positions of the particle in the channel cross section.

In order to understand the mechanism of particle migration in a viscoelastic fluid, fully resolved 3D numerical simulations are conducted. In this work, we show the distribution of lift force acting on the particle in a viscoelastic fluid and investigate the influence of combined elastic and inertial forces on the particle behavior in a microchannel. Furthermore, the location of equilibrium points and their corresponding stability are determined for $1 < Re < 30$ and $0 < Wi < 3$ which is important for designing the microfluidic devices relying on viscoelastic effects. Our results explain various focusing pattern of particles observed in previous experimental works by scrutinizing the stability of equilibrium points. We also predict new behaviors that have not been discovered in the past studies.

5.3 Mathematical modeling

In this work, we study the dynamics of a solid spherical particle suspended in a straight, square microchannel. The particle is neutrally buoyant and the ambient fluid is viscoelastic. The radius of the sphere is represented by a and the channel side and its length are $2w$ and L , respectively. In this problem, the origin of the reference frame is located at the channel center and x , y and z directions are aligned with the

streamwise, horizontal and vertical directions, respectively, as illustrated in Fig. 5.1. The particle is initially at rest and a constant pressure gradient is applied in the x direction, driving the flow in the microchannel. In order to simulate the hydrodynamic interaction between the particle and the surrounding fluid, an incompressible Navier-Stokes equation is numerically solved as follows:

$$\nabla \cdot \mathbf{u} = 0, \quad (5.1)$$

$$\frac{\partial(\rho \mathbf{u})}{\partial t} + \nabla \cdot (\rho \mathbf{u} \mathbf{u}) = -\nabla p + \nabla \cdot \boldsymbol{\tau} + \mathbf{F}, \quad (5.2)$$

where ρ is the fluid density, \mathbf{u} is the velocity vector, t denotes the time and p and $\boldsymbol{\tau}$ represent the pressure and stress tensor, respectively. The particle density is assumed to be the same as the fluid density. A Distributed Lagrangian Multiplier (DLM) method is used to simulate the solid particle motion in the fluid. A forcing term \mathbf{F} is added in eq. 5.2 to enforce the rigid body motion of the particle. The details of DLM method can be found in [142]. The viscoelastic properties of the fluid can be modeled by splitting the stress tensor into two parts: (i) the contribution from solvent $\boldsymbol{\tau}_s$ and (ii) that of polymer $\boldsymbol{\tau}_p$. Hence, the total stress tensor can be written as:

$$\boldsymbol{\tau} = \boldsymbol{\tau}_s + \boldsymbol{\tau}_p. \quad (5.3)$$

The Newtonian viscous stress is described as $\boldsymbol{\tau}_s = \mu_s(\nabla \mathbf{u} + \nabla \mathbf{u}^T)$, where μ_s represents the solvent viscosity. The Giesekus constitutive equation [74] is used to model the viscoelastic behavior of the fluid. This model captures the shear-thinning behavior and constrained elongation of polymer chains in the fluid [58]. According to this model, the polymeric stress tensor is governed by:

$$\lambda \overset{\nabla}{\boldsymbol{\tau}}_p + \boldsymbol{\tau}_p + \frac{\alpha \lambda}{\mu_p} \boldsymbol{\tau}_p \cdot \boldsymbol{\tau}_p = \mu_p(\nabla \mathbf{u} + \nabla \mathbf{u}^T), \quad (5.4)$$

$$\overset{\nabla}{\boldsymbol{\tau}}_{\boldsymbol{p}} \equiv \frac{\partial \boldsymbol{\tau}_{\boldsymbol{p}}}{\partial t} + \mathbf{u} \cdot \nabla \boldsymbol{\tau}_{\boldsymbol{p}} - \nabla \mathbf{u} \boldsymbol{\tau}_{\boldsymbol{p}} - \boldsymbol{\tau}_{\boldsymbol{p}} \nabla \mathbf{u}^T. \quad (5.5)$$

Here λ represents the fluid relaxation time and μ_p and α denote the polymeric viscosity and the mobility factor. The following equations are used to calculate the total, elastic and inertial forces acting on the particle.

$$\mathbf{F}_{total} = - \oint_V \mathbf{F} dv, \quad (5.6)$$

$$\mathbf{F}_{el} = \int \boldsymbol{\tau}_{\boldsymbol{p}} \cdot \mathbf{n} ds, \quad (5.7)$$

$$\mathbf{F}_{in} = \mathbf{F}_{total} - \mathbf{F}_{el}, \quad (5.8)$$

where \mathbf{n} represents the unit vector normal to the particle surface and ds and dv denote differential elements of particle surface and volume, respectively. In this problem, the no-slip boundary condition is applied at the walls of the channel. These boundaries are normal to y and z directions. The periodic boundary condition is applied at the inlet and outlet of the computational domain. These boundaries are normal to the x direction. The microchannel length is set to $L = 20a$ to ensure the channel is long enough and the particle does not interact with its periodic image. The details of the numerical methods used in this work and their validations are reported in our previous works [58, 61, 71, 87]. We use w as the characteristic length scale and U_0 as the characteristic velocity scale (where U_0 is the undisturbed flow velocity at the channel center filled with a Newtonian fluid). Accordingly, the governing dimensionless numbers can be defined as: (i) $Re = \frac{\rho U_0 2w}{\mu}$, representing the ratio of inertial to the viscous forces in which the total viscosity is defined as $\mu = \mu_s + \mu_p$, (ii) the Weissenberg number $Wi = \frac{\lambda U_0}{w}$, representing the ratio of elastic to the viscous forces, (iii) $\beta = \frac{\mu_p}{\mu}$, representing the ratio of polymer viscosity to the total viscosity and (iv) blockage ratio $\frac{a}{w}$, describing the finite size of the flowing particle. In this

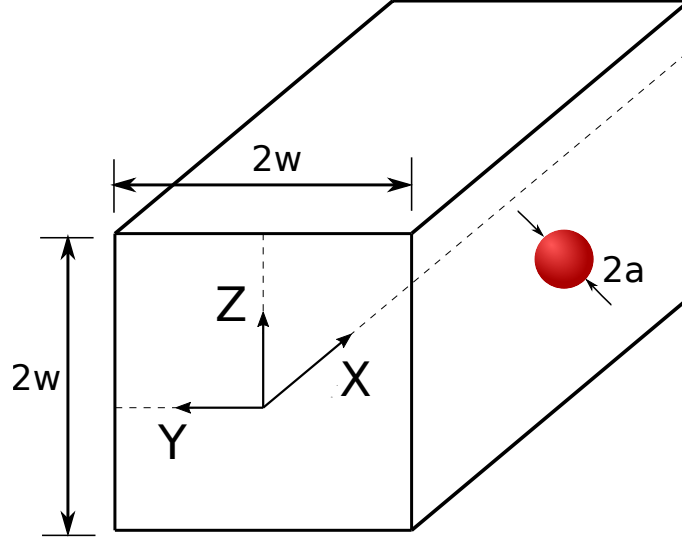


Fig. 5.1. Schematic of the problem setup

work, β , $\frac{a}{w}$ and α are set to 0.5, 0.3 and 0.2, respectively, unless otherwise stated. The particle has the same density as that of the fluid. It should be noted that the initial velocity of the fluid is set to the undisturbed flow velocity in the absence of the particle. In order to find the lift force distribution experienced by the particle across the channel cross section, the lateral position of the particle is fixed at the location where the lift force should be calculated. Consequently, the particle only travels along a line parallel to the x direction and it rotates freely around all directions. The particle is consequently not force-free and the elastic and inertial forces balance with the transverse force required to fix the transverse location of the particle. Hence, the dynamics of this particle is not the same as a force-free particle dynamics due to non-linearity of the problem, but the equilibrium positions and their instability are the same as the ones for a force-free particle. The particle is released with a zero initial velocity in the microchannel and the simulation continues until the ambient flow field reaches a steady state and then the lift force is calculated. This method is used to determine the particle's equilibrium locations and their corresponding stability across

the microchannel in a Newtonian fluid [49, 76, 83, 138, 143, 144]. The domain and grid size independency tests and the validation of the employed method are shown in the supplementary material.

5.4 Result and discussion

The migration of particles in Newtonian fluids has been extensively investigated by many researchers. According to the previous numerical and experimental studies [35, 39], the particles released in microchannel with a circular cross-section migrate toward an annulus ring with a radius of $\sim 0.6R$, where R represents the radius of microchannel. However, the particle dynamics changes in a square microchannel due to the reduced level of symmetry in the flow field [39, 58, 110]. In this case, the particles focus at four discrete points along the main axes of the microchannel. Considering the flow structure, there are nine equilibrium points, where the lateral force becomes zero, among which only four are stable. The rest exhibit unstable behavior, meaning the particles migrate away upon any disturbance in the flow [39, 76, 83]. This phenomenon is further explained in details in the following section. In this work, we investigate the stability and location of equilibrium points for the particles suspended in a viscoelastic fluid and we show the focusing patterns of particles for a wide range of Re and Wi numbers. The variety observed in the focusing patterns of particles indicates the promising effect of addition of polymers in microfluidic devices and we show that this method can be used for different applications without applying any changes to the geometry of the microchannel.

5.4.1 Migration in a low inertial regime

In order to find the location and stability of the equilibrium points in a viscoelastic fluid, the force field experienced by the particle is calculated. The particle size is fixed at $\frac{a}{w} = 0.3$ and the Reynolds number is set to $Re = 5$ in this section. Due to the symmetry of the problem, the force field is illustrated only for one quarter of the channel cross section. Figure 5.2(a) shows the lateral force profile acting on the particle at $Re = 5$ and $Wi = 0$.

In this figure, the location of the equilibrium points are indicated by red circles. The observed profile explains the particle configuration observed in [100], [81] and [76]. As shown in this figure, the radially directed forces drive the particle away from the center and the wall and push the particle toward an annulus ring across the channel marked with the dashed line. Hence, the particle primarily moves in the radial direction to reach the annulus ring. This motion is followed by the migration along the ring to focus at its equilibrium position along the main axes [83]. Considering the force-map illustrated in Fig. 5.2(a), there are four stable equilibrium points along the main axes and four unstable equilibrium points along the diagonal of the channel. The results indicate that the lateral force is also zero at the channel center, however, the force field around the channel center implies that this equilibrium point is unstable. The focusing pattern of particles for this force map that can be observed in experiments is presented in Fig. 5.2(b). In order to further investigate the location and stability of the equilibrium points, the lateral force profile along the y-direction (main axis of the microchannel, i.e., $z = 0$ and $y = 0$ lines in the cross section) is shown in Fig. 5.3 for $Re = 1$ and 5 and a wide range of Wi number.

According to Fig. 5.3(b), the force profile for $Re = 5$ and $Wi = 0$ crosses the dashed horizontal line at two points (one at the center and the other at $\sim 0.52w$). These points are identified as equilibrium points on the main axis and correspond to

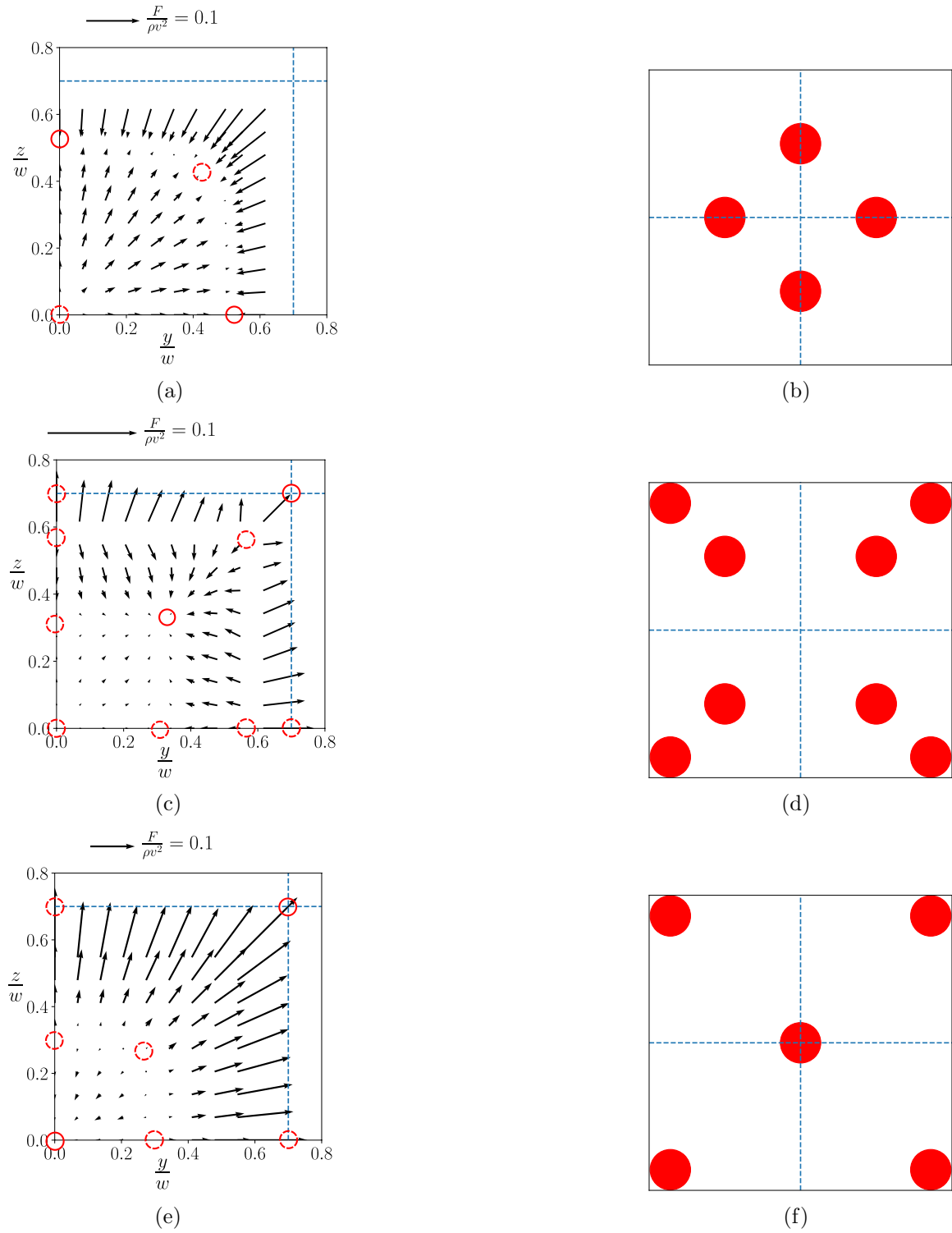


Fig. 5.2. Force-map accross the microchannel for $Re = 5$ and (a) $Wi = 0$ and (b) the focusing pattern (stable equilibrium positions) at $Wi = 0$, (c) force-map for $Wi = 0.1$ and (d) the focusing pattern for $Wi = 0.1$, (e) force-map for $Wi = 0.5$ and (f) the focusing pattern at $Wi = 0.5$.

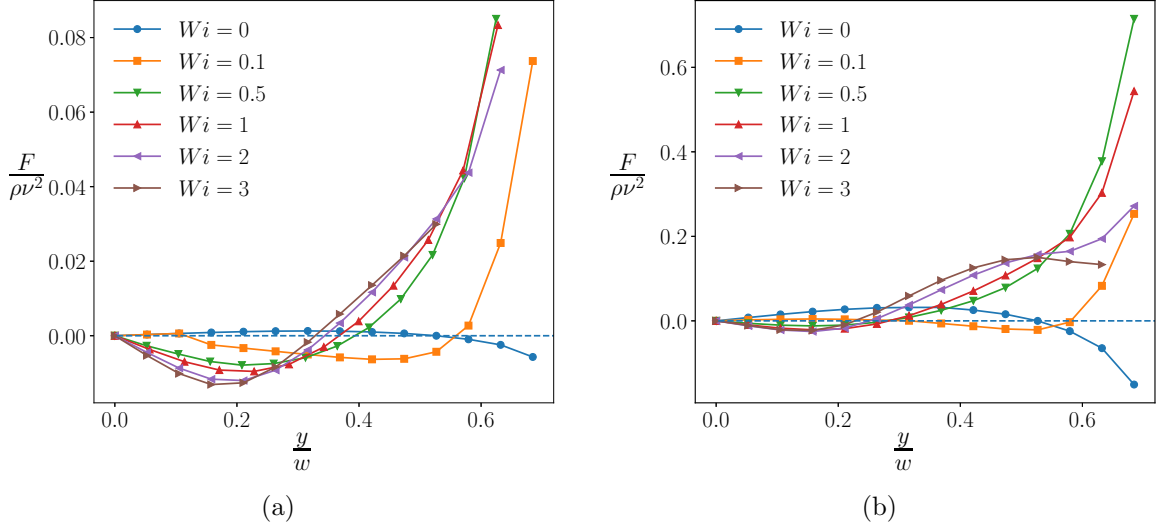


Fig. 5.3. Lateral force profile along the main axis for (a) $Re = 1$ and (b) $Re = 5$.

the locations where the lateral force is zero in Fig. 5.2(a). Stability of equilibrium points depends on the slope of the force profile at those locations. Hence, the center of channel is an unstable equilibrium point due to its positive slope, while the off-center equilibrium point is stable due to the negative slope of the force profile in that region. Increasing the Wi number changes the force field and consequently alters the focusing pattern of the particle. Figure 5.2(c) shows the lateral force acting on the particle for $Re = 5$ and $Wi = 0.1$. In the region constrained between two dashed curves the particle moves toward the center, while in the outer regions the particle moves toward the walls. A significant change in the force direction can be observed in the near wall region, where it is directed toward the wall in a viscoelastic fluid as opposed to a Newtonian fluid, where the particle is pushed away from the wall. Therefore, the corner becomes a basin of attraction for the particle at $Wi = 0.1$. According to the observed force-map, the expected focusing pattern is illustrated in Fig. 5.2(d). This result also rationalizes the particle behavior found in [110], where the particles aggregate at the corner and on the diagonal of the channel. The induced lateral force

results in the appearance of two equilibrium points along the diagonal line among which the one closer to the channel center is stable and the other one demonstrates an unstable behavior. Furthermore, there are three unstable equilibrium points on the main axis whose locations are shown in the force profile presented in Fig. 5.3(b). According to this profile, the channel center and the equilibrium point near the wall are unstable due to the positive slope of the force profile. The middle equilibrium point is also identified as an unstable point despite the negative slope of the curve. This behavior is attributed to the positive lateral force along the z -direction, which pushes the particle away from the main axis and turns this point to a sub-stable equilibrium point.

Figure 5.2(e) illustrates the force field for $Re = 5$ and $Wi = 0.5$. In this case the channel can be divided into two regions by a separatix. The region closer to the channel center (indicated by the region inside the dashed curve) attracts the particle toward the centerline, whereas the outer region pushes the particle toward the corner of the microchannel. Hence, only the channel center is stable and other equilibrium points along the diagonal of the channel and the main axes are unstable. It should be noted that the corner is also a basin of attraction for the particles. The corresponding focusing pattern is plotted in Fig. 5.2(f). The calculated force-map indicates the reason for the particle focusing pattern observed in previous experimental and numerical studies for the cases where the inertial effect is small and the elastic force is dominant [81, 99, 107, 110]. Figure 5.3(b) also shows a negative lateral force near the central region and a negative slope for the force profile at the center that leads to stability of the channel center. Another point that should be noted is the change in the force profile near the wall region as the lateral force decreases with increasing the elasticity effect for Wi above 0.5 in Fig. 5.3(b). As shown in Fig. 5.3, the change in Wi number alters the force profile significantly, leading to various focusing patterns

for the particles. This effect is more visible for smaller inertial effects as illustrated in Fig. 5.3(a) ($Re = 1$). Increasing the Wi number changes the convexity of the force profile along the main axis. In the Newtonian case ($Wi = 0$), the convexity of the force is negative along the entire axis, while it becomes positive for higher Wi numbers. Furthermore, the channel center which is unstable for $Wi = 0$, becomes stable for any Wi number above 0.5 and the corner becomes the basin of attraction. This change is observed for both $Re = 1$ and 5. According to Fig. 5.3(a) and (b), the location at which the force profile crosses the horizontal line in the range of $Wi > 0.5$ shifts toward the channel center with increasing elasticity. Hence, the size of the separatrix shrinks with Wi . This behavior can explain the results found in previous studies [99, 107, 110] as larger fraction of particles get attracted to the corner with increasing the elastic effects (Wi).

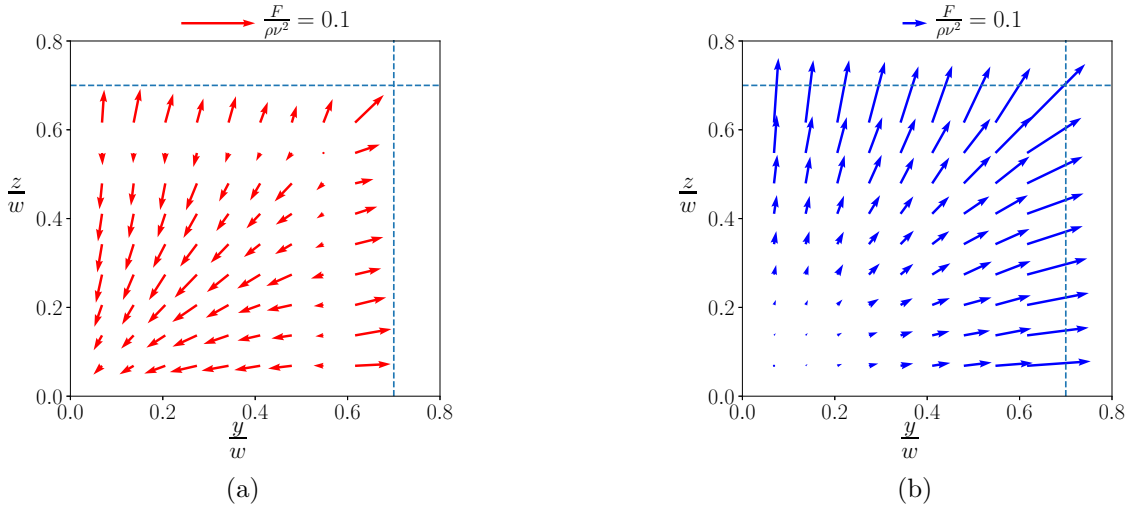


Fig. 5.4. Distribution of (a) elastic force and (b) inertial force at $Re = 5$ and $Wi = 0.5$

In order to investigate the effect of elasticity, particularly in the case where inertia is small, we split the lateral force plotted in Fig. 5.2(e) into two components: (i) elastic force (F_{el}) and (ii) inertial force (F_{in}). Figure 5.4 shows the distribution of

elastic and inertial forces for $Re = 5$ and $Wi = 0.5$. The elastic force (represented in Fig. 5.4(a)) drives the particle toward the center in the entire channel unless the particle is positioned near the wall region, where the elastic force direction reverses and the particle is pushed toward the wall. Contrary to the elastic force profile, the inertial force shown in Fig. 5.4(b) repels the particle from the center across the entire channel, however, the magnitude of the inertial force becomes negligible compared to that of elastic force for in the region close to the channel center. Hence, we observed a trapping region formed near the center of the microchannel and the particles that fall outside this region migrate to the corner. The comparison between elastic and inertial forces shown in Fig. 5.4 can explain the observed experimental results in previous studies. It should be noted that the magnitude of the elastic and inertial forces are significantly different for some cases and we use different force scale bars, which are shown in the figures.

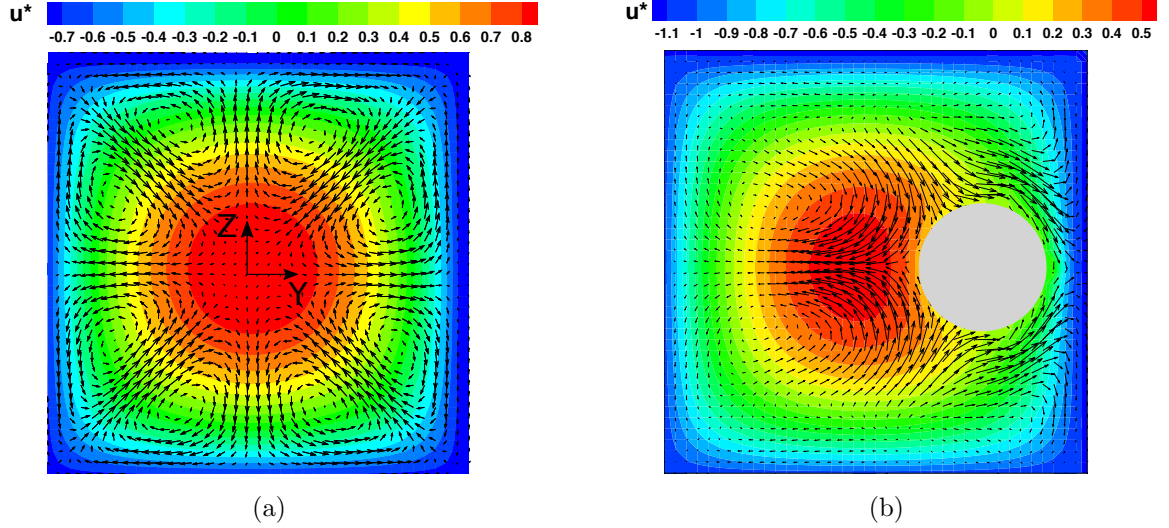


Fig. 5.5. Velocity profile at (a) the channel inlet and (b) the location of particle center at $Re = 5$ and $Wi = 3$. The stream-wise velocity is defined as $u^* = \frac{u}{U_0}$.

Figure 5.3 shows that increasing Wi number increases the magnitude of the lateral force near the channel center (for $Wi > 0.1$). This effect accelerates the transverse migration of the particle across the microchannel and leads to a shorter critical length for the microchannel required for complete focusing of the suspending particles [105, 107]. The second normal stress is non-zero in a Giesekus fluid modeled in this paper and it causes a secondary flow across the microchannel which affects the particle migration in the channel [58, 104, 107]. In order to show the effect of the secondary flow, the velocity profile is illustrated in Figure 5.5 at the channel inlet (far from the particle) and the location of particle center at $Re = 5$ and $Wi = 3$.

5.4.2 Migration in an intermediate inertial regime

In this section, we investigate the particle focusing pattern at $Re = 10$ for various Weissenberg numbers. The larger inertial effect leads to a significant change in the generated flow field compared to that of the previous section. This change can be reflected in the induced force-map shown in Fig. 5.6. Figure 5.6(a) illustrates the force field at $Wi = 0.1$. The noticeable difference between this case and the Newtonian fluid is the induced lateral force near the channel face center that attracts the particle toward the wall leading to the existence of a basin of attraction at the channel face.

Furthermore, the generated lateral force turns the equilibrium point on the diagonal of the channel stable and those on the main axes and channel center unstable. This phenomenon can be observed in Fig. 5.7, where the force profile along the main axis is plotted, showing the locations where the lateral force becomes zero and their corresponding stability status. Hence, the expected focal pattern looks like the one illustrated in Fig. 5.6(b) which has not been discovered in previous studies. Increasing the Wi number changes the force field significantly as displayed in Fig. 5.6(c). The radially directed lateral force drives the particle toward the channel corner across

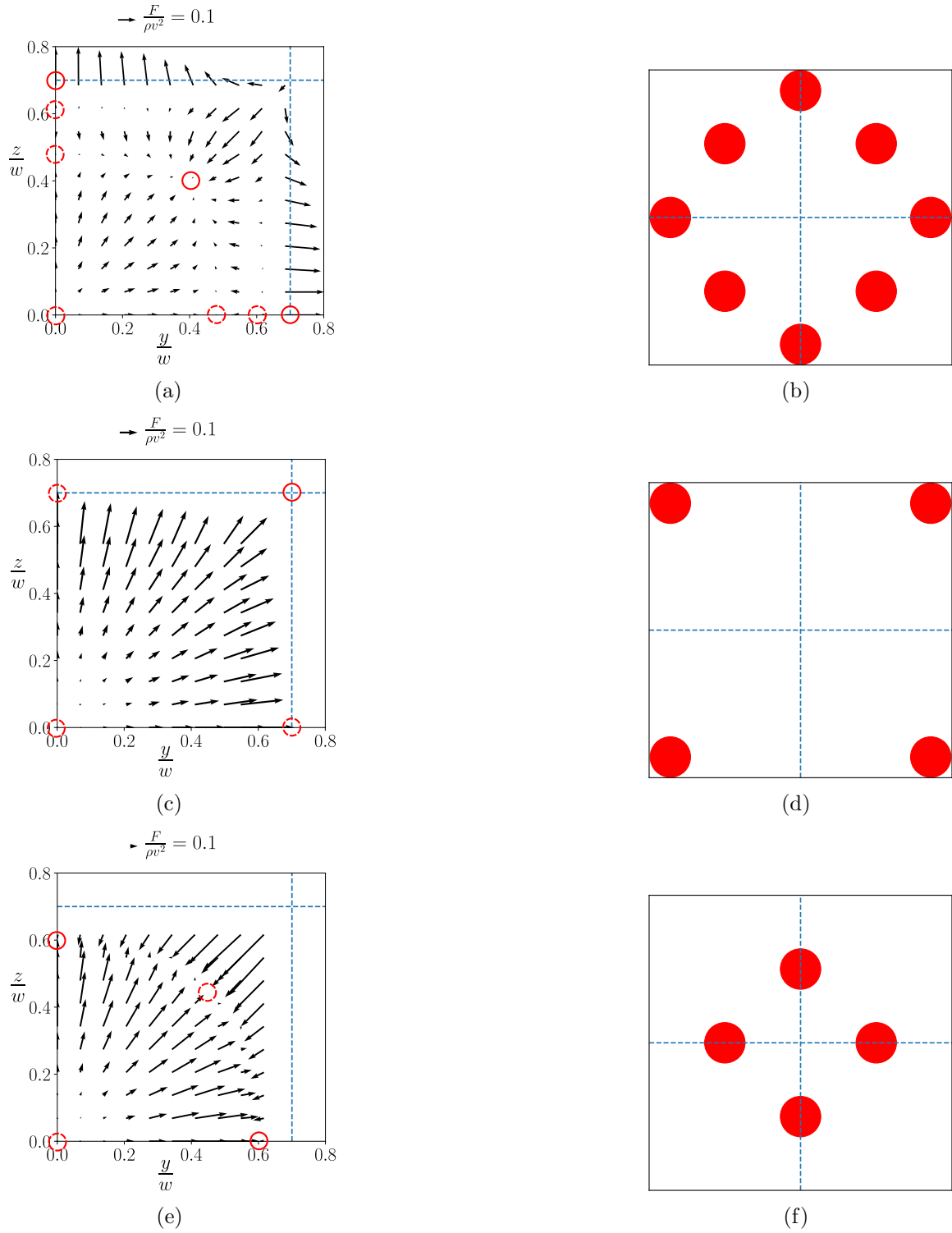


Fig. 5.6. Force-map across the microchannel for $Re = 10$ and (a) $Wi = 0.1$ and (b) the focusing pattern at $Wi = 0.1$, (c) force-map for $Wi = 0.5$ and (d) the focusing pattern for $Wi = 0.5$, (e) force-map for $Wi = 3$ and (f) the focusing pattern at $Wi = 3$.

the entire channel. Hence, the corner becomes the only basin of attraction resulting in the focal pattern presented in Fig. 5.6(d). Correspondingly, the positive value of the force along the entire main axis for $Wi = 0.5$ shown in Fig. 5.7 indicates that the particle is pushed away from the center regardless of its location in the microchannel. The calculated force field shown in Fig. 5.6(c) explains the particle configuration reported in previous experimental studies [99,110]. For $Wi = 3$, the lateral force has a distribution similar to that of a Newtonian fluid. In this case (shown in Fig. 5.6(e)) the radially directed force pushes the particle away from the wall and channel center and creates an annulus ring which is similar to the curve marked in Fig. 5.2(a). Consequently, the predicted focal pattern of the particle shown in Fig. 5.6(f) is similar to that of a Newtonian fluid.

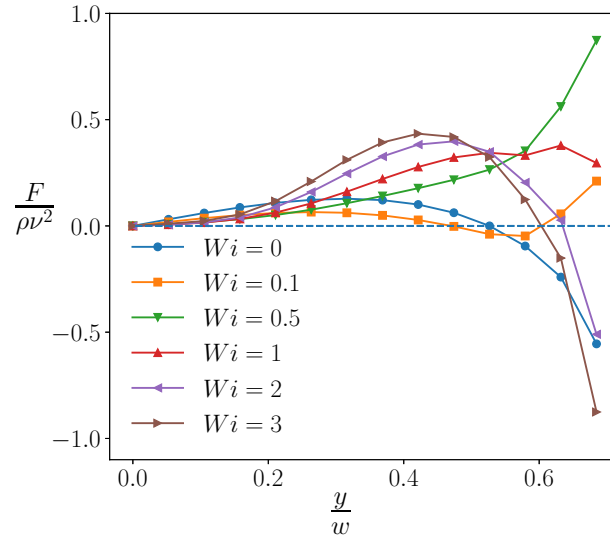


Fig. 5.7. Lateral force profile on the main axis for $Re = 10$

According to Fig. 5.7, the fluid elasticity significantly affects the magnitude of the lateral force such that the force profile near the wall region markedly changes and its direction reverses for high Wi numbers, leading to a stable equilibrium point on the main axes. On the other hand, the slope of the force profile is positive at the center

for the entire range of Weissenberg number explored in this study, implying that the channel center is not a stable position for the particle in this range of parameters. In order to investigate the effect of elasticity on the total lateral force the force-map of inertial and elastic forces are plotted for $Wi = 0.1$ to 3 in Fig. 5.8.

The results show that the inertial force dominates the elastic force. The direction of total force matches that of the inertial force, while the elastic force has a similar profile across the entire channel for various values of Wi number. This behavior indicates that changing the elasticity of the fluid changes the velocity field in the channel. Consequently, the inertial force is affected and the resulting focal pattern alters, while the elastic force itself remains relatively unchanged. In other word, the fluid elasticity affects the particle dynamic indirectly by changing the flow field and not directly by means of elastic force.

5.4.3 Migration in a high inertial regime

With increasing the Reynolds number, the particle dynamics changes significantly from those observed in previous sections. Figure. 5.9(a) shows the force profile for $Re = 30$. The force has a similar trend along the channel main axis for the entire range of Wi number. The force has a positive value near the center and it becomes negative in the near wall region, i.e., the particle is pushed away from the center and the wall, which leads to the existence of an off-center equilibrium point along the main axis. As opposed to previous sections, where the elasticity changes the force profile significantly, the force distribution across the microchannel remains unchanged for the entire range of Wi number studied in this work.

The slope of the force profile at the center and the off-center equilibrium points indicates that the particle is unstable and stable at these points, respectively. According to the force-map shown in Fig. 5.9(b), there is an unstable equilibrium point

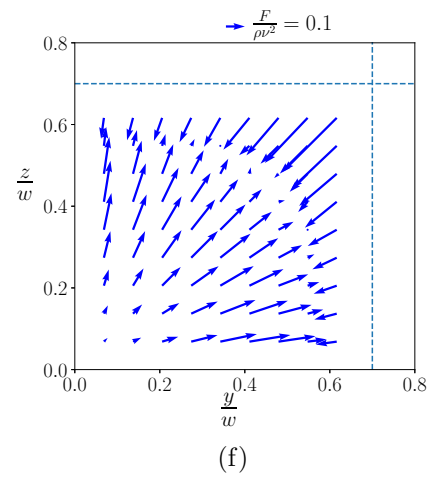
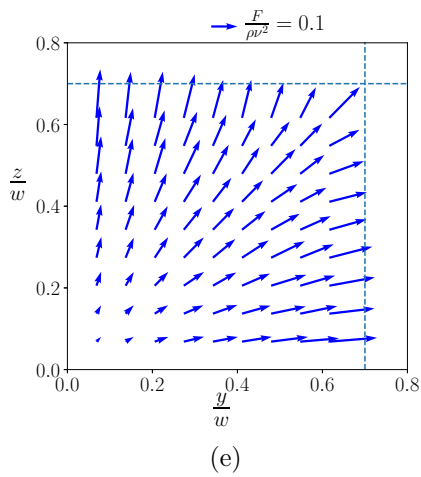
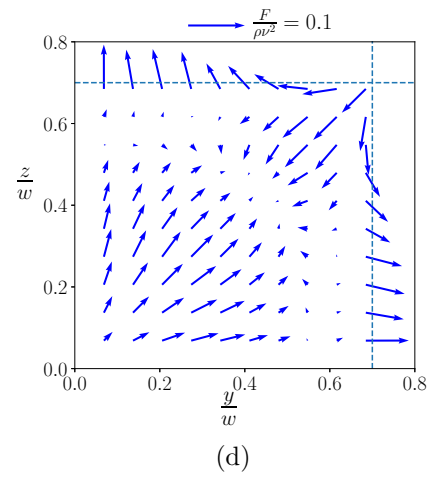
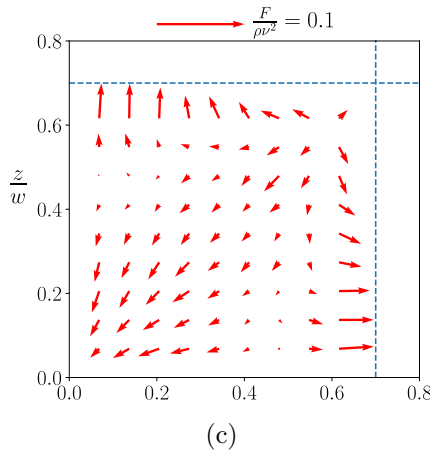
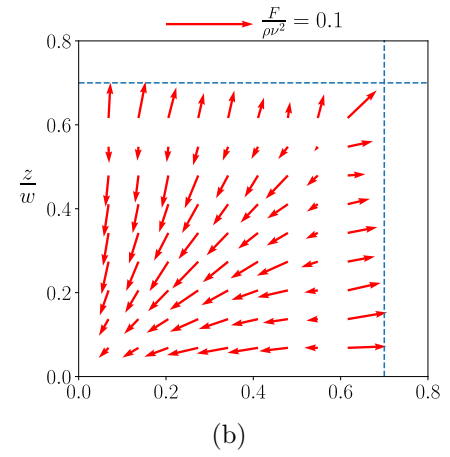
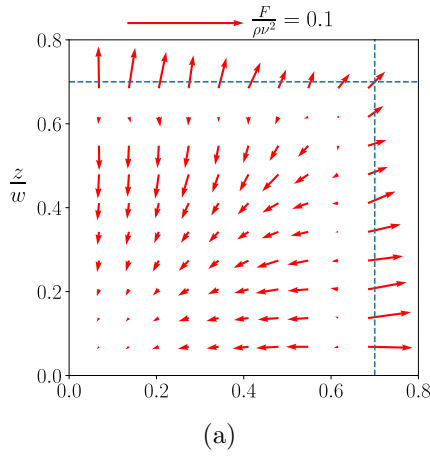


Fig. 5.8. Distribution of elastic force at $Re = 10$ and (a) $Wi = 0.1$ (b) $Wi = 0.5$ (c) $Wi = 3$ and inertial force at (d) $Wi = 0.1$ (e) $Wi = 0.5$ (f) $Wi = 3$

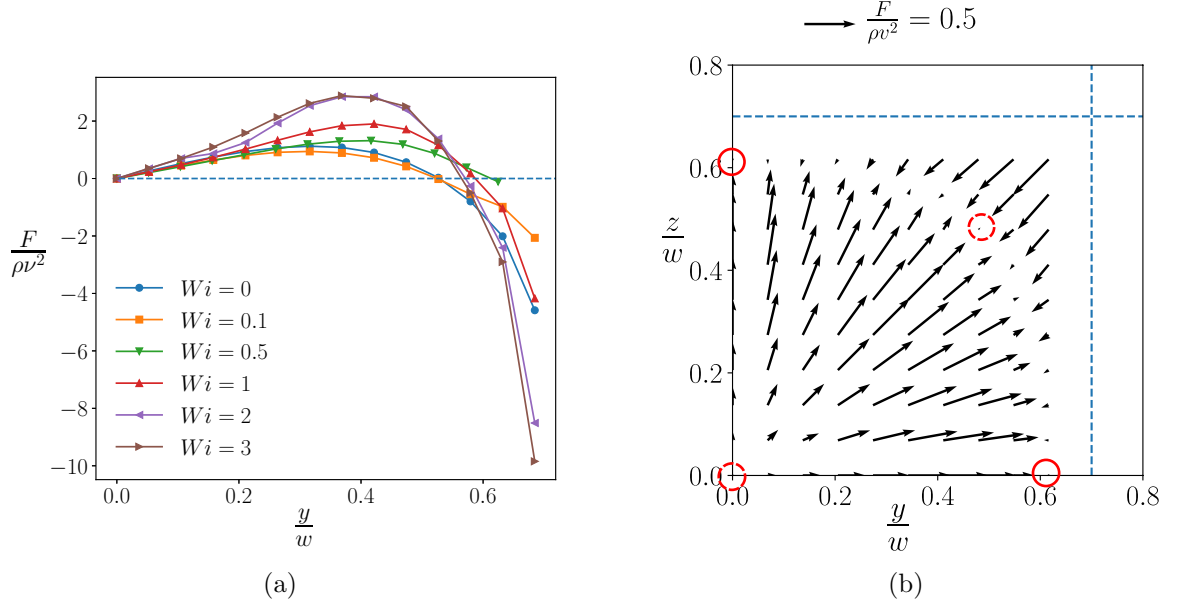


Fig. 5.9. Force profile for (a) $Re = 30$ and (b) the force-map at $Re = 30$ and $Wi = 0.5$.

along the diagonal of the channel at $Re = 30$ and $Wi = 0.5$ that is similar to that of a Newtonian fluid ($Wi = 0$). Hence, the behavior discovered in the numerical and experimental studies by [110] and [58] can be rationalized using our computational results. As shown in Fig. 5.9(a), the force gets stronger along most of the main axis as the Wi number increases (for $Wi > 0.1$). Hence, the particles are pushed away from the center and the wall faster, increasing the transverse migration toward the annulus ring and leading to a smaller critical length of microchannel required for particle focusing. However, this trend is not observed for $Wi = 0.1$ as the force magnitude is smaller than that of a Newtonian fluid.

Figure 5.10 illustrates the distance of the off-center equilibrium points from the channel center and their stability for the entire range of Re and Wi numbers studied in this work along the main axis and the diagonal of the channel.

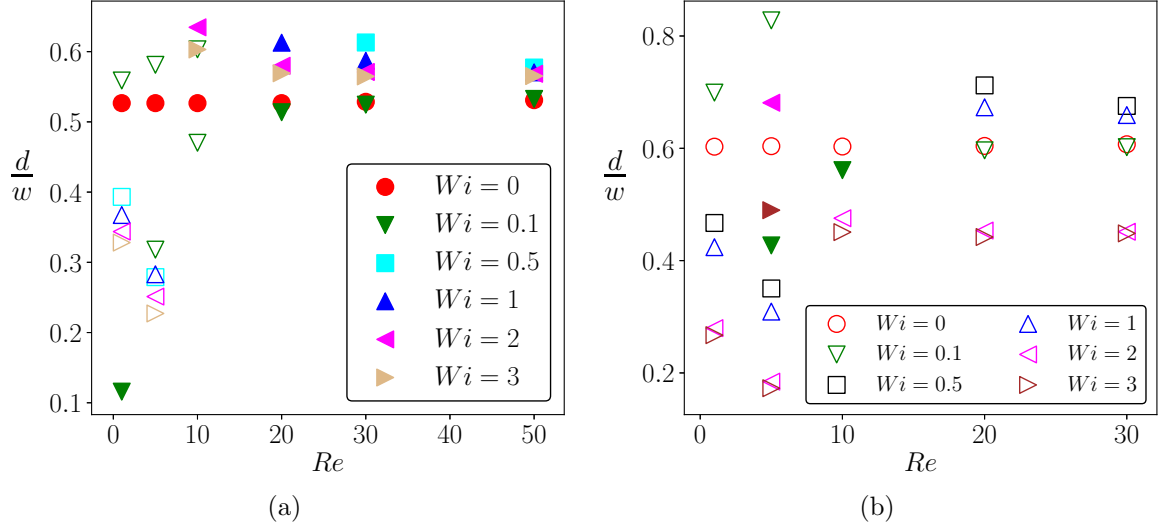


Fig. 5.10. Distance of the off-center equilibrium points from the channel center along (a) the main axis and (b) the diagonal of the channel. Filled symbols indicate stable equilibrium points and open symbols represent unstable equilibrium points.

As shown in Fig. 5.10(a), the equilibrium points for $Wi = 0$ are all stable on the main axis and their location does not change with Re , which is in agreement with previous results found in Li et al. [58]. However, the results show that the equilibrium points for $Wi \neq 0$ are mostly unstable in the low inertial regime ($Re = 1, 5$). The distance of these points are smaller than that of a Newtonian fluid and they approach the channel center with increasing Wi number (for $Wi > 0.5$), indicating reduction of trapping area with increasing the elastic effects. Oppositely, the equilibrium points for $Wi \neq 0$ are all stable on the main axis in the high inertial regime ($Re = 20, 30, 50$). In this range of Re number, the equilibrium points at $Wi = 0.1$ have relatively the same distance from the channel center as that of a Newtonian fluid which is due to the small effect of elasticity compared to inertial effect, while for a higher Wi number this distance is larger than that in a Newtonian fluid. The results also show that the difference between the location of equilibrium points becomes smaller as

the Re number increases. This can be attributed to the dominant effect of the flow inertia compared to the elastic effects. In contrary to the stability of the equilibrium points on the main axis, Fig. 5.10(b) indicates that most of equilibrium points on the diagonal of the channel are unstable. The results show that the equilibrium points approach the channel center with increasing Wi number for low inertial effects, while this behavior changes for larger inertia such that the distance between equilibrium points and channel center initially increases and subsequently the equilibrium point approaches the center with increasing the Wi number.

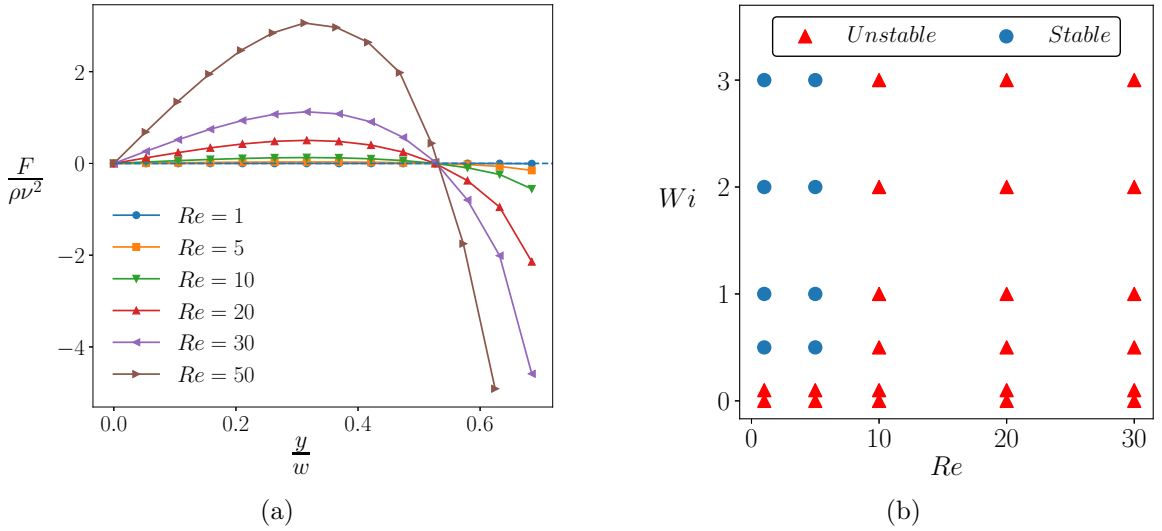


Fig. 5.11. (a) The force profile along the main channel for $Wi = 0$ and (b) the stability of channel centerline equilibrium point for a range of Re and Wi numbers

The location of equilibrium points along the main axis and the diagonal of the channel does not change with the Re number in a Newtonian fluid. In order to explain this phenomenon, the force profile along the channel main axis is plotted for $Wi = 0$ in Fig. 5.11(a). According to this figure, the change in the Re number changes the magnitude of the lateral force acting on the particle. As the inertial effect becomes stronger the lateral force magnitude increases significantly, however, the location at

which the lateral force becomes zero is the same for the entire range of Re number studied in this work. This explains the results reported by [58]. In order to investigate the combined effects of inertia and elasticity on the stability of the channel centerline equilibrium point, the stability phase diagram is illustrated in Fig. 5.11(b). As shown in this figure, the channel center is a stable equilibrium point when the elastic effect dominates the inertial effect, while with increasing the Re number the focal pattern looks similar to that of a Newtonian fluid, where the particle is not expected to travel toward the channel center.

5.5 Summary

In this work, we conduct 3D numerical simulations to find the distribution of lift force acting on the particle in viscoelastic fluids. As a result, we predict the location of equilibrium points and their corresponding stability for a wide range of parameter space which is important for designing microfluidic devices relying on viscoelastic effects. The results for low inertial regime show that the force field acting on the particle changes significantly with increasing the elasticity of the fluid. In the case of a Newtonian fluid the particle is pushed away from the wall and the channel center to reach an annulus ring across the channel. Subsequently, the particle moves toward the equilibrium points on the main axis. Our results show that only off-center equilibrium points along the main axes are stable and other equilibrium points are unstable in a Newtonian fluid. Increasing the elasticity changes the induced force field such that the main axis has no stable equilibrium point and the particle focuses on the corner and off-center points along the diagonal of the channel. Further increase in the Weissenberg number leads to dominance of the elastic force over the inertial lift force, shifting the off-center equilibrium points on the diagonal of the channel toward the channel center.

In the intermediate inertial regime, we also observe various focal patterns by changing the fluid elasticity. In the low Wi number range, the particle focuses at the wall face center and off-center points along the diagonal of the channel. This configuration changes for larger Wi numbers, where the particle is driven radially toward the corner in the entire channel cross-section, leading the corners to be the only basin of attraction in the microchannel. Further increase in the elasticity results in a configuration similar to that of a Newtonian fluid, in which the particle aggregates only at an off-center point on the main axis and equilibrium points on the center and diagonal of the channel are unstable. By splitting the total lift force experienced by the particle into inertial and elastic lift forces we conclude that the elastic effect modifies the velocity field in the microchannel. As a result, the inertial lift force changes accordingly, leading to various particle configurations. However, the direction and the magnitude of the elastic force remain relatively unchanged in the intermediate inertial regime implying that the fluid elasticity affects the particle dynamics indirectly by changing the velocity field. Our results for the high inertial flow indicate that the force profiles are similar for the entire range of Wi number studied in this work. Accordingly the particle configuration is also similar to that of a Newtonian fluid, in which the particles aggregate only at the off-center point along the main axis.

6. CONCLUSION

We investigated the dynamics of deformable cells in a channel flow of Newtonian and polymeric fluids and unravelled the effects of deformability, elasticity, inertia and size on the cell motion. Our results show that the equilibrium position of the cell is on the channel diagonal, in contrary to that of rigid particles, which is in the centre of the channel faces. A constant-viscosity polymeric fluid, modelled using an Oldroyd-B constitutive equation, drives the cells toward the channel centerline, while a shear-thinning polymeric fluid, modelled using a Giesekus constitutive equation, pushes the cells toward the channel wall. We studied a suspension of cells flowing in a microchannel of Newtonian and viscoelastic fluids and investigate the role of cell size, cell volume fraction, inertia, deformability and fluid elasticity on the cell distribution. We show that the use of constant-viscosity viscoelastic fluid pushes the cells toward the channel centerline, which can be used in microfluidic devices used for cell focusing such as cytometers. We also conduct 3D numerical simulations to find the distribution of lift force acting on the particle in viscoelastic fluids that helps us to predict the location of equilibrium points and their corresponding stability for a wide range of inertial and elasticity regimes which is essential for designing microfluidic devices relying on viscoelastic effects.

The experimental studies on microfluidic devices used for separating and focusing of the cells show that cells flowing in a microchannel have various sizes, deformability and shapes. Recent progress in fabrication methods at micro and nano-scale has enabled researchers to develop microfluidic devices with complex geometries. To have better understanding of the performance of these microfluidic devices, the dynamics

of a particle with various geometries (e.g. elongated particles) in a microchannel of complex shapes such as circular, triangular and square channels with round corner filled with Newtonian and non-Newtonian fluids should be studied.

REFERENCES

REFERENCES

- [1] T. Chang, W. Kühtreiber, R. P. Lanza, and W. L. Chick, *Cell encapsulation technology and therapeutics*. Springer Science & Business Media, 2013.
- [2] J. P. Beech, S. H. Holm, K. Adolfsson, and J. O. Tegenfeldt, “Sorting cells by size, shape and deformability,” *Lab on a Chip*, vol. 12, no. 6, pp. 1048–1051, 2012.
- [3] H. Bow, I. V. Pivkin, M. Diez-Silva, S. J. Goldfless, M. Dao, J. C. Niles, S. Suresh, and J. Han, “A microfabricated deformability-based flow cytometer with application to malaria,” *Lab on a Chip*, vol. 11, no. 6, pp. 1065–1073, 2011.
- [4] M. V. Kameneva, Z. J. Wu, A. Uraysh, B. Repko, K. N. Litwak, T. R. Billiar, M. P. Fink, R. L. Simmons, B. P. Griffith, and H. S. Borovetz, “Blood soluble drag-reducing polymers prevent lethality from hemorrhagic shock in acute animal experiments,” *Biorheology*, vol. 41, no. 1, pp. 53–64, 2004.
- [5] H. L. Greene, R. F. Mostardi, and R. F. Nokes, “Effects of drag reducing polymers on initiation of atherosclerosis,” *Polymer Engineering & Science*, vol. 20, no. 7, pp. 499–504, 1980.
- [6] D. Barthes-Biesel, A. Diaz, and E. Dhenin, “Effect of constitutive laws for two-dimensional membranes on flow-induced capsule deformation,” *Journal of Fluid Mechanics*, vol. 460, pp. 211–222, 2002.
- [7] X. Li and K. Sarkar, “Front tracking simulation of deformation and buckling instability of a liquid capsule enclosed by an elastic membrane,” *Journal of Computational Physics*, vol. 227, no. 10, pp. 4998–5018, 2008.
- [8] S. Ramanujan and C. Pozrikidis, “Deformation of liquid capsules enclosed by elastic membranes in simple shear flow: large deformations and the effect of fluid viscosities,” *Journal of Fluid Mechanics*, vol. 361, pp. 117–143, 1998.
- [9] C. D. Eggleton and A. S. Popel, “Large deformation of red blood cell ghosts in a simple shear flow,” *Physics of fluids*, vol. 10, no. 8, pp. 1834–1845, 1998.
- [10] M. Kraus, W. Wintz, U. Seifert, and R. Lipowsky, “Fluid vesicles in shear flow,” *Physical review letters*, vol. 77, no. 17, p. 3685, 1996.
- [11] D. Barthes-Biesel, “Role of interfacial properties on the motion and deformation of capsules in shear flow,” *Physica A: Statistical Mechanics and its Applications*, vol. 172, no. 1-2, pp. 103–124, 1991.
- [12] H. Schmid-Schönbein and R. Wells, “Fluid drop-like transition of erythrocytes under shear,” *Science*, vol. 165, no. 3890, pp. 288–291, 1969.

- [13] D. Barthes-Biesel and J. Rallison, "The time-dependent deformation of a capsule freely suspended in a linear shear flow," *Journal of Fluid Mechanics*, vol. 113, pp. 251–267, 1981.
- [14] D. Barthes-Biesel, "Motion of a spherical microcapsule freely suspended in a linear shear flow," *Journal of Fluid Mechanics*, vol. 100, no. 04, pp. 831–853, 1980.
- [15] X. Li, D. Barthes-Biesel, and A. Helmy, "Large deformations and burst of a capsule freely suspended in an elongational flow," *Journal of fluid mechanics*, vol. 187, pp. 179–196, 1988.
- [16] K. Chang and W. Olbricht, "Experimental studies of the deformation and breakup of a synthetic capsule in steady and unsteady simple shear flow," *Journal of Fluid Mechanics*, vol. 250, pp. 609–633, 1993.
- [17] R. D. Vidic, S. L. Brantley, J. M. Vandenbossche, D. Yoxtheimer, and J. D. Abad, "Impact of shale gas development on regional water quality," *Science*, vol. 340, no. 6134, p. 1235009, 2013.
- [18] M. A. Shannon, P. W. Bohn, M. Elimelech, J. G. Georgiadis, B. J. Marinas, and A. M. Mayes, "Science and technology for water purification in the coming decades," *Nature*, vol. 452, no. 7185, p. 301, 2008.
- [19] J. C. GIDDINGS, K. A. GRAFF, K. D. CALDWELL, and M. N. MYERS, "Field-flow fractionation: Promising approach for the separation and characterization of macromolecules," 1983.
- [20] M. Toner and D. Irimia, "Blood-on-a-chip," *Annu. Rev. Biomed. Eng.*, vol. 7, pp. 77–103, 2005.
- [21] D. R. Gossett, W. M. Weaver, A. J. Mach, S. C. Hur, H. T. K. Tse, W. Lee, H. Amini, and D. Di Carlo, "Label-free cell separation and sorting in microfluidic systems," *Analytical and bioanalytical chemistry*, vol. 397, no. 8, pp. 3249–3267, 2010.
- [22] H. F. Bunn, "Pathogenesis and treatment of sickle cell disease," *New England Journal of Medicine*, vol. 337, no. 11, pp. 762–769, 1997.
- [23] J. Li, Z. Zhang, J. Rosenzweig, Y. Y. Wang, and D. W. Chan, "Proteomics and bioinformatics approaches for identification of serum biomarkers to detect breast cancer," *Clinical chemistry*, vol. 48, no. 8, pp. 1296–1304, 2002.
- [24] J. Villanueva, D. R. Shaffer, J. Philip, C. A. Chaparro, H. Erdjument-Bromage, A. B. Olshen, M. Fleisher, H. Lilja, E. Brogi, J. Boyd *et al.*, "Differential exoprotease activities confer tumor-specific serum peptidome patterns," *The Journal of clinical investigation*, vol. 116, no. 1, pp. 271–284, 2006.
- [25] A. van de Stolpe, K. Pantel, S. Sleijfer, L. W. Terstappen, and J. M. Den Toonder, "Circulating tumor cell isolation and diagnostics: toward routine clinical use," 2011.
- [26] P. Gascoyne, J. Satayavivad, and M. Ruchirawat, "Microfluidic approaches to malaria detection," *Acta tropica*, vol. 89, no. 3, pp. 357–369, 2004.

- [27] K. Krabchi, F. Gros-Louis, J. Yan, M. Bronsard, J. Masse, J.-C. Forest, and R. Drouin, "Quantification of all fetal nucleated cells in maternal blood between the 18th and 22nd weeks of pregnancy using molecular cytogenetic techniques," *Clinical genetics*, vol. 60, no. 2, pp. 145–150, 2001.
- [28] P. Sethu, A. Sin, and M. Toner, "Microfluidic diffusive filter for apheresis (leukapheresis)," *Lab on a Chip*, vol. 6, no. 1, pp. 83–89, 2006.
- [29] A. Karimi, S. Yazdi, and A. Ardekani, "Hydrodynamic mechanisms of cell and particle trapping in microfluidics," *Biomicrofluidics*, vol. 7, no. 2, p. 021501, 2013.
- [30] H. M. Shapiro, *Practical flow cytometry*. John Wiley & Sons, 2005.
- [31] S. Miltenyi, W. Müller, W. Weichel, and A. Radbruch, "High gradient magnetic cell separation with macs," *Cytometry*, vol. 11, no. 2, pp. 231–238, 1990.
- [32] S. Zheng, H. Lin, J.-Q. Liu, M. Balic, R. Datar, R. J. Cote, and Y.-C. Tai, "Membrane microfilter device for selective capture, electrolysis and genomic analysis of human circulating tumor cells," *Journal of chromatography A*, vol. 1162, no. 2, pp. 154–161, 2007.
- [33] J. Takagi, M. Yamada, M. Yasuda, and M. Seki, "Continuous particle separation in a microchannel having asymmetrically arranged multiple branches," *Lab on a Chip*, vol. 5, no. 7, pp. 778–784, 2005.
- [34] M. D. Vahey and J. Voldman, "An equilibrium method for continuous-flow cell sorting using dielectrophoresis," *Analytical chemistry*, vol. 80, no. 9, pp. 3135–3143, 2008.
- [35] G. Segre, "Radial particle displacements in poiseuille flow of suspensions," *Nature*, vol. 189, pp. 209–210, 1961.
- [36] B. Chun and A. Ladd, "Inertial migration of neutrally buoyant particles in a square duct: An investigation of multiple equilibrium positions," *Physics of Fluids*, vol. 18, no. 3, p. 031704, 2006.
- [37] Y. W. Kim and J. Y. Yoo, "The lateral migration of neutrally-buoyant spheres transported through square microchannels," *Journal of Micromechanics and Microengineering*, vol. 18, no. 6, p. 065015, 2008.
- [38] X. Shao, Z. Yu, and B. Sun, "Inertial migration of spherical particles in circular poiseuille flow at moderately high reynolds numbers," *Physics of Fluids*, vol. 20, no. 10, p. 103307, 2008.
- [39] D. Di Carlo, "Inertial microfluidics," *Lab on a Chip*, vol. 9, no. 21, pp. 3038–3046, 2009.
- [40] E. S. Asmolov, "The inertial lift on a spherical particle in a plane poiseuille flow at large channel reynolds number," *Journal of Fluid Mechanics*, vol. 381, pp. 63–87, 1999.
- [41] L. Zeng, S. Balachandar, and P. Fischer, "Wall-induced forces on a rigid sphere at finite reynolds number," *Journal of Fluid Mechanics*, vol. 536, pp. 1–25, 2005.

- [42] R. Cox and H. Brenner, “The lateral migration of solid particles in poiseuille flow: theory,” *Chemical Engineering Science*, vol. 23, no. 2, pp. 147–173, 1968.
- [43] B. Ho and L. Leal, “Inertial migration of rigid spheres in two-dimensional unidirectional flows,” *Journal of fluid mechanics*, vol. 65, no. 2, pp. 365–400, 1974.
- [44] J. A. Schonberg and E. Hinch, “Inertial migration of a sphere in poiseuille flow,” *Journal of Fluid Mechanics*, vol. 203, pp. 517–524, 1989.
- [45] J.-P. Matas, J. F. Morris, and É. Guazzelli, “Inertial migration of rigid spherical particles in poiseuille flow,” *Journal of Fluid Mechanics*, vol. 515, pp. 171–195, 2004.
- [46] A. Karnis, H. Goldsmith, and S. Mason, “The flow of suspensions through tubes: V. inertial effects,” *The Canadian Journal of Chemical Engineering*, vol. 44, no. 4, pp. 181–193, 1966.
- [47] J. Feng, H. H. Hu, and D. D. Joseph, “Direct simulation of initial value problems for the motion of solid bodies in a newtonian fluid part 1. sedimentation,” *Journal of Fluid Mechanics*, vol. 261, pp. 95–134, 1994.
- [48] T.-W. Pan and R. Glowinski, “Direct simulation of the motion of neutrally buoyant balls in a three-dimensional poiseuille flow,” *Comptes Rendus Mécanique*, vol. 333, no. 12, pp. 884–895, 2005.
- [49] B. Yang, J. Wang, D. Joseph, H. H. Hu, T.-W. Pan, and R. Glowinski, “Migration of a sphere in tube flow,” *Journal of Fluid Mechanics*, vol. 540, pp. 109–131, 2005.
- [50] B. Kaoui, G. Ristow, I. Cantat, C. Misbah, and W. Zimmermann, “Lateral migration of a two-dimensional vesicle in unbounded poiseuille flow,” *Physical Review E*, vol. 77, no. 2, p. 021903, 2008.
- [51] A. Kilimnik, W. Mao, and A. Alexeev, “Inertial migration of deformable capsules in channel flow,” *Physics of Fluids*, vol. 23, no. 12, p. 123302, 2011.
- [52] Y.-L. Chen, “Inertia-and deformation-driven migration of a soft particle in confined shear and poiseuille flow,” *RSC Advances*, vol. 4, no. 34, pp. 17 908–17 916, 2014.
- [53] S. C. Hur, N. K. Henderson-MacLennan, E. R. McCabe, and D. Di Carlo, “Deformability-based cell classification and enrichment using inertial microfluidics,” *Lab on a Chip*, vol. 11, no. 5, pp. 912–920, 2011.
- [54] C. Schaaf and H. Stark, “Inertial migration and axial control of deformable capsules,” *Soft Matter*, 2017.
- [55] A. T. Ciftlik, M. Ettori, and M. A. Gijs, “High throughput-per-footprint inertial focusing,” *Small*, vol. 9, no. 16, pp. 2764–2773, 2013.
- [56] D. Di Carlo, J. F. Edd, D. Irimia, R. G. Tompkins, and M. Toner, “Equilibrium separation and filtration of particles using differential inertial focusing,” *Analytical chemistry*, vol. 80, no. 6, pp. 2204–2211, 2008.

- [57] E. J. Lim, T. J. Ober, J. F. Edd, S. P. Desai, D. Neal, K. W. Bong, P. S. Doyle, G. H. McKinley, and M. Toner, “Inertio-elastic focusing of bioparticles in microchannels at high throughput,” *Nature communications*, vol. 5, p. 4120, 2014.
- [58] G. Li, G. H. McKinley, and A. M. Ardekani, “Dynamics of particle migration in channel flow of viscoelastic fluids,” *Journal of Fluid Mechanics*, vol. 785, 2015.
- [59] F. Del Giudice, G. Romeo, G. D’Avino, F. Greco, P. A. Netti, and P. L. Maffettone, “Particle alignment in a viscoelastic liquid flowing in a square-shaped microchannel,” *Lab on a Chip*, vol. 13, no. 21, pp. 4263–4271, 2013.
- [60] F. Del Giudice, G. D’Avino, F. Greco, P. A. Netti, and P. L. Maffettone, “Effect of fluid rheology on particle migration in a square-shaped microchannel,” *Microfluidics and Nanofluidics*, vol. 19, no. 1, pp. 95–104, 2015.
- [61] A. H. Raffee, S. Dabiri, and A. M. Ardekani, “Deformation and buckling of microcapsules in a viscoelastic matrix,” *Physical Review E*, vol. 96, no. 3, p. 032603, 2017.
- [62] J. Charrier, S. Shrivastava, and R. Wu, “Free and constrained inflation of elastic membranes in relation to thermoformingnon-axisymmetric problems,” *The Journal of Strain Analysis for Engineering Design*, vol. 24, no. 2, pp. 55–74, 1989.
- [63] S. Shrivastava and J. Tang, “Large deformation finite element analysis of non-linear viscoelastic membranes with reference to thermoforming,” *The Journal of Strain Analysis for Engineering Design*, vol. 28, no. 1, pp. 31–51, 1993.
- [64] B. P. Leonard, “A stable and accurate convective modelling procedure based on quadratic upstream interpolation,” *Computer methods in applied mechanics and engineering*, vol. 19, no. 1, pp. 59–98, 1979.
- [65] A. J. Chorin, “Numerical solution of the navier-stokes equations,” *Mathematics of computation*, vol. 22, no. 104, pp. 745–762, 1968.
- [66] S. O. Unverdi and G. Tryggvason, “A front-tracking method for viscous, incompressible, multi-fluid flows,” *Journal of computational physics*, vol. 100, no. 1, pp. 25–37, 1992.
- [67] N. Aggarwal and K. Sarkar, “Deformation and breakup of a viscoelastic drop in a newtonian matrix under steady shear,” *Journal of Fluid Mechanics*, vol. 584, pp. 1–21, 2007.
- [68] E. Lac, D. Barthes-Biesel, N. Pelekasis, and J. Tsamopoulos, “Spherical capsules in three-dimensional unbounded stokes flows: effect of the membrane constitutive law and onset of buckling,” *Journal of Fluid Mechanics*, vol. 516, pp. 303–334, 2004.
- [69] S. K. Doddi and P. Bagchi, “Lateral migration of a capsule in a plane poiseuille flow in a channel,” *International Journal of Multiphase Flow*, vol. 34, no. 10, pp. 966–986, 2008.
- [70] K. Yoshimura, J. Usukura, and M. Sokabe, “Gating-associated conformational changes in the mechanosensitive channel mscl,” *Proceedings of the National Academy of Sciences*, vol. 105, no. 10, pp. 4033–4038, 2008.

- [71] A. H. Raffiee, S. Dabiri, and A. M. Ardekani, “Elasto-inertial migration of deformable capsules in a microchannel,” *Biomicrofluidics*, vol. 11, no. 6, p. 064113, 2017.
- [72] R. Skalak, A. Tozeren, R. Zarda, and S. Chien, “Strain energy function of red blood cell membranes,” *Biophysical Journal*, vol. 13, no. 3, pp. 245–264, 1973.
- [73] T. Krüger, B. Kaoui, and J. Harting, “Interplay of inertia and deformability on rheological properties of a suspension of capsules,” *Journal of Fluid Mechanics*, vol. 751, pp. 725–745, 2014.
- [74] H. Giesekus, “A simple constitutive equation for polymer fluids based on the concept of deformation-dependent tensorial mobility,” *Journal of Non-Newtonian Fluid Mechanics*, vol. 11, no. 1-2, pp. 69–109, 1982.
- [75] G. Schleiniger and R. Weinacht, “A remark on the giesekus viscoelastic fluid,” *Journal of Rheology*, vol. 35, no. 6, pp. 1157–1170, 1991.
- [76] D. Di Carlo, J. F. Edd, K. J. Humphry, H. A. Stone, and M. Toner, “Particle segregation and dynamics in confined flows,” *Physical review letters*, vol. 102, no. 9, p. 094503, 2009.
- [77] B. Ho and L. Leal, “Migration of rigid spheres in a two-dimensional unidirectional shear flow of a second-order fluid,” *Journal of Fluid Mechanics*, vol. 76, no. 4, pp. 783–799, 1976.
- [78] G. D’Avino, G. Romeo, M. M. Villone, F. Greco, P. A. Netti, and P. L. Maffettone, “Single line particle focusing induced by viscoelasticity of the suspending liquid: theory, experiments and simulations to design a micropipe flow-focuser,” *Lab on a Chip*, vol. 12, no. 9, pp. 1638–1645, 2012.
- [79] A. Leshansky, A. Bransky, N. Korin, and U. Dinnar, “Tunable nonlinear viscoelastic focusing in a microfluidic device,” *Physical review letters*, vol. 98, no. 23, p. 234501, 2007.
- [80] R. B. Bird, R. C. Armstrong, and O. Hassager, “Dynamics of polymeric liquids. vol. 1: Fluid mechanics,” 1987.
- [81] S. Yang, J. Y. Kim, S. J. Lee, S. S. Lee, and J. M. Kim, “Sheathless elasto-inertial particle focusing and continuous separation in a straight rectangular microchannel,” *Lab on a Chip*, vol. 11, no. 2, pp. 266–273, 2011.
- [82] K. Kang, S. S. Lee, K. Hyun, S. J. Lee, and J. M. Kim, “Dna-based highly tunable particle focuser,” *Nature communications*, vol. 4, p. 2567, 2013.
- [83] C. Prohm and H. Stark, “Feedback control of inertial microfluidics using axial control forces,” *Lab on a Chip*, vol. 14, no. 12, pp. 2115–2123, 2014.
- [84] J. Happel and H. Brenner, *Low Reynolds number hydrodynamics: with special applications to particulate media*. Springer Science & Business Media, 2012, vol. 1.
- [85] R. P. Chhabra, *Bubbles, drops, and particles in non-Newtonian fluids*. CRC press, 2006.

- [86] D. Di Carlo, D. Irimia, R. G. Tompkins, and M. Toner, "Continuous inertial focusing, ordering, and separation of particles in microchannels," *Proceedings of the National Academy of Sciences*, vol. 104, no. 48, pp. 18 892–18 897, 2007.
- [87] A. H. Raffee, S. Dabiri, and A. M. Ardekani, "Suspension of deformable particles in newtonian and viscoelastic fluids in a microchannel," *Microfluidics and Nanofluidics*, vol. 23, no. 2, p. 22, 2019.
- [88] A. S. Popel and P. C. Johnson, "Microcirculation and hemorrheology," *Annu. Rev. Fluid Mech.*, vol. 37, pp. 43–69, 2005.
- [89] C. Pozrikidis, *Modeling and simulation of capsules and biological cells*. CRC Press, 2003.
- [90] P. Paiè, F. Bragheri, D. Di Carlo, and R. Osellame, "Particle focusing by 3d inertial microfluidics," *Microsystems & Nanoengineering*, vol. 3, p. 17027, 2017.
- [91] T. D. Chung and H. C. Kim, "Recent advances in miniaturized microfluidic flow cytometry for clinical use," *Electrophoresis*, vol. 28, no. 24, pp. 4511–4520, 2007.
- [92] J. Godin, C.-H. Chen, S. H. Cho, W. Qiao, F. Tsai, and Y.-H. Lo, "Microfluidics and photonics for bio-system-on-a-chip: A review of advancements in technology towards a microfluidic flow cytometry chip," *Journal of biophotonics*, vol. 1, no. 5, pp. 355–376, 2008.
- [93] R. Pethig, "Dielectrophoresis: Status of the theory, technology, and applications," *Biomicrofluidics*, vol. 4, no. 2, p. 022811, 2010.
- [94] N. Pamme, "Magnetism and microfluidics," *Lab on a Chip*, vol. 6, no. 1, pp. 24–38, 2006.
- [95] J. Friend and L. Y. Yeo, "Microscale acoustofluidics: Microfluidics driven via acoustics and ultrasonics," *Reviews of Modern Physics*, vol. 83, no. 2, p. 647, 2011.
- [96] N. Sundararajan, M. S. Pio, L. P. Lee, and A. A. Berlin, "Three-dimensional hydrodynamic focusing in polydimethylsiloxane (pdms) microchannels," *Journal of Microelectromechanical systems*, vol. 13, no. 4, pp. 559–567, 2004.
- [97] C. Lancaster, M. Kokoris, M. Nabavi, J. Clemmens, P. Maloney, J. Capadanno, J. Gerdes, and C. Battrell, "Rare cancer cell analyzer for whole blood applications: Microcytometer cell counting and sorting subcircuits," *Methods*, vol. 37, no. 1, pp. 120–127, 2005.
- [98] P. B. Howell Jr, J. P. Golden, L. R. Hilliard, J. S. Erickson, D. R. Mott, and F. S. Ligler, "Two simple and rugged designs for creating microfluidic sheath flow," *Lab on a Chip*, vol. 8, no. 7, pp. 1097–1103, 2008.
- [99] F. Del Giudice, S. Sathish, G. D'Avino, and A. Q. Shen, "from the edge to the center: viscoelastic migration of particles and cells in a strongly shear-thinning liquid flowing in a microchannel," *Analytical chemistry*, 2017.
- [100] Y.-S. Choi, K.-W. Seo, and S.-J. Lee, "Lateral and cross-lateral focusing of spherical particles in a square microchannel," *Lab on a Chip*, vol. 11, no. 3, pp. 460–465, 2011.

- [101] S. C. Hur, H. T. K. Tse, and D. Di Carlo, "Sheathless inertial cell ordering for extreme throughput flow cytometry," *Lab on a Chip*, vol. 10, no. 3, pp. 274–280, 2010.
- [102] A. Kunze, J. Che, A. Karimi, and D. Di Carlo, "Research highlights: cell separation at the bench and beyond," *Lab on a Chip*, vol. 15, no. 3, pp. 605–609, 2015.
- [103] D. J. Lee, H. Brenner, J. R. Youn, and Y. S. Song, "Multiplex particle focusing via hydrodynamic force in viscoelastic fluids," *Scientific reports*, vol. 3, 2013.
- [104] X. Lu, C. Liu, G. Hu, and X. Xuan, "Particle manipulations in non-newtonian microfluidics: A review," *Journal of Colloid and Interface Science*, 2017.
- [105] G. D'Avino, F. Greco, and P. L. Maffettone, "Particle migration due to viscoelasticity of the suspending liquid and its relevance in microfluidic devices," *Annual Review of Fluid Mechanics*, vol. 49, pp. 341–360, 2017.
- [106] M. A. Faridi, H. Ramachandraiah, I. Banerjee, S. Ardabili, S. Zelenin, and A. Russom, "Elasto-inertial microfluidics for bacteria separation from whole blood for sepsis diagnostics," *Journal of nanobiotechnology*, vol. 15, no. 1, p. 3, 2017.
- [107] M. Villone, G. D'Avino, M. Hulsen, F. Greco, and P. Maffettone, "Particle motion in square channel flow of a viscoelastic liquid: Migration vs. secondary flows," *Journal of Non-Newtonian Fluid Mechanics*, vol. 195, pp. 1–8, 2013.
- [108] J. Nam, J. K. S. Tan, B. L. Khoo, B. Namgung, H. L. Leo, C. T. Lim, and S. Kim, "Hybrid capillary-inserted microfluidic device for sheathless particle focusing and separation in viscoelastic flow," *Biomicrofluidics*, vol. 9, no. 6, p. 064117, 2015.
- [109] C. Liu, C. Xue, X. Chen, L. Shan, Y. Tian, and G. Hu, "Size-based separation of particles and cells utilizing viscoelastic effects in straight microchannels," *Analytical chemistry*, vol. 87, no. 12, pp. 6041–6048, 2015.
- [110] K. W. Seo, Y. J. Kang, and S. J. Lee, "Lateral migration and focusing of microspheres in a microchannel flow of viscoelastic fluids," *Physics of Fluids*, vol. 26, no. 6, p. 063301, 2014.
- [111] G. Romeo, G. D'Avino, F. Greco, P. A. Netti, and P. L. Maffettone, "Viscoelastic flow-focusing in microchannels: scaling properties of the particle radial distributions," *Lab on a Chip*, vol. 13, no. 14, pp. 2802–2807, 2013.
- [112] P. Pranay, R. G. Henríquez-Rivera, and M. D. Graham, "Depletion layer formation in suspensions of elastic capsules in newtonian and viscoelastic fluids," *Physics of Fluids*, vol. 24, no. 6, p. 061902, 2012.
- [113] H. Zhao, E. S. Shaqfeh, and V. Narsimhan, "Shear-induced particle migration and margination in a cellular suspension," *Physics of Fluids (1994-present)*, vol. 24, no. 1, p. 011902, 2012.
- [114] D. A. Fedosov, B. Caswell, A. S. Popel, and G. E. Karniadakis, "Blood flow and cell-free layer in microvessels," *Microcirculation*, vol. 17, no. 8, pp. 615–628, 2010.

- [115] X. Li and C. Pozrikidis, "Wall-bounded shear flow and channel flow of suspensions of liquid drops," *International journal of multiphase flow*, vol. 26, no. 8, pp. 1247–1279, 2000.
- [116] S. K. Doddi and P. Bagchi, "Three-dimensional computational modeling of multiple deformable cells flowing in microvessels," *Physical Review E*, vol. 79, no. 4, p. 046318, 2009.
- [117] A. H. Raffiee, A. M. Ardekani, and S. Dabiri, "Numerical investigation of elasto-inertial particle focusing patterns in viscoelastic microfluidic devices," *Journal of Non-Newtonian Fluid Mechanics*, vol. 272, p. 104166, 2019.
- [118] J. Khalesi and N. Sarunac, "Numerical analysis of flow and conjugate heat transfer for supercritical co₂ and liquid sodium in square microchannels," *International Journal of Heat and Mass Transfer*, vol. 132, pp. 1187–1199, 2019.
- [119] C. Yamashita, M. M. S. Chung, C. dos Santos, C. R. M. Mayer, I. C. F. Moraes, and I. G. Branco, "Microencapsulation of an anthocyanin-rich blackberry (*rubus* spp.) by-product extract by freeze-drying," *LWT*, vol. 84, pp. 256–262, 2017.
- [120] B. Castro, M. S. de Medeiros, B. Sadri, and R. V. Martinez, "Portable and power-free serodiagnosis of chagas disease using magnetic levitating microbeads," *Analyst*, vol. 143, no. 18, pp. 4379–4386, 2018.
- [121] H. M. Sadeghi, B. Sadri, M. A. Kazemi, and M. Jafari, "Coalescence of charged droplets in outer fluids," *Journal of Colloid and Interface Science*, vol. 532, pp. 363–374, 2018.
- [122] S. Choi, S. Song, C. Choi, and J.-K. Park, "Microfluidic self-sorting of mammalian cells to achieve cell cycle synchrony by hydrophoresis," *Analytical Chemistry*, vol. 81, no. 5, pp. 1964–1968, 2009.
- [123] P. Hafezisefat, M. N. Esfahany, and M. Jafari, "An experimental and numerical study of heat transfer in jacketed vessels by sio₂ nanofluid," *Heat and Mass Transfer*, vol. 53, no. 7, pp. 2395–2405, 2017.
- [124] J. El-Ali, P. K. Sorger, and K. F. Jensen, "Cells on chips," *Nature*, vol. 442, no. 7101, p. 403, 2006.
- [125] H. Park, A. H. Raffiee, S. W. John, A. M. Ardekani, and H. Lee, "Towards smart self-clearing glaucoma drainage device," *Microsystems & Nanoengineering*, vol. 4, no. 1, p. 35, 2018.
- [126] Z. Almansoori, B. Khorshidi, B. Sadri, and M. Sadrzadeh, "Parametric study on the stabilization of metal oxide nanoparticles in organic solvents: A case study with indium tin oxide (ito) and heptane," *Ultrasonics Sonochemistry*, vol. 40, pp. 1003–1013, 2018.
- [127] B. Sadri, D. Pernitsky, and M. Sadrzadeh, "Aggregation and deposition of colloidal particles: Effect of surface properties of collector beads," *Colloids and Surfaces A: Physicochemical and Engineering Aspects*, vol. 530, pp. 46–52, 2017.
- [128] K. Ishii and H. Hashimoto, "Lateral migration of a spherical particle in flows in a circular tube," *Journal of the Physical Society of Japan*, vol. 48, no. 6, pp. 2144–2155, 1980.

- [129] Z. Isiksacan, M. T. Guler, A. Kalantarifard, M. Asghari, and C. Elbuken, “Lab-on-a-chip platforms for disease detection and diagnosis,” *Biosensors and Nanotechnology: Applications in Health Care Diagnostics*, pp. 155–181, 2018.
- [130] Z. Isiksacan, M. Asghari, and C. Elbuken, “A microfluidic erythrocyte sedimentation rate analyzer using rouleaux formation kinetics,” *Microfluidics and Nanofluidics*, vol. 21, no. 3, p. 44, 2017.
- [131] A. Karnis and S. Mason, “Particle motions in sheared suspensions. xix. viscoelastic media,” *Transactions of the Society of Rheology*, vol. 10, no. 2, pp. 571–592, 1966.
- [132] F. Gauthier, H. Goldsmith, and S. Mason, “Particle motions in non-newtonian media. ii. poiseuille flow,” *Transactions of the Society of Rheology*, vol. 15, no. 2, pp. 297–330, 1971.
- [133] P.-H. Chan and L. Leal, “A note on the motion of a spherical particle in a general quadratic flow of a second-order fluid,” *Journal of Fluid Mechanics*, vol. 82, no. 3, pp. 549–559, 1977.
- [134] P. Brunn, “The motion of rigid particles in viscoelastic fluids,” *Journal of non-Newtonian fluid mechanics*, vol. 7, no. 4, pp. 271–288, 1980.
- [135] L. Leal, “Particle motions in a viscous fluid,” *Annual Review of Fluid Mechanics*, vol. 12, no. 1, pp. 435–476, 1980.
- [136] L. Zeng, F. Najjar, S. Balachandar, and P. Fischer, “Forces on a finite-sized particle located close to a wall in a linear shear flow,” *Physics of Fluids*, vol. 21, no. 3, p. 033302, 2009.
- [137] M. Trofa, M. Voccianti, G. D’Avino, M. A. Hulsen, F. Greco, and P. L. Maffettone, “Numerical simulations of the competition between the effects of inertia and viscoelasticity on particle migration in poiseuille flow,” *Computers & Fluids*, vol. 107, pp. 214–223, 2015.
- [138] C. Liu, C. Xue, J. Sun, and G. Hu, “A generalized formula for inertial lift on a sphere in microchannels,” *Lab on a Chip*, vol. 16, no. 5, pp. 884–892, 2016.
- [139] P. Huang, J. Feng, H. H. Hu, and D. D. Joseph, “Direct simulation of the motion of solid particles in couette and poiseuille flows of viscoelastic fluids,” *Journal of Fluid Mechanics*, vol. 343, pp. 73–94, 1997.
- [140] P. Wang, Z. Yu, and J. Lin, “Numerical simulations of particle migration in rectangular channel flow of giesekus viscoelastic fluids,” *Journal of Non-Newtonian Fluid Mechanics*, vol. 262, pp. 142–148, 2018.
- [141] A. Saadat, C. J. Guido, G. Iaccarino, and E. S. Shaqfeh, “Immersed-finite-element method for deformable particle suspensions in viscous and viscoelastic media,” *Physical Review E*, vol. 98, no. 6, p. 063316, 2018.
- [142] A. M. Ardekani, S. Dabiri, and R. H. Rangel, “Collision of multi-particle and general shape objects in a viscous fluid,” *Journal of Computational Physics*, vol. 227, no. 24, pp. 10 094–10 107, 2008.

- [143] C. Liu, G. Hu, X. Jiang, and J. Sun, “Inertial focusing of spherical particles in rectangular microchannels over a wide range of reynolds numbers,” *Lab on a Chip*, vol. 15, no. 4, pp. 1168–1177, 2015.
- [144] D. R. Gossett, H. T. K. Tse, J. S. Dudani, K. Goda, T. A. Woods, S. W. Graves, and D. Di Carlo, “Inertial manipulation and transfer of microparticles across laminar fluid streams,” *Small*, vol. 8, no. 17, pp. 2757–2764, 2012.

VITA

VITA

Education

PhD in Mechanical Engineering, **Purdue University** , 2015-2019

M.Sc in Mechanical Engineering, **Sharif University of Technology** , 2011-2013

B.Sc in Mechanical Engineering, **Sharif University of Technology** , 2007-2011

Publication

A.H. Raffee, A.M. Ardekani, S. Dabiri, Numerical investigation of elasto-inertial particle focusing patterns in viscoelastic microfluidic devices, *Journal of Non-Newtonian Fluid Mechanics*, 272, 104166.

A.H. Raffee, S. Dabiri, A.M. Ardekani, Suspension of deformable particles in Newtonian and viscoelastic fluids in a microchannel, *Microfluidics Nanofluidics*, 2019.

H. Park, **A.H. Raffee**, S.W.M. John, A.M. Ardekani, H. Lee, Towards Smart Self-Clearing Glaucoma Drainage Device, *Microsystems Nanoengineering*, 2018.

A.H. Raffee, S. Dabiri, A.M. Ardekani, Elasto-inertial migration of deformable capsules in a microchannel, *Biomicrofluidics*, 2017.

A.H. Raffee, S. Dabiri, A.M. Ardekani, Deformation and buckling of microcapsules in a viscoelastic fluid, *Physical Review E*, 2017.

A.H. Raffee, S. Dabiri, A.M. Ardekani, Deformation and buckling of microcapsules in a viscoelastic matrix, *Midwestern Universities Fluid Mechanics Retreat*, 2017.

A.H. Raffee, S. Dabiri, A.M. Ardekani, Modeling malaria infected cells in microcirculation, *APS meeting* 2016.